

CONFIDENTIAL

Designing an Adaptive Head and Neck Immobilization Device

For use in Proton Therapy

A.M. Brouwer

Master of Science Thesis

proBEAM

CONFIDENTIAL

Designing an Adaptive Head and Neck Immobilization Device

For use in Proton Therapy

MASTER OF SCIENCE THESIS

For the degree of Master of Science in Systems and Control, and
Mechanical Engineering at Delft University of Technology

A.M. Brouwer

September 27, 2018

Faculty of Mechanical, Maritime and Materials Engineering (3mE) · Delft University of
Technology

Cover image courtesy of Varian Medical Systems, Inc. All rights reserved.

Copyright © Delft Center for Systems and Control, and the Department of Precision and
Microsystems Engineering
All rights reserved.

DELFT UNIVERSITY OF TECHNOLOGY
DEPARTMENTS OF
DELFT CENTER FOR SYSTEMS AND CONTROL, AND THE DEPARTMENT OF
PRECISION AND MICROSYSTEMS ENGINEERING

The undersigned hereby certify that they have read and recommend to the Faculty of
Mechanical, Maritime and Materials Engineering (3mE) for acceptance a thesis
entitled

DESIGNING AN ADAPTIVE HEAD AND NECK IMMOBILIZATION DEVICE

by

A.M. BROUWER

in partial fulfillment of the requirements for the degree of
MASTER OF SCIENCE IN SYSTEMS AND CONTROL, AND MECHANICAL
ENGINEERING

Dated: September 27, 2018

Supervisor(s):

prof.dr.ir. M. Verhaegen

ir. J.W. Spronck

Reader(s):

prof.dr.ir. J.L. Herder

dr. E. Steur

Summary

Introduction

Radiotherapy is the treatment of cancer and other diseases with ionizing radiation. An increasingly popular form of radiotherapy is proton therapy. It uses a beam of protons instead of high energy photons to deliver the radiation dose. Due to physical properties of protons (most notably the Bragg peak), the dose can be delivered more precisely to the target volume. The result is a lower integral dose and less healthy tissue damage. This makes proton therapy suitable for the treatment of tumors close to critical organs such as in the head and neck. To minimize alignment errors the head and neck are immobilized during treatment. A commonly used immobilization device for the head and neck is the thermoplastic mask.

The problem with current immobilization methods is that they are unable to correct a misalignment of the head relative to the body. Especially nodding motions lead to large local alignment errors. The thermoplastic mask is also rather uncomfortable. The objective of this study is therefore to design an immobilization device that automatically aligns and immobilizes the head and neck with respect to the body. It must be transparent to the proton beam, compatible with CT and MRI machines, comfortable to use and able to adapt to the patient.

Methods

An adaptive immobilization must perform several functions. Several options for each function are listed in a morphological chart. A concept is generated by selecting a combination of these options. The chosen concept is an open helmet-like shell around the patients head in which eight actuators are placed. Six of these are placed to the sides of the head and two to the back. The side actuators are placed in opposing pairs since they can only push against the head and not pull.

Each actuator module consists of a spherical rubber membrane that is inflated by a precisely controlled pneumatic piston. The pressure in the membrane and the position of the piston are continuously measured. The immobilization device itself is compatible with CT and MRI imaging devices. However, because the source part contains metals, it must be moved away from sensitive imaging equipment thus away from the immobilization device. It is therefore connected to the membrane by a long flexible tube.

The head and neck are modeled as a kinematic chain with five degrees of freedom (DOFs). The parameters of this anatomical model are based on a male (height: 1.74m). A static equilibrium of the internal and external forces is found with a minimization of the total potential energy.

The alignment error is calculated by a 3D-2D registration of two orthogonal X-ray projections with the planning-CT (pCT). A controller uses this alignment error to actuate both the six DOF treatment couch and the five DOF actuators inside the immobilization device. The model of the system is linearized and the control input to the actuators is found by a convex optimization of this linearized model. The solution is optimal for the linearized problem. The clamping force of the actuators is also estimated and is kept constant by the controller.

Results

The minimum actuator stiffness depends on the moments that are subconsciously generated by the neck. It is designed to keep the rotational error below 0.3° and the translational error below 0.6 mm. The back actuators need to be approximately twice as stiff as the side actuators. The membrane model was verified by measurements on a compression tester.

For a simple setup with two regions-of-interest (ROIs) (body, skull) a 3D alignment error below 1.5° for rotations, and 1.4 mm for translations was reached with 95 % certainty. This was after only a single correction by the controller.

For more complex cases (body, C5, C2, skull) three corrections were needed to reduce the error to within 1.4° and 1.3 mm, respectively. For a system with a larger initial body displacement ($\sigma_{\text{rot}} = 2^\circ$ and $\sigma_{\text{tr}} = 5$ mm in all major directions) the errors after three corrections were within 2.2° and 1.4 mm, respectively. The large rotational error is due to the misalignment of vertebra C5 which was added to the model using an alternate method. In comparison, current immobilization methods offer a 3D alignment error of 1.9° for rotations and 3.3 mm for translations.

The correction of the clamping force negatively impacts the rotational error in anterior-posterior (AP) direction (nodding motion), where the root mean square (RMS) error has increased from 0.34° to 0.74° .

Conclusion

The designed immobilization device outperforms current alternative methods. In particular, it is better than the thermoplastic mask with a treatment couch correction. After a single correction the alignment errors are similar to or lower than those of existing methods.

The device boasts an open design that is comfortable for the patient. It is also suitable for use in CT and MRI machines because it contains no metals and is made of a thin shell with low density gradients. The minimum stiffness of the actuators is sufficient to withstand intrafraction motion (motion during the treatment). Usage of a closed-volume pneumatic system for the actuators offers the ability to detect sudden motions and to estimate and correct the clamping force on the head and neck.

A parameter estimation of the anatomical model is deemed unnecessary due to the inherent robustness of the controller. Using this device the setup time will decrease resulting in an increased throughput of patients of up to 15 %.

Future Research

A few things should still be researched before clinical trials. Most importantly the error due to the force correction must be resolved. It must also be investigated whether the body can be assumed to be fixed to the treatment couch. Similarly, the mandible and hyoid bone must be investigated for intrafraction motion. If necessary, they also must be fixed.

Contents

| | |
|--|-------------|
| Acknowledgments | xvii |
| 1 Introduction | 1 |
| 2 Proton Therapy: Background | 3 |
| 2-1 Tumor: Clinical Target Volume | 3 |
| 2-2 Protons vs. Photons | 3 |
| 2-3 Treatment Process | 5 |
| 2-4 Current Immobilization Methods | 6 |
| 2-4-1 Immobilization of the Head and Neck | 7 |
| 2-4-2 Localization of the CTV | 8 |
| 2-4-3 Correction Methods | 9 |
| 2-5 Alignment Errors: Cause and Effect | 10 |
| 3 Objective and Requirements | 13 |
| 3-1 Problems of Current Immobilization Methods | 13 |
| 3-2 Objective | 14 |
| 3-3 Design Requirements | 15 |
| 3-3-1 Error Requirements | 15 |
| 3-3-2 Setup Requirements | 16 |
| 3-3-3 Control Requirements | 16 |
| 4 Design of the Immobilization Device | 19 |
| 4-1 Body Fixation | 19 |
| 4-2 Concept Generation and Selection | 19 |
| 4-3 Attenuation of the Proton Beam | 21 |
| 4-4 Design of the Air Channel | 22 |

| | | |
|----------|--|-----------|
| 5 | Membrane Actuators | 23 |
| 5-1 | Actuator Type | 23 |
| 5-2 | Actuator Placement and Actuation Axis | 24 |
| 5-3 | Actuator Module: Closed Pneumatic System | 28 |
| 5-4 | Design Requirements | 28 |
| 5-4-1 | Working Range | 28 |
| 5-4-2 | Minimum Stiffness | 29 |
| 5-4-3 | Dimensional Parameters | 30 |
| 5-4-4 | Patient Comfort and Safety | 31 |
| 5-5 | Membrane Models | 31 |
| 5-5-1 | General Framework | 32 |
| 5-5-2 | Geometrical Model: Approximation | 33 |
| 5-5-3 | Physical Model: Constitutive Equations | 33 |
| 5-5-4 | Limit-Point Instability | 35 |
| 5-5-5 | Temperature Sensitivity | 36 |
| 5-6 | Parameter Optimization | 37 |
| 5-7 | Simulation and Verification | 39 |
| 5-7-1 | Free vs. Constrained Inflation | 39 |
| 5-7-2 | Measurement Setup and Model Verification | 40 |
| 5-7-3 | Minimum Stiffness Verification | 42 |
| 5-7-4 | Distance Estimation of the Contact Surface | 44 |
| 6 | Anatomical Model | 45 |
| 6-1 | Anatomy of the Head and Neck | 45 |
| 6-1-1 | Dominant Range of Motion | 45 |
| 6-1-2 | Neck Stiffness | 45 |
| 6-2 | Kinematics | 49 |
| 6-2-1 | Forward Kinematics | 49 |
| 6-2-2 | Inverse Kinematics | 52 |
| 6-3 | Static Equilibrium: Minimum Total Potential Energy Principle | 53 |
| 6-3-1 | Prismatic and Revolute Joints | 54 |
| 6-3-2 | Membrane Actuators: Nonlinear Springs | 55 |
| 6-3-3 | Gravitational Force | 56 |
| 7 | Controller Design and Performance Evaluation | 57 |
| 7-1 | Overview | 57 |
| 7-2 | Discrete State Space Model | 58 |
| 7-2-1 | Linearization | 59 |
| 7-2-2 | Observability | 59 |
| 7-2-3 | Controllability | 61 |
| 7-3 | Intrafraction Controller | 62 |
| 7-3-1 | Unconstrained Controller | 63 |

| | | |
|----------|--|------------|
| 7-3-2 | Constrained Controller: Force Correction | 64 |
| 7-3-3 | Nonlinear Observer: an Extended Kalman Filter | 66 |
| 7-4 | Model Personalization: Parameter Estimation | 67 |
| 7-5 | Simulation and Verification | 67 |
| 7-5-1 | Simulation Procedure | 67 |
| 7-5-2 | Alignment Performance | 70 |
| 7-5-3 | Fixation Performance | 73 |
| 7-5-4 | Parameter Estimation Results | 75 |
| 7-5-5 | Verification with a Clamped Cantilever Beam | 75 |
| 8 | Conclusion | 77 |
| 9 | Future Research | 79 |
| A | Medical Terminology | 81 |
| A-1 | Directional Terms | 81 |
| A-2 | Relevant Head and Neck Anatomy | 82 |
| B | Errors and Uncertainties | 83 |
| B-1 | Calculation of the Alignment Errors | 83 |
| B-2 | Rigid Body Errors | 83 |
| B-3 | 3D Errors: Chi Distribution | 84 |
| C | Screw Theory | 85 |
| C-1 | Twists | 85 |
| C-2 | Wrenches | 85 |
| D | Concept Generation | 87 |
| D-1 | Morphological Chart | 87 |
| D-1-1 | Concept 1: Stereoscopic X-ray, Pneumatic Actuation | 89 |
| D-1-2 | Concept 2: Surface Scanning, Electric Actuation | 89 |
| D-1-3 | Concept 3: IR-Tracking, Electric Actuation | 90 |
| D-2 | Concept Selection | 91 |
| E | Geometric Membrane Model: Stiffness Mechanisms | 93 |
| F | Extended Kalman Filter: Algorithm | 97 |
| | Bibliography | 99 |
| | List of Acronyms | 107 |

List of Figures

| | | |
|-----|--|----|
| 2-1 | A typical treatment room. Inside the gantry are shown: the treatment couch (blue), the proton beam nozzle (orange) and two orthogonal X-ray imaging detectors (yellow). Sometimes an optional CT device is placed in the same room for faster and more precise imaging. From [3]. | 4 |
| 2-2 | The dose distribution of protons compared to photons. The Bragg peak is where the protons start decelerating rapidly which is why all the energy is concentrated in a small area. A photon energy of 15 MeV corresponds to a wavelength of 83 fm, located in the γ -region of the electromagnetic spectrum. From [5]. | 4 |
| 2-3 | Left: proton therapy (PT), right: radiotherapy (RT). Proton therapy (PT) shows a lower integral dose than radiotherapy (RT). From [6]. | 5 |
| 2-4 | The immobilization procedure consists of several subsystems. A setup strategy can be chosen by starting at step 1 (the initial patient placement) and then traversing the tree downwards. Several alignment strategies are listed in Table 2-1. The strategy that will be used for the adaptive immobilization device is highlighted. . | 6 |
| 2-5 | A five-point mask by Qfix. This particular mask keeps the eyes and nose free for improved comfort. Note that by omitting the nose bridge the rotational fixation in CC-direction is worsened. From [28]. | 8 |
| 2-6 | Regions-of-interest (ROI) on a X-Ray image from a stereoscopic setup. From [34]. | 9 |
| 2-7 | An example of a 3D-2D registration. From [35]. | 9 |
| 3-1 | A sagittal view of the global and local alignment errors after a treatment couch correction. The global error is shown in blue, the local errors of the individual regions-of-interest (ROIs) in red. One can see that the global alignment is satisfied, but locally the alignment errors are still quite large. The alignment errors are scaled for better visibility. From [18]. | 14 |
| 4-1 | The chosen concept (see Table D-1; red line). Listed: The head and neck are enclosed for maximum fixation (1). Membrane actuators; inflatable balloons (2). The head and neck are clamped into place by the actuators (3). The immobilization device is rigidly connected to the treatment couch (4). There are three actuators on each side and two at the back of the head and neck. The face is uncovered for improved patient comfort. | 20 |

| | | |
|------|---|----|
| 4-2 | Top: male and female head breadth distribution [48]. The means are given by the dotted lines. Bottom: the different immobilization device sizes. Note that there is some overlap between sizes. This is because it is desired to have some sizes centered around the mean breadths for males and females. These sizes are sufficient to fit 99.7% of the patients (± 3 SD). | 21 |
| 4-3 | The effect of rotations and translations of the treatment couch on the proton beam attenuation. The immobilization device is fixed to the treatment couch. The clinical target volume (CTV) is denoted by the plus symbol and the arrows denote the two beam angles. As it turns out from Eq. (4-1) the effect of the rotations is negligible therefore the design to the left is chosen. Note that due to the shape of the head some curvature must be introduced to keep the material thickness to a minimum. | 22 |
| 4-4 | A comparison of four different air channel types. From left to right: a single large channel, multiple smaller channels, a wedge-shaped channel and a porous structure that lets air through. For the wedge-shaped channel extra material is added to the outside. | 22 |
| 5-1 | A cross-sectional view of a membrane and piston. The proton beam attenuation of the membrane is largely independent of the point of incidence and the angle of incidence of the proton beam. In contrast to the membrane the piston is sensitive to this. | 24 |
| 5-2 | The placement of the actuators is shown for a simplified model of the head and neck. The effective rotation center is located at vertebra C4. Given dimensions are of a median male (height 1.74 m) [49]: $L_1 = 65$ mm, $L_2 = 59$ mm, $L_3 = 43$ mm, $L_4 = 57$ mm, $L_5 = 110$ mm. For the placement of the actuators the neck is approximated by a wire flexure. | 24 |
| 5-3 | Actuator configuration of the back of the head and neck. The goal is to minimize parasitic forces in the cranial-caudal (CC) direction due to forces applied in anterior-posterior (AP) direction. | 26 |
| 5-4 | A single actuator module. From left to right: an inflatable membrane, a long flexible tube (longer than shown), a pressure sensor, a piston, a lead screw, a limit switch and finally the stepper motor. | 28 |
| 5-5 | Deformation profiles of a cross-section of the membrane. Only half of the cross-section is simulated since the membrane is axisymmetric. From [55]. | 34 |
| 5-5a | Free inflation from the reference configuration. The line tensions T_ξ and T_ϕ are related to the strain energy function W . | 34 |
| 5-5b | An overview of the different boundary conditions for free and constrained inflation. For a more detailed overview see Table 5-6. | 34 |
| 5-6 | Free inflation of the membrane. The limit-point is unstable and a pressure beyond this value will cause the membrane to grow uncontrollably. Therefore the pressures in the system are kept below this value. | 36 |
| 5-7 | The actuator stiffness at the nominal clamping force. The minimum stiffness requirements are satisfied over the full working range. | 39 |
| 5-8 | The deformation profile for constrained inflation with no-slip boundary conditions. All values are dimensionless which indicates that the deformation profile is similar for all spherical membranes. | 40 |
| 5-9 | A comparison of free inflation and constrained inflation (frictionless and no-slip). The isolines denote a constant distance to the surface (in millimeters). For free inflation the pressure will follow the dotted line. This plot enables us to estimate the distance to the surface as well as (with a similar plot) the force that is generated by the actuator. | 40 |

- 5-10 The test setup for validation of the membrane actuator model. The parts are: a 9 V power supply (1), a micro-controller (ATmega328P) and stepper motor driver (2), a 1.2 MPa pressure sensor (3), the pneumatic source (4), the membrane pressing against a 100 N force sensor (5) and a signal amplifier together with an analog to digital converter (ADC) for the force sensor (6). In the end the force sensor was replaced by a universal testing machine (compression tester). With this machine the position could be controlled and the forces measured simultaneously. 41
- 5-11 The test setup of the membrane using a compression tester. This machine can control the position and measure the forces simultaneously. The membrane presses against a plate which is connected to a force sensor. In both pictures the flexible tube going from the piston to the membrane is visible in the bottom. 42
- 5-11a A front view of the machine. 42
- 5-11b A close-up of the membrane (shown in orange). The size of the actuator is shown by the circle. 42
- 5-12 The membrane pressure and force for a given input and contact surface distance. The continuous lines denote the model and the circles denote the measurements. It can be seen that the model is accurate. A slight hysteresis can be noticed in the measurements. During inflation the pressure sensor registers a slightly higher pressure than during deflation. This is because the sensor is mounted at the piston and the narrow tube restricts the air flow a little. Similarly, the force also lags behind. 43
- 5-12a The membrane pressure for a given input and contact surface distance. These measurements are used to fit the parameters listed in Table 5-8. 43
- 5-12b The actuator force for a given input and contact surface distance. These measurements are used to verify the model. The force estimation becomes less accurate for larger distances. 43
- 5-13 The stiffness of the side actuator at the nominal preload force (15 N). The minimum stiffness requirements are satisfied. For short distances the stiffness is underestimated by the model. 43
- 5-14 The distance to the contact surface can be estimated given the input and the measured pressure. The y-axis is shown on the right to better illustrate the estimation performance. For each specified distance the membrane is inflated fully. If the distance is small it can already be estimated for low input values. If the distance is large the estimation becomes a more unreliable. At the end of the working range the difference between free inflation and constrained inflation becomes small. The estimated distance must always lie below the dotted line (the maximum deflection for free inflation). 44
- 6-1 Left: the measurement setup with an applied force F resulting in a displacement y . The center of rotation is the cervical joint at T1 - C7 with $L_1 + L_2 = 230.4$ mm. Right: a setup that produces the same displacement for an identical force (assuming a small angle approximation). A prismatic joint has been added to reflect translations of the neck. The center of rotation depends on the location of the corresponding joints and is listed in Table 6-3. 47
- 6-2 The series manipulator of the head and neck with the skull as end-effector. First there are two prismatic joints (q_1 and q_2) attached to the body (more specifically T1, the first of the thoracic vertebrae). Then there are three consecutive revolute joints ($q_3 - q_5$), with at the end the skull. 50
- 6-3 Left: the standard model that is used to calculate the pose of the ROIs. Right: the model where the remaining vertebrae of the neck are added through inverse kinematics. Although the body is not shown on the left, it can still be referenced as a ROI. 53

| | | |
|-----|---|----|
| 6-4 | An approximation of the membrane profile under compression. The symbols are: R is the radius of the membrane in the undeformed configuration and r_0 is the initial actuation axis. $\delta(u)$ is the deflection of the membrane during free inflation. $R_0(u)$ is the radius of the corresponding sphere with $p_0 = p_\mu(q) + (\delta(u) - R_0(u))\hat{r}_0$ as the origin. $p_\mu(q)$ and $p_\nu(q)$ (shown in green) denote the attachment points of the virtual spring to joints μ and ν . These two points follow directly from the kinematic model. $d(q, u)$ is the distance between both surfaces (also called the stroke of the actuator) and $x(q, u)$ is the compression. $a(q, u)$ is the radius of the circular contact area. The contact area is always perpendicular to the actuation axis $r(q, u)$. This also shows that, as long as the compression is constant, the volume of the membrane is independent of the actuation angle ($\beta(q, u)$). This means that the actuator force is independent of the actuation angle. | 55 |
| 7-1 | The alignment procedure at the start of each fraction. The number of corrections is to be kept as small as possible. Each iteration a single correction is performed. The current iteration is denoted by k and the maximum number of iterations by N | 58 |
| 7-2 | The 3D mesh of the head and neck [74] used to find the contact points of the actuators. A ray-triangle intersection algorithm [75] is implemented to find the intersection point of the actuators (rays) with the 3D mesh (triangles). The head is scaled to match the dimensions used in the rest of the model. From left to right: A lateral view showing the five independent actuators. An anterior view showing the two sets of three actuators on opposing sides of the head. Only three of these actuators are linearly independent. And lastly, another overview of the head. | 69 |
| 7-3 | The median of the rotational and translational errors of the head and neck for consecutive corrections (iterations). In both cases the translational error requirements are fulfilled after one iteration. Only in the case without force correction the rotational error requirements are also satisfied. | 71 |
| | 7-3a Without force correction. | 71 |
| | 7-3b With force correction. | 71 |
| 7-4 | The probability of exceeding a given error, either rotational or translational. A comparison of different controller options is given. The abbreviations are: with (w/), without (w/o), force correction (FC), and observer (OB). The observer increases the performance of the controller slightly, both with and without force correction. The force correction decreases the performance significantly. | 71 |
| | 7-4a After one iteration. The effect of the observer is not yet noticeable. | 71 |
| | 7-4b After four iterations. The observer decreases the alignment error except in some cases. In extreme cases the observer cannot find the correct state. | 71 |
| 7-5 | An evaluation of the observer performance. Shown are the rotational and translational errors between the real pose and estimated pose. The abbreviations are: with (w/), without (w/o), force correction (FC), and observer (OB). The results are averaged over 100 simulations. The observer improves the localization performance. The errors of the pure measurements are constant and agree with the chi distribution (Appendix B-3). Namely: $\mu_{\text{rot}} = 1.60 \cdot 0.3 = 0.48^\circ$ and $\mu_{\text{rot}} = 1.60 \cdot 0.4 = 0.64 \text{ mm}$ | 72 |
| 7-6 | The alignment errors for systems with more than two ROIs. Vertebra C5 was added to the model using inverse kinematics as described by Section 6-2-2. It is mostly responsible for the large rotational errors. In both cases the rotational error exceeds the given requirements. The translational alignment is sufficient after two iterations. | 73 |
| | 7-6a Measured ROIs: the body, C5, C2 and the skull. The translational error after one iteration has a lot of variation. Although the median is well below the dotted line, the upper whisker extends to 6.5 mm. | 73 |

| | | |
|------|---|----|
| 7-6b | Measured ROIs: C5, C2 and the skull. This time the initial body offset is approximately doubled. As a result the rotational error also doubles. | 73 |
| 7-7 | A case with only a single ROIs, namely the skull. A system with a single ROI is not observable (Section 7-2-2). The control input is compared to that of Fig. 7-3b. | 74 |
| 7-7a | The errors are comparable to that of Fig. 7-3a. In all cases the error requirements are fulfilled. | 74 |
| 7-7b | The control input (averaged per category) to the treatment couch and actuators, averaged over 100 simulations. What is shown is the difference in control input from one iteration to the next. It is interesting to see that in both cases, while the error stabilizes after a single iteration, the control input is never constant. | 74 |
| 7-8 | The effect of force correction on the alignment. The reference case is without force correction, which understandably results in the best alignment. Note that the translational alignment remains largely unchanged. | 75 |
| 7-9 | Estimation of model parameters and the effect on the alignment over a duration of ten fractions (a typical treatment consists of 30 fractions). The estimated parameters are the neck length and the mass of the head. The length is estimated correctly after approximately five fractions while the mass cannot be observed. The real values are given by Eq. (7-40) or by the dotted lines in the figure. This simulation was performed without any measurement noise. The variation of the alignment error is due to the random body offset at the beginning of each fraction. It can be seen that even without noise in the system the performance gain is very small (approximately $4 \times 10^{-3^\circ}$ for rotations and 0.015 mm for translations). | 76 |
| 7-10 | A dual actuator setup clamping a simple cantilever beam. This setup serves as a proof of principle. | 76 |
| A-1 | Directional terms applied to the human body. From [76]. | 81 |
| A-2 | The skeletal system of the head and neck. From [77]. | 82 |
| B-1 | An example of how the alignment errors are calculated. For example: the values indicate the translational error in millimeters in LR-direction. From [38]. | 83 |
| D-1 | The indexable couch top is identical for each concept. The cranial part of the couch top (1) supports the head and neck and is rigidly attached to the immobilization device. The caudal part of the couch top (2) supports the body. The indexation pins (3) ensure a repeatable and secure connection to the treatment couch. | 87 |
| D-2 | Concept 1, as denoted by the red line in Table D-1. Left: lateral view, right: anterior view. Inflatable membranes (2). The head and neck are clamped into place by the actuators (3). The head and neck are enclosed for maximum fixation (1). The immobilization device is rigidly connected to the treatment couch (4). | 89 |
| D-3 | Concept 2, as denoted by the green line in Table D-1. Left: lateral view, right: anterior view. To reduce artifacts in the CT scan, the actuators are moved away from the neck and towards the head as much as possible. The entire upper part of the skull can be seen as rigid and is therefore easier to register. Lead screw stepper motors (2). The intermediate platform for the translation in left-right (LR) direction and rotation in AP direction (4). The head is lightly supported and the ears are not obstructed (1). A cushion provides comfort and a better fixation (3). Elastic foam presses firmly on the sides of the back of the head to keep it in place and not distort the imaged surface (5). The immobilization device is not directly fixed to the treatment couch (6). | 90 |

| | | |
|-----|---|----|
| D-4 | Concept 3, as denoted by the blue line in Table D-1. Left: lateral view, right: anterior view. Electric servo motors (2). A Stewart platform for six degree of freedom (DOF) motion (4). The head and neck are enclosed for maximum fixation (1). A cushion provides comfort and a better fixation (3). Elastic foam presses firmly on the sides of the head to keep it in place (5). The immobilization device is not fixed to the treatment couch (6). IR-markers on a bite-block and on the neck and shoulders for the localization of the ROIs (7). | 91 |
| E-1 | Stiffness mechanisms. For $x/\delta \ll 1$ the stiffness is primarily due to the change of contact area of the membrane. | 95 |
| E-2 | Change of area for different geometries. | 95 |

List of Tables

| | | |
|-----|--|----|
| 2-1 | Several strategies for the alignment of the CTV. The numbers refer to the steps in Fig. 2-4. A vinculum (e.g. $\overline{3b - 6a}$) is used to denote a repeating set of steps. The strategies itself are repeated every fraction. | 7 |
| 2-2 | State-of-the-art alignment errors for most subsystems shown in Fig. 2-4. The errors in LR, CC and AP directions (Fig. A-1) are considered independent and are therefore combined to a single 1D error. The same is done for the rotations. The 1D errors are assumed to be independent and identically distributed (IID) with a zero mean. | 11 |
| 3-1 | The requirements for the 1D alignment error of the immobilization device (in combination with a treatment couch correction). The desired error is approximately half that of the current rigid body correction errors (which are: 0.7° for rotations and 1.2 mm for translations). | 16 |
| 5-1 | All the possible wrenches (along one of the three axes) that constrain the head along the left-right (LR) and anterior-posterior (AP) direction. The variables x and y can be chosen freely. | 27 |
| 5-2 | The placement of the side actuators ($A_1 - A_3$) and back actuators (A_4 and A_5). The center of gravity is located at: $u = [0 \ 0.176 \ 0.027]$ [51]. A wrench is calculated as: $W = [u \times fr + mr \ fr]$, where $r \in \mathbb{R}^3$ is the actuation axis and $u \in \mathbb{R}^3$ is a point on this axis. f and m are the scalar force and moment, respectively. These wrenches span the same constraint space as Π_W | 27 |
| 5-3 | Maximum voluntary moments generated by the neck and the corresponding myoelectric signal levels [53]. The subconscious moments are estimated at 5% of the maximum voluntarily moments. Measured with vertebra C4 as the center of rotation. Standard deviations are shown in parenthesis. | 29 |
| 5-4 | An overview of the minimum actuator stiffnesses to ensure that the maximum errors are not exceeded. The maximum errors are $\theta_{\max} = 0.3^\circ$ for the rotations and $\delta_{\max} = 0.6$ mm for the translations. These are specified by the requirements (σ_{device} ; Table 3-1). The subconsciously generated are listed in Table 5-3. The dimensions are given by Fig. 5-2. | 30 |
| 5-5 | The design constraints that follow from the actuator requirements. | 31 |
| 5-6 | Boundary conditions for free inflation and constrained inflation, both frictionless and no-slip. These boundary conditions are specified by Long et al. [55]. | 36 |

| | | |
|-----|--|----|
| 5-7 | The lower and upper bounds of the actuator parameters that are to be optimized. The parameters are collected in $\theta = [h_0 \ R_{\text{side}} \ R_{\text{back}} \ V_{\text{side}} \ V_{\text{back}}]$. The optimal values are displayed in the last column. The Young's modulus of the membrane is assumed $E = 1.4 \text{ MPa}$ and the volume of the tubes is $V_{\text{tube}} = \text{mL}$ ($L_{\text{tube}} = 2 \text{ m}$). | 39 |
| 5-8 | The parameters of the actuator module before and after fitting. | 42 |
| 6-1 | Model parameters for a median male. | 46 |
| 6-2 | Range of motion of the neck (5th - 95th percentiles). Males and females combined. | 46 |
| 6-3 | Passive stiffness values of the neck for an average male. Values for the average female are shown in parenthesis [63]. The equivalent stiffness is calculated by Eqs. (6-1) and (6-2) using dimensions from Table 6-1. | 48 |
| 6-4 | A screw description of the joints in the kinematic chain. The dimensions are from [49]. The transform from joint C1-skull to the center of gravity is fixed. . . | 49 |
| 7-1 | Objective function and constraints for the optimization. | 65 |
| 7-2 | 1D alignment errors in the three directions: LR, cranial-caudal (CC) and AP. These correspond to the X-, Y-, and Z-axis in Fig. 6-2, respectively. Only the rotational error in AP-direction (highlighted) is significantly impacted by the force correction. The errors are compared to values found in literature. | 70 |
| 7-3 | A comparison of the alignment errors between the state-of-the-art, the desired errors given by the requirements and the errors resulting from the simulations. . . | 72 |
| 7-4 | Fixation errors due to an applied moment. The magnitude of this moment is determined by the subconsciously generated moments listed in Table 5-3. The errors are below those specified by the requirements, indicating that the fixation is satisfactory. | 74 |
| B-1 | The local alignment errors of the regions-of-interest (ROIs) after a rigid body correction. Several correction methods are compared. It can be seen that the random error increases with the number of ROIs. This is because local errors are not averaged out. Compare it with a single ROI where the error after correction is approximately to zero. | 84 |
| D-1 | The morphological chart used to design three concepts. The red, green and blue lines denote concepts 1, 2 and 3 respectively. | 88 |
| E-1 | A comparison of the contribution to the change of area effect due to different membrane geometries | 94 |

Acknowledgments

I would like to give thanks to my supervisors: prof.dr.ir. M. Verhaegen and ir. J.W. Spronck for guiding me in this thesis. Their constructive criticism and enthusiasm was greatly appreciated. I would also like to thank my other committee members: prof.dr.ir. J.L. Herder and dr. E. Steur for taking the time to read this work and judge it. Lastly, I would like to give special thanks to drs. N. Holtzer for helping me during my time at HollandPTC. It allowed me to learn from the experiences of people working in a proton therapy center.

Delft, University of Technology
September 27, 2018

A.M. Brouwer

Chapter 1

Introduction

Every year 100,000 new cases of cancer are diagnosed in the Netherlands [1]. 45–47% of which are treated with radiotherapy (RT) [2]. In RT malignant cells are killed using ionizing radiation. Typically this ionization is due to high energy photons such as X-rays or gamma rays. An alternative ionization method, called proton therapy (PT), is becoming increasingly popular. PT uses a beam of protons instead of photons to irradiate the targeted cells. It offers a higher dose conformity (i.e. a more precise dose deposition) and a lower integral dose than conventional RT. This makes it suitable for treating tumors close to critical organs, e.g. in the head and neck region. Approximately 3% of the RT cases are eligible for PT. Due to its high conformity, a good estimate of the tumor location is essential. This study will therefore focus on improving the tumor alignment with respect to the initial planning-CT (pCT). Only tumors in the head and neck will be considered.

First some of the background on PT is explained in Chapter 2: what is an immobilization device and why is it necessary? Then in Chapter 3 some problems with current immobilization devices are listed and the research objective is stated. Also some requirements are listed that must be fulfilled by the design. Next is the design of a concept for the immobilization device in Chapter 4. This concept uses membrane actuators which are considered in Chapter 5. In Chapter 6 the anatomical model is defined as well as the methods to simulate it. The controller is designed in Chapter 7. This chapter also contains the results of the simulations. Finally, the conclusion is given in Chapter 8 and the recommendations for future research in Chapter 9.

Proton Therapy: Background

In this chapter some background information on proton therapy (PT) is given. While the treatment process is similar to that of radiotherapy (RT), there are some technical differences that make PT a more suitable candidate for head and neck patients.

2-1 Tumor: Clinical Target Volume

When it comes to the tumor, three volume types are distinguished. The smallest is the gross tumor volume (GTV). This is the tumor as it is visible on the medical images. Typically not all malignant cells are visible. Therefore the volume is increased slightly to account for microscopic tumor spread. This is called the clinical target volume (CTV) and is actually the volume that needs to be irradiated. Due to errors and uncertainties in the setup the margins are increased once again to make sure that everything gets enough radiation. This is called the planning target volume (PTV). This margin is usually a function of the alignment errors of the immobilization device (Section 2-5).

2-2 Protons vs. Photons

The protons are first accelerated by a particle accelerator and then pass through a range modulator where the energy is decreased to a usable range of 70–250 MeV. The protons are transported to the treatment room and exit the nozzle in the gantry. The gantry can rotate around the patient to treat the tumor from different angles. In Fig. 2-1 a typical gantry is shown.

In Fig. 2-2 the main advantage of PT becomes clear. Due to the Bragg peak, PT has a higher dose conformity than RT. This means that it can better handle complex CTV shapes. By modulating the proton beam energy a superposition of multiple peaks is created. This is called the spread-out Bragg peak (SOBP) and is used to give a constant dose to the entire tumor volume. Another advantage is the finite range of protons. This means that the tissues distal to the tumor are spared. This effect is shown in Fig. 2-3. It is also better suited for treating children who have a higher lifetime risk of secondary cancer [4].



Figure 2-1: A typical treatment room. Inside the gantry are shown: the treatment couch (blue), the proton beam nozzle (orange) and two orthogonal X-ray imaging detectors (yellow). Sometimes an optional CT device is placed in the same room for faster and more precise imaging. From [3].

One effect that is present (and often exploited) in RT and not in PT is the skin-sparing effect. Figure 2-2 shows that the radiation dose close to the skin is lower than that a few centimeters deeper. However, the absence of this effect makes the dose deposition of protons more predictable than that of photons.

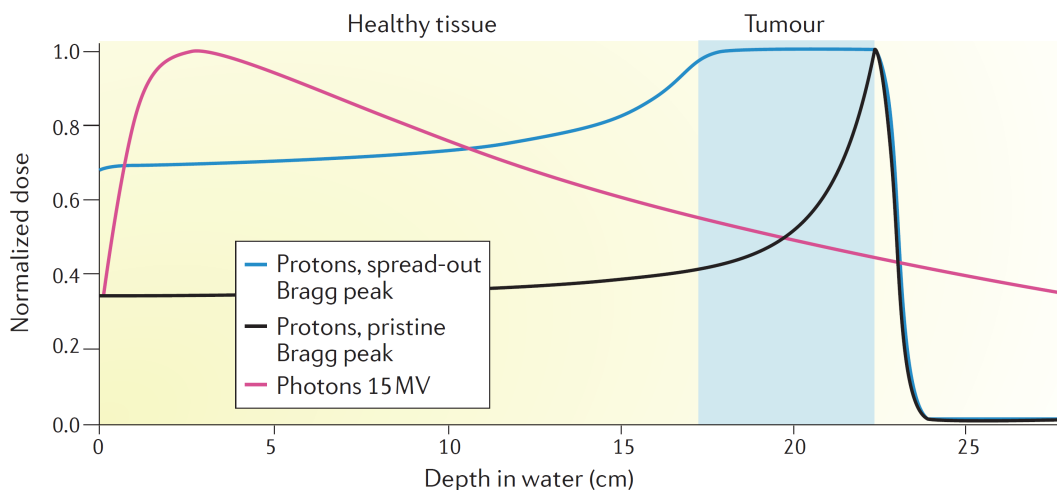


Figure 2-2: The dose distribution of protons compared to photons. The Bragg peak is where the protons start decelerating rapidly which is why all the energy is concentrated in a small area. A photon energy of 15 MeV corresponds to a wavelength of 83 fm, located in the γ -region of the electromagnetic spectrum. From [5].

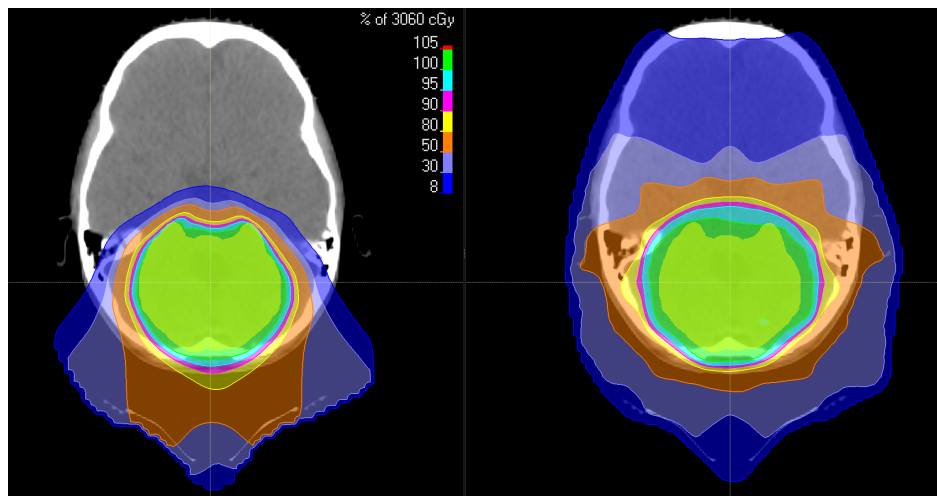


Figure 2-3: Left: proton therapy (PT), right: radiotherapy (RT). PT shows a lower integral dose than RT. From [6].

2-3 Treatment Process

The treatment process of a patient is split up into several sessions, so-called fractions. It depends on the tumor but on average it takes about 30 fractions in 5 weeks. The treatment process of PT is similar to that of RT and consists of the following steps:

1. **Diagnosis:** The patient is first diagnosed. If the patient is eligible for PT they are referred to a specialized facility.
2. **Consult:** The patient is made familiar with the treatment process. Any questions or concerns are answered.
3. **Initial setup:** The patient is aligned on the treatment couch. An immobilization device is customized and fitted for the patient.
4. **Imaging:** A detailed CT scan is made which is later used to design the treatment plan on. This scan is called the planning-CT (pCT). Often a MRI or PET/CT is made as well for additional information.
5. **Planning:** The pCT is used by the radiation oncologist to determine where and how much dose needs to be given. The treatment planner then optimizes the treatment plan based on the pCT. This plan is identical for every fraction and is used to direct the proton beam.
6. **Quality assurance (QA):** The treatment plan is checked using a phantom. This QA step is done to ensure that the proton beam angles and intensities are correct.
7. **Irradiation:** The patient is aligned on the treatment couch and immobilized. The patient is then irradiated according to the treatment plan. This step is repeated for every fraction. A single fraction can take anywhere from 25 to 35 minutes, although the proton beam is usually only active for approximately one minute [7].
8. **Follow-up:** After the final fraction a follow-up is planned. This follow-up is a check for how successful the treatment was and whether additional treatment is necessary.

2-4 Current Immobilization Methods

In most cases the CTV cannot be observed directly. A solution is to immobilize the patient such that the CTV is at a fixed location in a known reference frame. This process is called stereotaxy. The most important properties of an immobilization device are its precision and its fixation. The accuracy is not important since the pCT will be made using the same device. Therefore any initial misalignment will be accounted for. If any form of correction is used, the precision of the device also becomes less important. If the patient is misaligned due to a poor precision, it will be detected and corrected, e.g. by moving the treatment couch. Therefore, an immobilization device that is used in combination with a correction primarily requires a good fixation.

There are several strategies for immobilizing the head and neck. Figure 2-4 aims to give a clear overview of the possibilities. When traversing down the tree, different alignment strategies can be identified. Several of these strategies are listed in Table 2-1. The highlighted strategy will be the guideline for the design of the adaptive immobilization device.

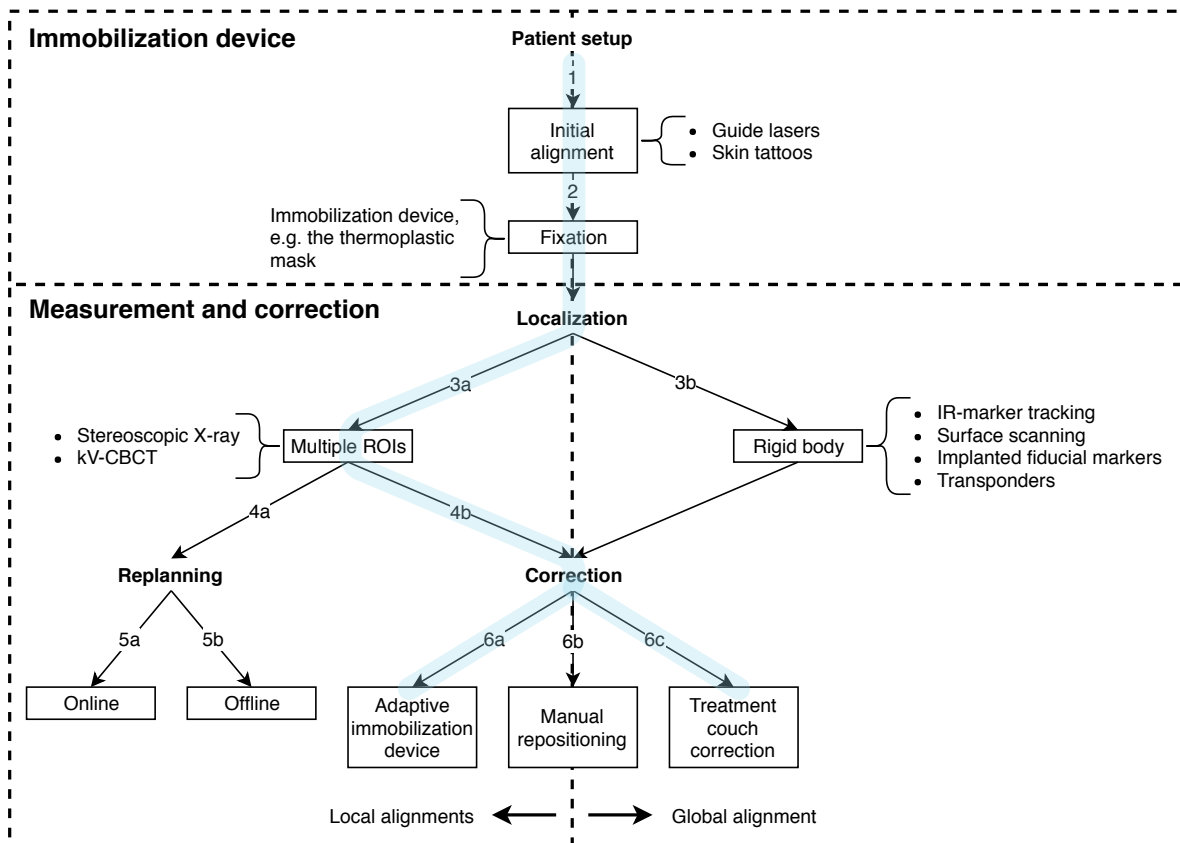


Figure 2-4: The immobilization procedure consists of several subsystems. A setup strategy can be chosen by starting at step 1 (the initial patient placement) and then traversing the tree downwards. Several alignment strategies are listed in Table 2-1. The strategy that will be used for the adaptive immobilization device is highlighted.

Table 2-1: Several strategies for the alignment of the CTV. The numbers refer to the steps in Fig. 2-4. A vinculum (e.g. $\overline{3b - 6a}$) is used to denote a repeating set of steps. The strategies itself are repeated every fraction.

| Strategy (Fig. 2-4) | Description | Examples in literature |
|--|--|---------------------------|
| 1 – 2 | This strategy does not check alignment errors. It is mainly used in old setups or single fraction treatments, e.g. stereotactic radiosurgery (SRS). | [8–11] |
| 1 – 2 – 3a – 4b – 6c or sometimes: 1 – 2 – 3b – 4b – 6c | This strategy is commonly used in combination with a thermoplastic mask. Sometimes step 6c is substituted by 6b if the misalignment is too large or impossible to correct. | [12–22] |
| 1 – 2 – 3a – 4a – 5b | This is an offline replanning strategy. This replanning is not necessarily done every fraction. It can be alternated with other strategies. | [18, 20, 23] |
| 1 – 2 – 3a – 4a – 5a | This is an online replanning strategy. | [24] |
| 1 – 2 – $\overline{3b - 6a}$ | This is an immobilization strategy that performs corrections based on the global misalignment. | [25, 26] |
| 1 – 2 – $\overline{3a - 4b - 6a}$ or sometimes: $\overline{1 - 2 - 3a - 4b - 6c - 6a}$ | This is an immobilization strategy that performs corrections based on local misalignments This strategy is highlighted in Fig. 2-4 and used in Chapter 7. | - |

2-4-1 Immobilization of the Head and Neck

Although the quality of the alignment and fixation mostly depends on the immobilization strategy, it must be noted that it is also largely influenced by the experience and time constraints of the radiographer [27]. For the alignment of a patient on the treatment couch often a laser guidance system is used.

The thermoplastic mask is currently the most used frameless immobilization device for the head and neck. These masks come in a few sizes. A three-point mask only immobilizes the head but a five-point mask also immobilizes the neck and shoulders. In Fig. 2-5 such a mask is shown. The mask begins as a flat mesh of plastic and is heated in a bath of water to a temperature of 70–75 °C [10]. At that temperature it becomes soft and malleable. It is then formed and molded around the patient’s head, neck and shoulders making sure to take advantage of anatomical features. After approximately 10 minutes it cools down and hardens again. Sometimes during the treatment the mask does not fit anymore. In this case a new mask must be made. For this new mask steps 3–6 of the treatment process (Section 2-3) must be repeated. This is not only time-consuming but also a costly process.

Body supports are a collection of modular wedges and cushions that help with the fixation of the body on the treatment couch. They can be combined with other immobilization devices to



Figure 2-5: A five-point mask by Qfix. This particular mask keeps the eyes and nose free for improved comfort. Note that by omitting the nose bridge the rotational fixation in CC-direction is worsened. From [28].

increase the precision. Houweling et al. [29] has demonstrated that a customized head cushion significantly reduces alignment errors when used in combination with a thermoplastic mask.

2-4-2 Localization of the CTV

The process of measuring the pose of the CTV, i.e. its location and orientation, is called localization and is necessary to calculate alignment errors. Often the CTV cannot be localized directly. It is then correlated to reference geometry that can be localized. Anatomical features that are used as a reference are called regions-of-interest (ROIs). Whereas a rigid-body localization method only measures a single ROI, deformable localization methods can measure multiple ROIs. In ear, nose and throat (ENT) patients the CTV can span from the head all the way down to the collarbones. Motion between the head and neck can then lead to significant measurement errors if using a rigid body localization method [30].

A common deformable localization method is stereoscopic X-ray imaging. It is the process of making two orthogonal projections of the patient through the isocenter. An example of such a projection is shown in Fig. 2-6. These 2D projections of the head and neck are then correlated to the 3D volumetric CT-scan (which was made during the planning process) in a process referred to as 3D-2D registration. This is shown in Fig. 2-7. From this registration the alignment error of each of the ROIs is calculated. These errors will be called the local alignment errors. The error of a rigid-body localization method will be referred to as a global alignment error.

A stereoscopic X-ray imaging setup is shown in Fig. 2-1. One of the downsides of this method is that it does not provide good soft tissue contrast [31]. That problem can be mitigated by only registering bony anatomy. In the head and neck region tumors are namely attached to bony anatomy [32, 33]. Another downside is that each measurement gives an

undesirable extra dose to the patient. Even though the dose given by the X-ray images is low, at <0.3 mGy/image [34]. Yet another disadvantage is that the 3D-2D registration can take up to several minutes [35]. Hence the number of measurements must be kept as low as possible. Despite these disadvantages, such a method is essential if one wants to measure the local alignment errors.

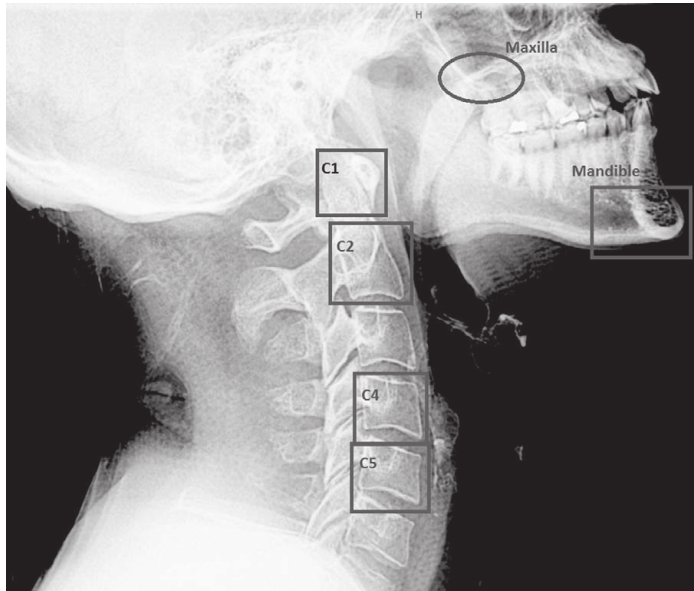


Figure 2-6: Regions-of-interest (ROI) on a X-Ray image from a stereoscopic setup. From [34].



Figure 2-7: An example of a 3D-2D registration. From [35].

2-4-3 Correction Methods

Alignment errors can be reduced by various forms of correction. A correction means that the patient is moved either manually or automatically to the desired pose, which is generally the reference pose. Daily corrections can reduce the PTV margins considerably [21].

Most treatment couches offer the ability to perform four or six degree of freedom (DOF) corrections (three translations and one or three rotations). It can only be used to correct global alignment errors. An example of a six DOF treatment couch is shown in Fig. 2-1. Correcting rotations can halve the variance of residual translations [21]. Care must be taken to not correct the rotations too much, especially if the patient is not adequately fixed. This can lead to shifting of the patient on the couch [16]. However, if the patient is adequately fixed, corrections $<4.4^\circ$ are not perceived as uncomfortable [36].

Sometimes an automatic correction cannot be performed. In that case the patient must be aligned manually by the radiographer. For a thermoplastic mask this means removing the mask, relocating the patient and reattaching the mask. Some research has been done in correcting head misalignments with a motorized head support [25, 26]. Using this device the head can be aligned relative to the body. Despite its potential the device is not suited for use in proton therapy due to its construction. It is not commercially available.

2-5 Alignment Errors: Cause and Effect

In Section 2-4 it was stated that the most important properties of an immobilization device are its precision and its fixation. The fixation error is generally small compared to the precision. Intrafraction motion, i.e. motion during the fraction, is therefore often neglected [19, 27, 33, 37].

In the literature errors are traditionally expressed with the following quantities:

- **The group systematic error (M)** - This is the mean of all means and a measure for the imprecisions in the setup, e.g. a misalignment of the guiding lasers or an offset in the table. This error is identical for every fraction and every patient. Usually this error is small (<1 mm).
- **The standard deviation (SD) of the systematic error (Σ)** - This is a measure of the reproducibility of the treatment process, e.g. an error in the delineation of the CTV or the construction of the thermoplastic mask. This error is identical for every fraction of a single patient. The relaxation of the patient after several fractions can also contribute to this error.
- **The SD of the random error (σ)** - This is a measure for the reproducibility of the alignment. This error is different for every fraction and every patient. It is generally smaller than the SD of the systematic error [27]. It is increased by anatomical changes such as tumor shrinkage or weight loss, causing the immobilization to be less reproducible.

In calculating these errors it is assumed that they are independent in the three directions: left-right (LR), cranial-caudal (CC) and anterior-posterior (AP) [16] (see Fig. A-1 for the directional terms). Translational errors are also found to be independent of rotational errors [30]. If the CTV is small or symmetric, rotations around the isocenter are often neglected [27]. However, for elongated CTVs, even small rotations can result in significant displacements at the ends [30].

There are several different recipes to calculate the margins of the PTV. A common recipe is: $2.5\Sigma + 0.7\sigma$ by van Herk [38]. It ensures that 90% of the patients receive a minimum dose of 95% of the prescribed dose to the CTV. From this recipe it becomes clear that systematic errors are more important than random errors. Some effort has been made in the development of variable margins for relative deformations but this is not widely implemented [39].

The SD of the random error (σ) describes the precision (or repeatability) of the device. It is used to compare the state-of-the-art errors to the calculated alignment errors. In Table 2-2 state-of-the-art errors are listed of the various subsystems shown in Fig. 2-4.

Table 2-2: State-of-the-art alignment errors for most subsystems shown in Fig. 2-4. The errors in LR, CC and AP directions (Fig. A-1) are considered independent and are therefore combined to a single 1D error. The same is done for the rotations. The 1D errors are assumed to be independent and identically distributed (IID) with a zero mean.

| | SD Translations (mm) | SD Rotations (deg) |
|--------------------------|----------------------|--------------------|
| CTV fixation | | |
| Thermoplastic mask | 1.7 | 1.5 |
| Scotchcast mask | 2.0 | 1.2 |
| Localization | | |
| Stereoscopic X-ray | 0.4 | 0.3 |
| Cone-beam CT | 0.2 | 0.2 |
| IR tracking | 0.2 | 0.1 |
| Surface scanning | 0.5 | 0.1 |
| Transponders | 1.2 | 0.8 |
| Correction | | |
| Adaptive ¹ | 0.6 | 0.3 |
| Manual ² | 1.7 | 1.5 |
| Couch | 0.1 | 0.05 |
| Proton beam ³ | | |
| Range | 1.6 | - |
| Spread | 1.0 | - |

¹ Estimated values based on the requirements in Table 3-1. No references of truly adaptive immobilization devices were found.

² Manual correction errors are assumed to be equivalent to initial CTV fixation errors, since the same procedure is followed.

³ For a penetration depth of 5 cm.

Objective and Requirements

Current immobilization methods still have some unsolved problems which are addressed in this chapter. Some objectives are formulated that resolve the most important problems. The objectives are quantified by three types of requirements: the error requirements, the setup requirements and the control requirements.

3-1 Problems of Current Immobilization Methods

The most important problem of current immobilization devices is the inability to correct local misalignments. Other problems include: incorrect application of error margin recipes, the inability to compensate for anatomical changes and the discomfort of wearing such a device.

Local misalignments are substantial and should not be neglected [18, 21, 40]. This is especially a problem for clinical target volumes (CTVs) that cover large areas, have complex shapes or are close to critical organs. The largest of these misalignments is due to a nodding motion of the head which is hard to eliminate with current setups [19, 21, 33, 34]. This motion is highly correlated with the motion of the skull and the mandible [34, 40]. The neck also shows relatively large errors because it cannot be immobilized effectively [40, 41]. Furthermore, a rigid body correction is not sufficient to eliminate the local misalignments (see Table B-1). This is because the local errors are higher than the global errors [40]. The result is that large local errors remain after a correction [18]. This is shown in Fig. 3-1. The root mean square (RMS) value of the remaining errors is 0.7° for rotations and 1.2 mm for translations.

Current error margin recipes assume rigid body translations and become invalid when including rotations and deformations [18, 21, 40]. Some effort has been made in the development of variable margins for deformations, however the effect of geometrical changes on dosimetric changes is not fully understood [18, 39].

Weight loss and tumor shrinkage are common during treatment [40, 42]. The neck was found to be more sensitive to volume changes than the head [21]. The problem is that if the volume decreases too much the patient will be able to move inside the immobilization device.

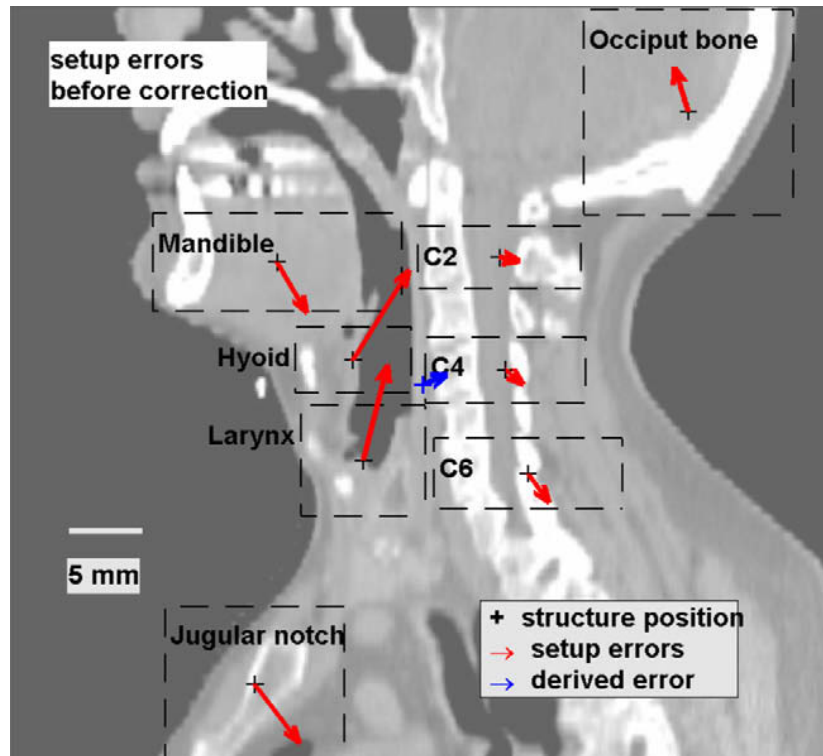


Figure 3-1: A sagittal view of the global and local alignment errors after a treatment couch correction. The global error is shown in blue, the local errors of the individual regions-of-interest (ROIs) in red. One can see that the global alignment is satisfied, but locally the alignment errors are still quite large. The alignment errors are scaled for better visibility. From [18].

This decreased fit will lead to an increased random error. Currently there are no frameless immobilization devices that can compensate for that.

The thermoplastic mask is arguably the most common immobilization device. However, it is quite uncomfortable for the patient [43, 44]. Not only during the molding process but it also tends to be claustrophobic. Shrinkage of the mask is also a common occurrence.

3-2 Objective

The ultimate goal of proton therapy is to cure the patient of its illness using a beam of high energy protons. In order to deliver the dose accurately to the desired location the Bragg curve needs to be estimated (Fig. 2-2). The shape of this curve depends on:

- **The proton energy:** this determines the penetration depth of the protons. It is usually in the range 70–250 MeV.
- **Range straggling:** this is the effect of inelastic collisions of protons with nuclei in the material. The uneven loss of energy results in a wider Bragg peak.
- **The stopping power of the materials:** a CT-calibration curve is used to calculate the relative proton stopping power of the materials from the X-ray attenuation.
- **The material composition:** this determines not only the type of material but also the distance the protons must travel through each material.

The first three are outside the scope of this study, but the last one is related to three of the four problems that were listed in Section 3-1.

The material composition depends on the patient's anatomy, the location of the CTV and the design of both the treatment couch and the immobilization device. More specifically, errors between the predicted material composition and the real material composition are affected by:

- **The alignment error of the CTV with respect to the planning-CT (pCT):** This depends on the immobilization device and used the correction method.
- **The usage and placement of materials in the design of the treatment couch and immobilization device:** The design of the treatment couch will not be investigated but the immobilization device is discussed in Chapter 4. The design of the actuators that are placed inside the immobilization device is discussed in Section 5-1.

Therefore, an objective is formulated that aims to reduce this error.

Objective

Design an immobilization device that:

- Automatically aligns and immobilizes the head and neck
- Is capable of local corrections
- Is transparent to the proton beam
- Is compatible with CT and MRI
- Is comfortable for the patient
- Adapts to the patient

A possible strategy that satisfies the stated objectives is given by $1 - 2 - 3a - 4b - 6c - 6a$ in Fig. 2-4. These objectives will be used throughout this study to motivate design choices.

3-3 Design Requirements

Requirements are formed to quantify the objective. These requirements are split up into three parts: the error requirements, the setup requirements and the control requirements. In the next sections these are listed along with some things to keep in mind if the requirement is to be fulfilled. The requirements that are not explicitly investigated are denoted by an asterisk (*).

3-3-1 Error Requirements

The total alignment error of the setup is given by:

$$\sigma_{\text{total}} = \sqrt{\sigma_{\text{X-ray}} + \sigma_{\text{couch}} + \sigma_{\text{device}}}. \quad (3-1)$$

The desired error is approximately half that of the current rigid body correction errors. The requirements for the rotational errors are then 0.4° and for the translational errors 0.7 mm. This is summarized in Table 3-1. This requirement ensures that, with 95% certainty, the 3D rotational error of the ROIs is $<1.1^\circ$ with a mean of 0.6° . The 3D translational error

is then <1.9 mm with a mean of 1.1 mm. The 3D error follows from the chi distribution (Appendix B-3).

Keep in mind that these new requirements already lead to substantially lower errors than the state-of-the-art can offer.

Table 3-1: The requirements for the 1D alignment error of the immobilization device (in combination with a treatment couch correction). The desired error is approximately half that of the current rigid body correction errors (which are: 0.7° for rotations and 1.2 mm for translations).

| Error | Rotations [deg] | Translations [mm] | Remark |
|--------------------------|-----------------|-------------------|--------------------------------|
| $\sigma_{\text{X-ray}}$ | 0.3 | 0.4 | |
| σ_{couch} | 0.05 | 0.1 | |
| σ_{device} | 0.3 | 0.6 | Requirement for the fixation |
| σ_{total} | 0.4 | 0.7 | Requirement for the controller |

3-3-2 Setup Requirements

The setup requirements are related to the mechanical aspects of the setup:

- **Non-obstructive under CT and MRI** - The used materials must be radiolucent. In the case of MRI-compliance it may not contain any ferromagnetic materials; restrictions also apply to non-ferromagnetic metals.
- **"Invisible" to the proton beam** - The materials must have low or predicable proton stopping powers (e.g. low-Z materials), thin walls, rounded shapes [45] and low density gradients. They must also prevent artifacts such as beam hardening, multiple Coulomb scattering and range straggling.
- **Durable** - The used materials must be resistant to degradation by the proton beam. The setup must also have a decent lifetime and not break down unexpectedly.
- **Robust** - Robust to morphological variations between patients and to external tumors or other abnormalities.
- **Compatible and indexable** - Compatible with existing setups in proton therapy (PT) (and radiotherapy (RT)). Also provide a repeatable and predictable position of the device on the treatment couch.
- **Comfortable** - Non-invasive and painless, give a secure mounting and reassure the patient. It is desired to keep the eyes, mouth, nose and ears clear.
- ***Sterilizable** - It must be possible to clean the device. Alternatively make the contact surfaces disposable.
- ***Safety** - The used materials must be non-toxic and not lead to suffocation or other bodily harm.

3-3-3 Control Requirements

The control requirements are related to the input-output and dynamic aspects of the setup:

- **Sensors:**
 - **CTV localization** - Measure the pose of the individual ROIs.

- **Actuator state** - Measure or estimate the stroke of the actuators and the applied force.
- ***Operating parameters** - Measure relevant operation parameters, e.g. temperature, pressure and humidity.
- **Actuation** - The actuators must be able to withstand intrafraction motion and preferably have a low static power usage. The bandwidth does not have to be high.
- **Controller** - Use a fail-safe, robust control structure. Adapt the controller or model to each individual patient.
- **Fast alignment** - A fast alignment is desired for a high throughput of patients. The number of corrections should be kept as low as possible.
- **Safety** - The forces generated by the setup must be safe. Additionally, setup corrections should be gradual and slow. It must also have a kill-switch that stops the operation and releases the patient. Minimize the dose given to the patient by the X-ray measurements.
- **Give feedback to:**
 - ***The patient** - Give visual, audible or sensible feedback to the patient.
 - **The radiographer** - Notify when the patient is misaligned.
 - ***The gantry** - Stop when the kill-switch is pressed or if the patient is misaligned. Alternatively, use the feedback for gating.

Design of the Immobilization Device

A good immobilization device is important to ensure a low alignment error and to prevent intrafraction motion. There are some constraints in the design of an immobilization device. These are mostly due to the working principle of proton therapy (PT) and medical imaging devices such as CT and MRI. This chapter shows a concept design and some extra things to be aware of.

4-1 Body Fixation

The radiation treatment is an additive process that adds a little dose to the tumor at each fraction. Sudden motions of short duration have a negligible effect on the total dose distribution. Even a frequent motion such as swallowing (a motion of the larynx) results only in a 0.5% difference [46]. Most of the patients complete the treatment without any interruptions [43].

A larger problem is the gradual intrafraction motion of the patient. Studies have found that the type of thermoplastic mask (three-point versus five-point mask) influences the setup uncertainty of the shoulders [47]. This seems to indicate that the intrafraction motion is also affected. However, literature also indicates that the fixation error is generally small compared to the precision, thus intrafraction motion is often neglected [19, 27, 33, 37].

The body and shoulders are assumed to be large enough that no intrafraction motion occurs of the base of the neck. As a result the immobilization device is designed such that it fixes only the head and neck. If fixation of the body is still deemed necessary this device allows for the use of standard body supports, shoulder cushions or shoulder retractors. For these last two, the intrafraction motion of the base of the neck has been found to be small [43].

4-2 Concept Generation and Selection

Functions of the immobilization device were listed in a morphological chart from which three concepts were generated. An overview of this process is shown in Appendix D. In this process functions of the immobilization device were scored and the chosen concept was determined by the highest weighted score. The chosen concept is shown in Fig. 4-1. The shape of the

device is chosen such that the requirements are satisfied. It consists of a lightweight shell that contains eight actuators. There are two actuators at the back of the head and six actuators to the sides. The actuators to the side are placed in opposing pairs. They are not fixed to the head and are limited to a pushing action only.

According to Li et al. [44] 80% of the patients preferred an open mask versus a closed one. Whereas claustrophobic patients could not even tolerate a closed one. Similarly, Zhao et al. [43] found the thermoplastic mask to be constrictive and stressful. In favor of comfort the face is therefore not covered. This also makes it easier to use motion tracking equipment such as infrared (IR) markers or surface scanning. The ears are also unobstructed.

In order to accommodate different head sizes, the immobilization device must either be adjustable or easily swappable. It is chosen for five different sizes that are indexable and can easily be swapped out. The breadth of the head is the deciding factor; the actuators have a limited stroke and must still be able to align the patient. The male and female head breadth and the corresponding device size is given by Fig. 4-2. The different sizes are chosen such that the devices need to be swapped out as little as possible.

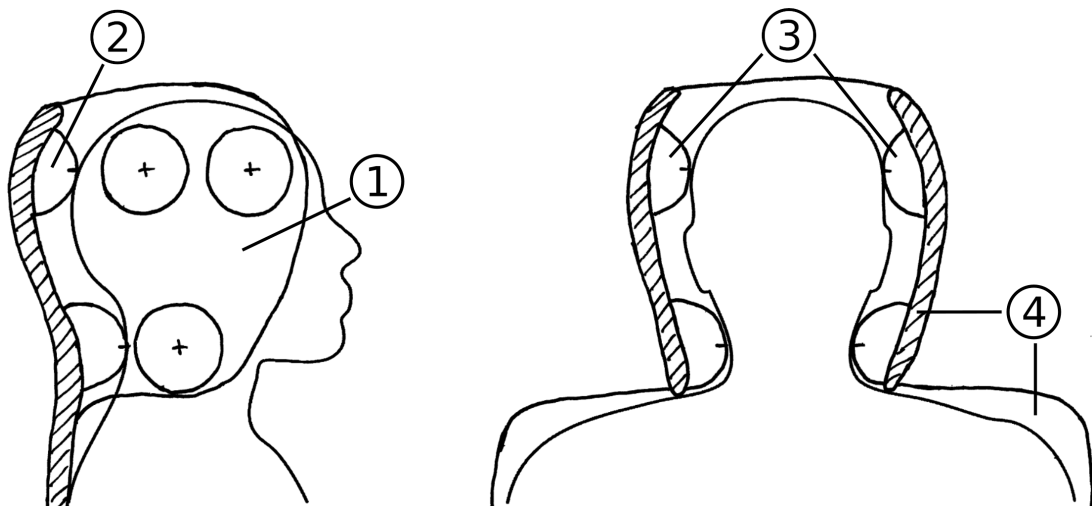


Figure 4-1: The chosen concept (see Table D-1; red line). Listed: The head and neck are enclosed for maximum fixation (1). Membrane actuators; inflatable balloons (2). The head and neck are clamped into place by the actuators (3). The immobilization device is rigidly connected to the treatment couch (4). There are three actuators on each side and two at the back of the head and neck. The face is uncovered for improved patient comfort.

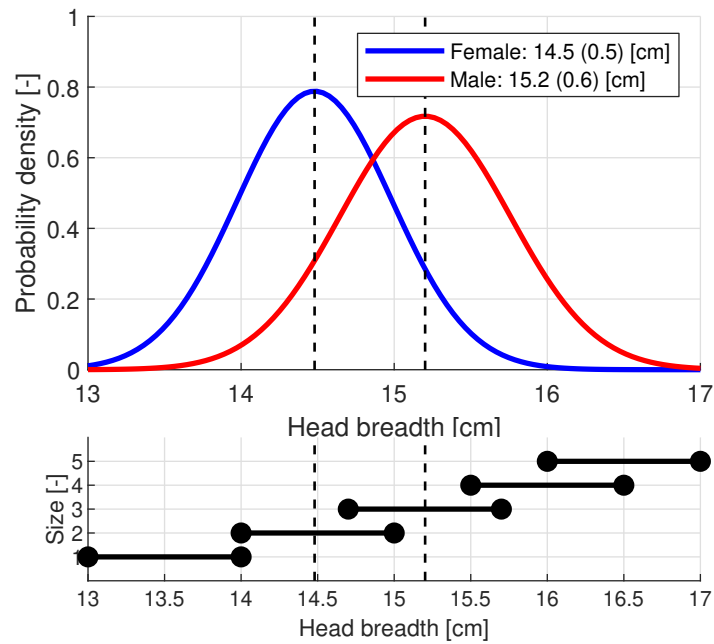


Figure 4-2: Top: male and female head breadth distribution [48]. The means are given by the dotted lines. Bottom: the different immobilization device sizes. Note that there is some overlap between sizes. This is because it is desired to have some sizes centered around the mean breadths for males and females. These sizes are sufficient to fit 99.7% of the patients (± 3 SD).

4-3 Attenuation of the Proton Beam

Suppose that the shell has a thickness of $h = 1$ cm and that the maximum rotational error is $\alpha = 5^\circ$. Then the amount of extra material the proton beam needs to penetrate due to the rotational error is given by:

$$\Delta h = h \left(\frac{1}{\cos \alpha} - 1 \right) = 0.038 \text{ mm.} \quad (4-1)$$

This is negligible compared to the magnitude of the translations. Therefore, a straight design is chosen (Fig. 4-3, left).

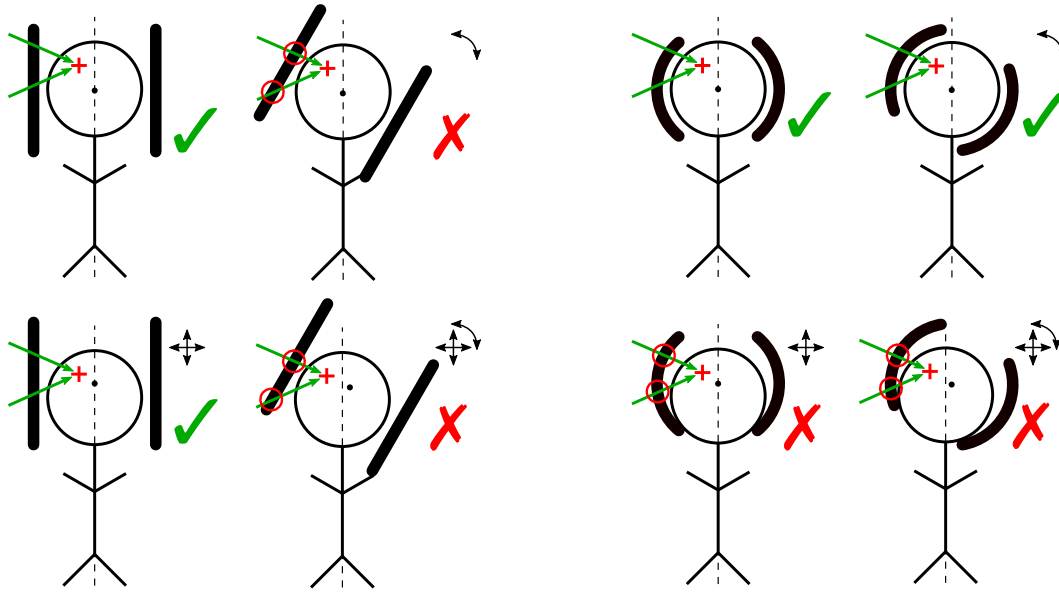


Figure 4-3: The effect of rotations and translations of the treatment couch on the proton beam attenuation. The immobilization device is fixed to the treatment couch. The clinical target volume (CTV) is denoted by the plus symbol and the arrows denote the two beam angles. As it turns out from Eq. (4-1) the effect of the rotations is negligible therefore the design to the left is chosen. Note that due to the shape of the head some curvature must be introduced to keep the material thickness to a minimum.

4-4 Design of the Air Channel

It is desired to have gradual density changes in the immobilization device. Because pneumatic actuators are chosen in Section 5-1, air channels are necessary. These channels are built into the shell. A comparison of four channel types is shown in Fig. 4-4. The wedge-shaped channel (number 3) is recommended; it is relatively easy to manufacture (if the shell is split into an inner and outer section of constant thickness) and more importantly, if done correctly the attenuation of the proton beam will not change.

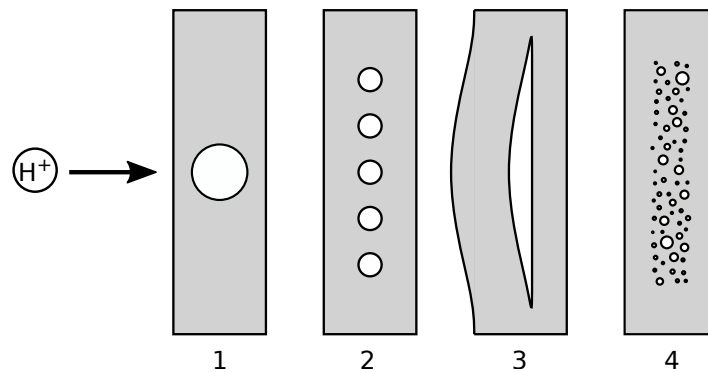


Figure 4-4: A comparison of four different air channel types. From left to right: a single large channel, multiple smaller channels, a wedge-shaped channel and a porous structure that lets air through. For the wedge-shaped channel extra material is added to the outside.

Membrane Actuators

A special type of actuators will be used, namely membrane actuators. These are rubber balloons that can be inflated. In this chapter the actuators are designed and placed in the immobilization device. A membrane model is also simulated and verified by measurements.

5-1 Actuator Type

In Appendix D a morphological chart was made to evaluate and compare design options. One of the design requirements is that the immobilization device must be compatible with MRI machines. This means that ferromagnetic materials are prohibited and other metals strongly discouraged. Electric actuation is therefore discarded as an option. This leaves hydraulic and pneumatic actuation as feasible alternatives.

Figure 5-1 shows the attenuation of the proton beam depending on its position and angle. A membrane type actuator is compared to a piston. For the membrane the attenuation is unaffected by its position or angle. In any case the materials that the proton beam has to penetrate are the same. This is also independent of the membrane deflection. The story is different for the piston where there is a lot less freedom in choosing the beam positions and angles. By extending the piston the beam can also be obstructed. The treatment planning process is important to consider since it affects the margins of the planning-CT (pCT). The membrane actuator gives the treatment planner the most freedom to optimize the treatment plan.

It should be noted that the above does not work for hydraulic actuation. If filled with an incompressible liquid (e.g. water) the effective thickness of the membrane would increase. Therefore pneumatic actuation of membrane actuators is chosen as the actuation type. The working principle is simple: the membrane is inflated to increase the force and deflated to decrease the force.

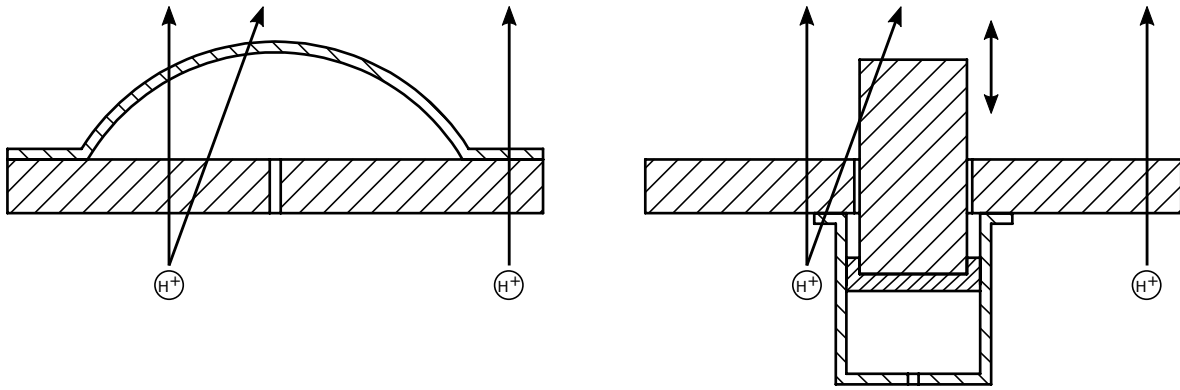


Figure 5-1: A cross-sectional view of a membrane and piston. The proton beam attenuation of the membrane is largely independent of the point of incidence and the angle of incidence of the proton beam. In contrast to the membrane the piston is sensitive to this.

5-2 Actuator Placement and Actuation Axis

The neck is capable of a large range of motion. The only motion that is restricted is the translation in cranial-caudal (CC) direction (along the y-axis in Fig. 5-2). As a result the head has five degrees of freedom (DOFs) (with respect to the body, which was assumed fixed).

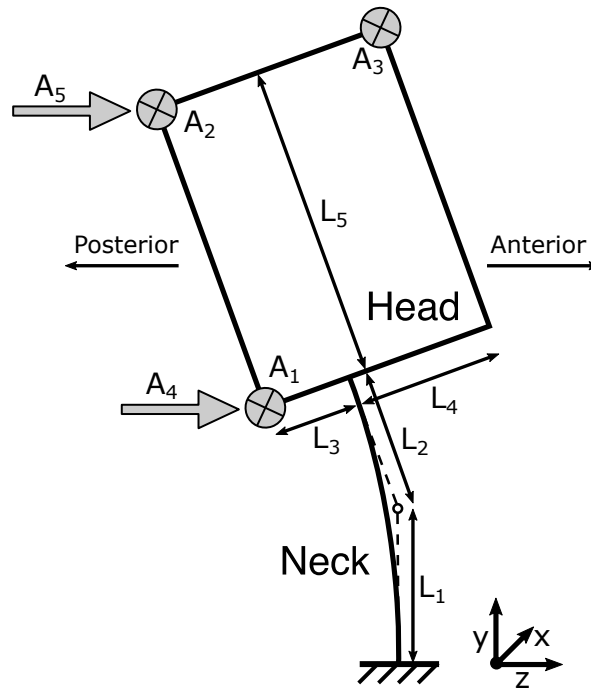


Figure 5-2: The placement of the actuators is shown for a simplified model of the head and neck. The effective rotation center is located at vertebra C4. Given dimensions are of a median male (height 1.74 m) [49]: $L_1 = 65$ mm, $L_2 = 59$ mm, $L_3 = 43$ mm, $L_4 = 57$ mm, $L_5 = 110$ mm. For the placement of the actuators the neck is approximated by a wire flexure.

The actuators are placed according to a constraint pattern design procedure, outlined by Su et al. [50]. This is a mathematical method of finding the locations and orientations of the

actuators. Using screw theory (Appendix C), the motions will be described by twists and the constraints by wrenches.

A motion is constrained when the reciprocal product of the twist (T) and wrench (W) (i.e. the power) is zero:

$$P = WT = m\omega + fv = 0. \quad (5-1)$$

The actuators are modeled as ideal five DOF wire flexures. A wire flexure only constrains the motion in axial direction. This modeling assumption follows from the following observations:

- The shear stiffness of the skin with respect to the skull is low.
- The shear stiffness of the membrane is relatively low; of the order 1 kN m^{-1} , assuming no volume change.

This leads to the constraints: $f_x m_x + f_y m_y + f_z m_z = 0$ and $f_x^2 + f_y^2 + f_z^2 \neq 0$. Now suppose that the only free motion of the head is the aforementioned translation in CC direction. The twist corresponding to this motion is

$$T = [0 \ 0 \ 0 \mid 0 \ 1 \ 0]^T. \quad (5-2)$$

Its reciprocal product with a general wrench $W = [m_x \ m_y \ m_z \mid f_x \ f_y \ f_z]$ is

$$WT = f_y = 0. \quad (5-3)$$

The general wrench in the complementary constraint space is then given by:

$$W = [m_x \ m_y \ m_z \mid f_x \ 0 \ f_z], \quad (5-4)$$

which has constraints: $f_x m_x + f_x m_z = 0$ and $f_x^2 + f_z^2 \neq 0$. Limiting the wrenches to work along a single axis, the eight wrenches listed in Table 5-1 can be constructed. The constraint space is denoted by:

$$\Pi_W = \begin{bmatrix} W_1 \\ W_2 \\ \vdots \\ W_8 \end{bmatrix}, \quad (5-5)$$

Any constraint in this space can be written as a linear combination of the basis wrenches. The rank of the constraint space is:

$$\text{rank}(\Pi_W) = 5. \quad (5-6)$$

This means that there are five independent wrenches that span this space. In other words, a minimum of five actuators is needed to constrain the head such that only a translation in the CC direction is possible. Since this motion was already constrained in the first place, the head will then be immobilized.

The following wrenches are chosen:

$$\Pi'_W = \begin{bmatrix} W_1 \\ W_2 \\ W_4 \\ W_5 \\ W_6 \end{bmatrix} = \begin{bmatrix} 0 & 0 & 0 & \mid & 1 & 0 & 0 \\ 0 & 0 & -1 & \mid & 1 & 0 & 0 \\ 0 & 1 & -1 & \mid & 1 & 0 & 0 \\ 0 & 0 & 0 & \mid & 0 & 0 & 1 \\ 1 & 0 & 0 & \mid & 0 & 0 & 1 \end{bmatrix} \quad (\text{full row rank}) \quad (5-7)$$

The constraint pattern design procedure only determines global actuator locations and orientations. In practice the actuator orientation also depends on the contact surface which it presses against. The sides of the head and neck are relatively flat thus it can be assumed that the placement of the side actuators does not change the actuation axis significantly. In that case the contact surface is parallel to the actuators. However, the back of the head and neck is curved. In that case the relative placement of the back actuators suddenly becomes important. Since the head is not fixed in the CC direction it is desired to minimize the parasitic forces in this direction. This is to prevent either stretching of the neck or a displacement of the body. The configuration of the back actuators is shown in Fig. 5-3. In equilibrium the resultant moment and force must be zero. This gives three equations that are solved iteratively:

$$\begin{aligned} \sum \vec{F} = 0 : \quad & F_1 \cos \theta_1 + F_2 \cos \theta_2 - F_g = 0 \quad (\text{AP direction}) \\ & F_1 \sin \theta_1 - F_2 \sin \theta_2 = 0 \quad (\text{CC direction}) \\ \sum \vec{M} = 0 : \quad & -L_1 F_1 \cos \theta_1 + L_2 F_2 \cos \theta_2 = 0 \end{aligned} \quad (5-8)$$

Using the same mesh as shown in Fig. 7-2, an equilibrium is found where both actuators are horizontally aligned. The corresponding values are $\theta_1 = 18.8^\circ$, $\theta_2 = 12.5^\circ$, $L_1 = 59.5 \text{ mm}$, $L_2 = 41.3 \text{ mm}$ and $F_1 = 17.8 \text{ N}$, $F_2 = 26.5 \text{ N}$.

As long as the head and neck have similar dimensions and weight, the parasitic forces in CC direction are close to zero.

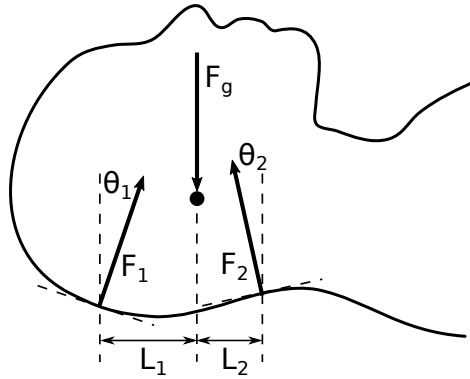


Figure 5-3: Actuator configuration of the back of the head and neck. The goal is to minimize parasitic forces in the CC direction due to forces applied in anterior-posterior (AP) direction.

The side actuator positions are chosen as such that they are comfortable and fit well to the shape of the head. The actuators must span the same constraint space as \prod'_W . Another consideration for the placement is the minimum stiffness of the actuators and their size. Roughly speaking, the further apart, the lower the required minimum stiffness. Also, they cannot be placed too close together due to the size constraints of the membranes. The appropriate working range is also influenced to a lesser extend. The actuators are placed as shown in Table 5-2.

Table 5-1: All the possible wrenches (along one of the three axes) that constrain the head along the left-right (LR) and AP direction. The variables x and y can be chosen freely.

| Wrench | Point |
|---------------------------------------|---------------------|
| $W_1 = [0 \ 0 \ 0 \mid 1 \ 0 \ 0]$ | $u = [x \ 0 \ 0]$ |
| $W_2 = [0 \ 0 \ -1 \mid 1 \ 0 \ 0]$ | $u = [x \ 1 \ 0]$ |
| $W_3 = [0 \ 1 \ 0 \mid 1 \ 0 \ 0]$ | $u = [x \ 0 \ 1]$ |
| $W_4 = [0 \ 1 \ -1 \mid 1 \ 0 \ 0]$ | $u = [x \ 1 \ 1]$ |
| $W_5 = [0 \ 0 \ 0 \mid 0 \ 0 \ 1]$ | $u = [0 \ 0 \ z]$ |
| $W_6 = [1 \ 0 \ 0 \mid 0 \ 0 \ 1]$ | $u = [0 \ 1 \ z]$ |
| $W_7 = [0 \ -1 \ 0 \mid 0 \ 0 \ 1]$ | $u = [1 \ 0 \ z]$ |
| $W_8 = [1 \ -1 \ 0 \mid 0 \ 0 \ 1]$ | $u = [1 \ 1 \ z]$ |

Table 5-2: The placement of the side actuators ($A_1 - A_3$) and back actuators (A_4 and A_5). The center of gravity is located at: $u = [0 \ 0.176 \ 0.027]$ [51]. A wrench is calculated as: $W = [u \times fr + mr \ fr]$, where $r \in \mathbb{R}^3$ is the actuation axis and $u \in \mathbb{R}^3$ is a point on this axis. f and m are the scalar force and moment, respectively. These wrenches span the same constraint space as $\prod W$.

| Actuator (Fig. 5-2) | Wrench (Table 5-1) | Direction and attachment point [m] | Description of the location |
|------------------------|-----------------------|---|--|
| A_1 | W_1 | $r = [1 \ 0 \ 0],$ $u = [-0.067 \ 0.100 \ -0.010]$ | Below the ears, against the side of the neck |
| A_2 | W_2 | $r = [1 \ 0 \ 0],$ $u = [-0.075 \ 0.222 \ -0.029]$ | Above the ears, against the side of the head |
| A_3 | W_4 | $r = [1 \ 0 \ 0],$ $u = [-0.067 \ 0.216 \ 0.071]$ | Against the temples |
| A_4 | W_5 | $r = [0 \ 0 \ 1],$ $u = [\ 0 \ 0.135 \ -0.065]$ | Against the nape of the neck |
| A_5 | W_6 | $r = [0 \ 0 \ 1],$ $u = [\ 0 \ 0.236 \ -0.065]$ | Against back of the head |

5-3 Actuator Module: Closed Pneumatic System

The stroke of the membrane cannot easily be measured. However, if a pneumatic system with a closed volume is used, then the membrane position is directly related to the piston position and the pressure in the membrane (Fig. 5-9). These two values are measured and thus the actuator stroke can be estimated. The same holds for the estimation of the force. Another advantage is that the system does not become unstable at the limit-point (see Section 5-5-4). This is because the pressure automatically drops when the volume increases.

Each actuator consists of a separate module. Such a module is shown in Fig. 5-4. It contains a piston that is used to inflate the membrane, a long flexible tube going from the piston to the membrane and the membrane itself. The piston is attached to a lead screw that is driven by a stepper motor. Assuming that the stepper motor does not skip any steps, the position of the piston is known with a resolution of 1.3 μm . A limit switch is installed near the motor to calibrate the position after a power loss and to prevent damage to the setup. The play on the lead nut is minimal because it is effectively preloaded by the pressure in the system. The flexible tube has a length of several meters and separates the metal and non-metal parts. Especially when using it in combination with the *magnetic* resonance imaging (MRI) machine it is desired to keep metals as far removed as possible. The air in the tube increases the total volume of the system which decreases the stiffness of the actuator. This problem is partly reduced by using small diameter tube. It can be entirely eliminated by filling the system with an incompressible liquid, e.g. water. The tubes can be made arbitrarily long as long as the volume of the water is equal to that of the tube. One has to be cautious about water entering the membrane as this will affect the proton beam. Also note that exceeding this amount effectively reduces the working range of the membrane.



Figure 5-4: A single actuator module. From left to right: an inflatable membrane, a long flexible tube (longer than shown), a pressure sensor, a piston, a lead screw, a limit switch and finally the stepper motor.

5-4 Design Requirements

In this section each of the requirements is defined and a constraint is formulated (if possible). These constraints are used in the optimization of the actuator parameters (Section 5-6).

5-4-1 Working Range

If the working range of the actuators is too small, one or both of the following things will happen:

- The displacement error is too large to be corrected.

Table 5-3: Maximum voluntary moments generated by the neck and the corresponding myoelectric signal levels [53]. The subconscious moments are estimated at 5% of the maximum voluntarily moments. Measured with vertebra C4 as the center of rotation. Standard deviations are shown in parenthesis.

| Mode | Voluntary moment [N m] | Myoelectric signal level [μV] | Subconscious moment [N m] |
|----------------------|------------------------|--|---------------------------|
| Relaxed ¹ | - | 12 (8) | - |
| Extension | 25.9 (13.4) | 52 (28) ² | 1.30 |
| Flexion | 10.4 (6.3) | 209 (77) | 0.52 |
| Lateral bending | 12.8 (7.3) | 122 (70) | 0.64 |
| Axial rotation | 8.5 (3.1) | 174 (80) | 0.43 |

¹ Measured in upright position as opposed to supine.

² Muscle activity was measured using surface electrodes that may inaccurately represent muscles in deeper tissue. This might explain the low myoelectric signal level for a large moment in extension.

- The patient cannot be sufficiently immobilized by the device due to morphological variations (specifically the breadth of the head).

The global corrections will be done by the treatment couch. The resulting 1D error from a treatment couch correction is approximately 1.2 mm for translations and 0.7° for rotations (Table B-1). The working range therefore mostly depends on the breadth of the head.

Ideally the working range is at least 39 mm (to fit 99.7% of the patients; see Fig. 4-2). This is not feasible as follows from the optimization (Section 5-6). So it is split up into five sections of 10 mm.

The working range is therefore constrained to $5 \text{ mm} \leq d \leq 15 \text{ mm}$.

5-4-2 Minimum Stiffness

Skeletal muscles are under voluntary control but they are subconsciously regulated [52]. It is therefore important to estimate the magnitude of the moments that are subconsciously generated by the neck in order to determine the needed fixation. Moroney et al. [53] measured the maximum voluntary moments in neck. These are listed in Table 5-3 along with the corresponding myoelectric signal levels. The signal level in the relaxed upright position is approximately 6–10% of that of the fully active modes (not including extension). This will be slightly lower for the supine position which is the default position during treatment. It is therefore assumed that the subconsciously generated moments are 5% of the maximum voluntarily moments. These values are shown in the last column of Table 5-3.

The resulting rotations of the head and neck should be below 0.3° and the translations below 0.6 mm (Table 3-1). These motions can be reduced by increasing the stiffness of the actuators. The minimum stiffness of the actuators is evaluated using the physical membrane model with no-slip boundary conditions (Section 5-5-3). The stiffness is evaluated for a constant preload force of 15 N for the side actuators and $F_g/2 = 21.4 \text{ N}$ for the back actuators. F_g is the gravitational force acting on the head (Section 6-3-3). Since a rotational error also results in

Table 5-4: An overview of the minimum actuator stiffnesses to ensure that the maximum errors are not exceeded. The maximum errors are $\theta_{\max} = 0.3^\circ$ for the rotations and $\delta_{\max} = 0.6$ mm for the translations. These are specified by the requirements (σ_{device} ; Table 3-1). The subconsciously generated are listed in Table 5-3. The dimensions are given by Fig. 5-2.

| Mode (subconscious moment [N m]) | Limiting error | Minimum actuator stiffness [kN m ⁻¹] |
|----------------------------------|---|--|
| Extension (1.30) ¹ | Translation: $\frac{1}{\theta_x} < \frac{L_1 + L_2}{\delta_z}$ | $\frac{M_{\text{extension}}}{L_1^2 + (L_1 + L_2)^2} \frac{L_1 + L_2}{\delta_z} = 11.4$ |
| Lateral bending (0.64) | Translation: $\frac{1}{\theta_z} < \frac{L_1 + L_2}{\delta_x}$ | $\frac{1}{2} \frac{M_{\text{lateral}}}{L_1^2 + 2(L_1 + L_2)^2} \frac{L_1 + L_2}{\delta_x} = 1.5$ |
| Axial rotation (0.43) | Rotation: $\frac{1}{\theta_y} > \frac{\max\{L_3, L_4\}}{\delta_x}$ | $\frac{1}{2} \frac{M_{\text{axial}}}{L_4^2 + 2L_3^2} \frac{1}{\theta_y} = 5.9$ |

¹ In flexion a smaller moment is generated (0.52 N m). The value for extension is used instead.

a translational error, only the worst of both is evaluated. The resulting minimum stiffnesses are shown in Table 5-4. It is assumed that only one of the listed modes is active at a time. Furthermore, it can be seen that the highest minimum stiffness is that of the actuators acting on the back of the head and neck. For lateral bending and axial rotation the actuators are placed on both sides, doubling the effective stiffness.

Configurations with more side actuators were considered. The total clamping force was kept constant and as a result the individual clamping force decreased. The stiffness therefore also decreased. No significant improvements were observed and due to size constraints these configurations were not chosen.

The stiffness at the preload force is therefore constrained to $k_{\text{side}} > 5.9$ kN m⁻¹ for the side actuators and $k_{\text{back}} > 11.4$ kN m⁻¹ for the back actuators. This must hold over the entire working range.

5-4-3 Dimensional Parameters

The thickness of the membrane influences the attenuation of the proton beam, the conformity to the head and the pressure that is needed to inflate it. For these reasons the thickness should be as small as possible. However, if the membrane is too thin it is prone to breakage during operation. If it is too thick, the neo-Hookean material model (Section 5-5-3) is no longer valid. Therefore $0.1 \text{ mm} \leq h_0 \leq 5 \text{ mm}$, where 0.25 mm is considered optimal.

The radius of the membrane is limited by the size of the human head. The maximum distance, from center to center, between actuators A_2 and A_3 is approximately 100 mm. Therefore the membrane radius at the side is constrained to $R_{\text{side}} \leq 40$ mm. On the back there is a bit more room, therefore $R_{\text{back}} \leq 60$ mm.

Table 5-5: The design constraints that follow from the actuator requirements.

| Requirement | Constrained variable | Units | Minimum value | Maximum value |
|--|--|-------------------|--------------------|---------------|
| Working range | Contact surface distance d | mm | 5 | 25 |
| Minimum stiffness | Actuator stiffness k | N m^{-1} | 7.75×10^3 | - |
| Dimensions | Membrane radius R | mm | 20 | 50 |
| | Source piston volume V_{piston} | mL | 0 | 300 |
| PT compatibility and practical feasibility | Membrane thickness h_0 | mm | 0.25 | 5 |

The volume of the piston partially determines the stiffness of the system and the maximum membrane deflection. It is constrained to $V_{\text{piston}} \leq 300$ mL to keep the setup compact.

5-4-4 Patient Comfort and Safety

The patient comfort is subjective, which means that a hard constraint cannot be formulated. Instead, the objective of the optimization (Section 5-6) will be to make the membranes as comfortable as possible for the patient. This means keeping the membrane thin and flexible such that they conform to the head. Also, the patient might hit the hard shell of the head support if the contact surface of the head is uneven or if it is not parallel to the membrane. A smaller membrane decreases the chances of this happening. Therefore, the radius of the membrane is minimized.

To ensure the safety of the patient (at the actuator level) a pressure relief valve should be mounted between the membrane and the piston. This valve opens when a threshold pressure is exceeded, sparing the patient.

5-5 Membrane Models

Due to the compressibility of air and the elasticity of the membrane the model can get quite complicated. One can choose between an approximate geometrical model or a physical model based on governing equations. The first model is useful to get qualitative insight into the behavior of the system while the second model is more accurate and is used to simulate and verify the actuators.

The membrane state is fully defined for a given actuator input ($0 \leq u \leq 1$, the position of the piston) and compression distance (x). This means that if these two values are known any of the other values can be calculated.

There are a few values that are calculated differently depending on the model that is used. These are:

- The deflection of the membrane: $\delta(u)$
- The contact radius of the membrane: $a(x, u)$
- The volume of the membrane: $V_{\text{mem}}(x, u)$

First the general equations are shown on which the models are built. Then there are two sections that treat the specifics of the simpler geometrical model and the more accurate physical model. See Fig. 6-4 for a visualization of the membrane and the used symbols.

5-5-1 General Framework

During free inflation the membrane forms a sphere with radius

$$R_0(u) = \frac{1}{2}R \left(\eta(u) + \frac{1}{\eta(u)} \right), \quad (5-9)$$

where R is the radius of the undeformed membrane and $\eta(u) = \delta(u)/R$ is a dimensionless parameter that relates the deflection $\delta(u)$ to the initial radius.

The membrane volume is:

$$V_{\text{mem}}(x, u) = V_{\text{free}}(u) - \int_0^x A(x', u) dx', \quad (5-10)$$

where $V_{\text{free}}(u)$ is the volume of the membrane during free inflation and $A(x, u) = \pi a(x, u)^2$ is the contact area of the membrane when compressed. The total volume of the system is then given by:

$$V(x, u) = V_{\text{mem}}(x, u) + \underbrace{(1-u) L_{\text{piston}} \pi r_{\text{piston}}^2}_{V_{\text{piston}}} + \underbrace{L_{\text{tube}} \pi r_{\text{tube}}^2}_{V_{\text{tube}}}, \quad (5-11)$$

Initial volume: V_{atm}

where L_{piston} and L_{tube} are the lengths of the piston and tube. r_{piston} and r_{tube} are their corresponding radii.

The compression of air is modeled by Boyle's law ($PV = \text{const.}$), which is valid for these working pressures and temperatures [54]. The pressure in the closed system is then given by:

$$P(x, u) = P_{\text{atm}} \left(\frac{V_{\text{atm}}}{V(x, u)} - 1 \right). \quad (5-12)$$

where $P_{\text{atm}} = 101.3 \text{ kPa}$ is the atmospheric pressure and V_{atm} is the initial volume.

The force generated by the membrane is:

$$F(x, u) = P(x, u)A(x, u). \quad (5-13)$$

Its stiffness is given by:

$$k(x, u) = \frac{\partial F}{\partial x} = \frac{\partial F}{\partial P} \frac{\partial P}{\partial x} + \frac{\partial F}{\partial A} \frac{\partial A}{\partial x} = \underbrace{\frac{P_{\text{atm}} V_{\text{atm}}}{V(x, u)^2} A(x, u)^2}_{\text{Pressure change}} + \underbrace{P(x, u) \frac{\partial A}{\partial x}}_{\text{Area change}}. \quad (5-14)$$

5-5-2 Geometrical Model: Approximation

An approximate model of the membrane is useful to gain insights in the mechanics that drive the force and stiffness. It makes it easier to compare different membrane shapes or configurations. This is further examined in Appendix E. Furthermore, the computational load of this model is much lower than that of the more accurate one.

The pressure during free inflation is approximated as [55]:

$$P_{\text{free}}(u) = \frac{4}{3} \frac{Eh_0}{R} \left(\frac{\eta(u)}{1 + \eta(u)^2} \right) \left(1 - \frac{1}{(1 + \eta(u)^2)^3} \right), \quad (5-15)$$

where E is the Young's modulus of the membrane and h_0 is its initial thickness. This pressure is used to find $V_{\text{free}}(u)$, the volume of the membrane during free inflation.

Up until the limit-point (Fig. 5-6), the mapping from the membrane volume to the pressure is bijective. For this application the function can therefore be regarded as invertible. The corresponding deflection is then found by a bounded optimization on this interval.

The membrane is approximated by a spherical segment (Fig. 6-4). The resulting approximations are:

$$a(x, u) = \sqrt{x(2R_0(u) - x)}, \quad (5-16)$$

and

$$V_{\text{mem}}(x, u) = \pi R_0(u) (\delta(u)^2 - x^2) - \frac{\pi}{3} (\delta(u)^3 - x^3). \quad (5-17)$$

5-5-3 Physical Model: Constitutive Equations

For the physical model the membrane is modeled as a uniform, axisymmetric solid as described by Long et al. [55]. It is clamped along the edge and subjected to a uniform pressure P on one side. Due to its symmetry only a cross-section needs to be evaluated. The cross-section of an inflated membrane is shown in Fig. 5-5. A cylindrical coordinate system is used to describe the position of the material points. The material coordinate ρ is varied from $0 \leq \rho \leq R$. Each material point at $(\rho, 0)$ in the undeformed configuration is transformed to a distinct point $(r(\rho), z(\rho))$ in the deformed configuration. The maximum deflection is at $(0, -\delta)$ with $\rho = 0$.

Two principal stretches are introduced:

$$\lambda_\xi = \frac{d\xi}{d\rho} \quad \text{and} \quad \lambda_\phi = \frac{r}{\rho}, \quad (5-18)$$

where ξ is the arc length from the maximum deflection point to the material point in the deformed configuration (as shown in Fig. 5-5a). These principal stretches are dimensionless coordinates that simplify the calculations.

It is simulated for different boundary conditions. These simulations may take a long time. The results are therefore precomputed and written to a disk. Later, when the actuator is evaluated, instead of repeating the simulations the precomputed values are interpolated. This also makes it possible to calculate values that follow from the simulation but cannot be chosen directly (the volume of the membrane for example).

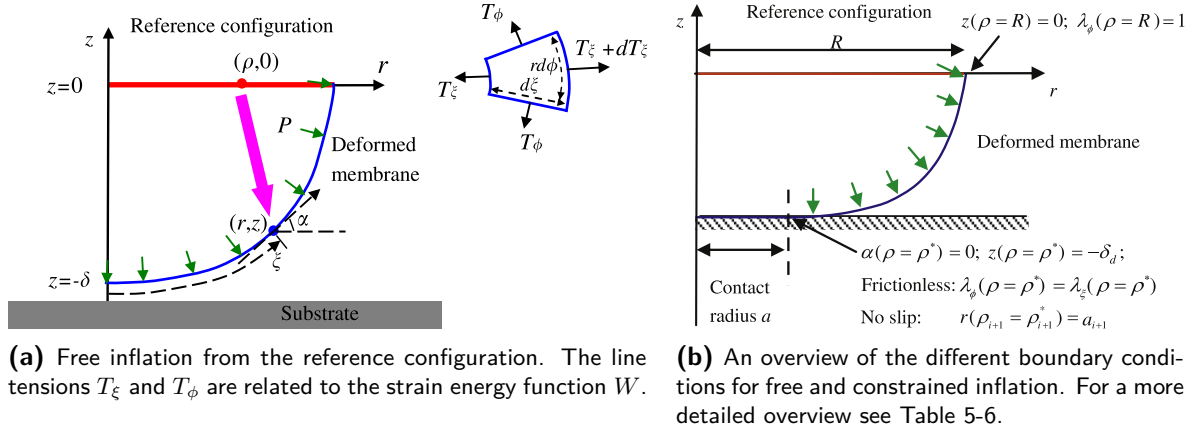


Figure 5-5: Deformation profiles of a cross-section of the membrane. Only half of the cross-section is simulated since the membrane is axisymmetric. From [55].

Constitutive Equations

The constitutive equations for large deformation membranes are [56]:

$$\frac{d\lambda_\xi}{d\rho} = \frac{\lambda_\xi (T_\phi - T_\xi) \cos \alpha - \lambda_\phi \frac{\partial T_\xi}{\partial \lambda_\phi} (\lambda_\xi \cos \alpha - \lambda_\phi)}{\rho \lambda_\phi \frac{\partial T_\xi}{\partial \lambda_\xi}},$$

$$\frac{d\alpha}{d\rho} = \frac{P \rho \lambda_\phi \lambda_\xi - \lambda_\xi T_\phi \sin \alpha}{\rho \lambda_\phi T_\xi}, \quad (5-19)$$

$$\frac{d\lambda_\phi}{d\rho} = \frac{\lambda_\xi \cos \alpha - \lambda_\phi}{\rho},$$

$$\frac{dz}{d\rho} = \lambda_\xi \sin \alpha.$$

A neo-Hookean material model is used, resulting in the strain energy density function

$$W = \frac{E}{6} \left(\lambda_\xi^2 + \lambda_\phi^2 + \frac{1}{(\lambda_\xi \lambda_\phi)^2} - 3 \right). \quad (5-20)$$

It assumes an incompressible material and a constant Young's modulus. The strain at a maximum deformation of $\delta_{\max} = R$ is:

$$\varepsilon_{\max} = \frac{L_1 - L_0}{L_0} = \frac{\pi}{2} - 1 = 57\%. \quad (5-21)$$

This is within the valid range for this model, which can handle strains of up to 100% [57].

The line tensions T_ξ and T_ϕ are related to this strain energy function W as:

$$T_\xi = \frac{h_0}{\lambda_\phi} \frac{\partial W}{\partial \lambda_\xi} = \frac{h_0 E}{3} \left(\frac{\lambda_\xi}{\lambda_\phi} - \frac{1}{\lambda_\xi^3 \lambda_\phi^3} \right), \quad (5-22)$$

$$T_\phi = \frac{h_0}{\lambda_\xi} \frac{\partial W}{\partial \lambda_\phi} = \frac{h_0 E}{3} \left(\frac{\lambda_\phi}{\lambda_\xi} - \frac{1}{\lambda_\xi^3 \lambda_\phi^3} \right). \quad (5-23)$$

Their partial derivatives are:

$$\frac{\partial T_\xi}{\partial \lambda_\xi} = \frac{h_0 E}{\lambda_\phi} \left(\frac{1}{\lambda_\xi^4 \lambda_\phi^2} + \frac{1}{3} \right), \quad (5-24)$$

$$\frac{\partial T_\xi}{\partial \lambda_\phi} = \frac{h_0 E}{\lambda_\phi^2} \left(\frac{1}{\lambda_\xi^3 \lambda_\phi^2} - \frac{1}{3} \lambda_\xi \right). \quad (5-25)$$

Boundary Conditions

Three types of inflation are considered. They only differ in the imposed boundary conditions. These types are:

- **Free inflation:** the inflation from the initial unloaded configuration up until the membrane hits a contact surface is called free inflation. The membrane is unobstructed and will form perfect sphere. The boundary conditions for free inflation are shown in Table 5-6. The governing equations contain five unknowns (including the pressure P), therefore five boundary conditions are specified.
- **Constrained inflation:** this type of inflation starts after the membrane has hit the contact surface. A circular contact area will form with a contact radius a . The point where the membrane releases the surface is at $(a, -\delta)$ with $\rho = \rho^*$. Depending on the contact surface and the membrane material, either frictionless or no-slip boundary conditions can be applied:
 - **Frictionless:** use these boundary conditions if there is no friction between the membrane and the contact surface. They assume that ρ^* is fixed and that $a = \lambda_\phi \rho^*$. Implementation wise it is easier to fix a and let $\rho^* = a/\lambda_\phi$. The boundary conditions are transformed accordingly with a change of variables. The new boundary conditions are shown in Table 5-6. Due to the change of variables the governing equations of Eq. (5-18) change to:

$$\frac{dx}{dr} = \frac{dx}{d\rho} \left(\frac{dr}{d\rho} \right)^{-1} = \frac{1}{\lambda_\xi \cos \alpha} \frac{dx}{d\rho} \quad (5-26)$$

where $x = [\lambda_\xi \alpha \lambda_\phi z]^T$ is the state of governing equations. It is unstable for pressures beyond the limit-pressure [58] (for limit point instability see Section 5-5-4).

- **No-slip** - Use these boundary conditions if there is no slipping between the membrane and the contact surface. This is the opposite of frictionless contact. They are shown in Table 5-6. In this case ρ^* is iteratively determined. An increase in material coordinate $\Delta \rho_i^*$ corresponds to an increase in contact radius $\Delta a_i = (\lambda_\xi)_i \Delta \rho_i^*$. The contact radius is updated with $r_{i+1}(\rho_{i+1}^*) = a_{i+1} = a_i + \Delta a_i$. This is also shown in Fig. 5-5b. The solution is then iteratively determined until the target contact radius is reached ($a_{i+1} > a_{\text{target}}$).

5-5-4 Limit-Point Instability

A membrane made of a neo-Hookean type material will become unstable for pressures exceeding the limit-pressure. This effect is shown in Fig. 5-6. If the pressure becomes too high,

Table 5-6: Boundary conditions for free inflation and constrained inflation, both frictionless and no-slip. These boundary conditions are specified by Long et al. [55].

| Free inflation | Constrained inflation | |
|--|--|--|
| | Frictionless ¹ | No-slip ² |
| $z(\rho = R) = 0$ | $z(r = R) = 0$ | $z(\rho = R) = 0$ |
| $\lambda_\phi(\rho = R) = 1$ | $\lambda_\phi(r = R) = 1$ | $\lambda_\phi(\rho = R) = 1$ |
| $\alpha(\rho = 0) = 0$ | $\alpha(r = a) = 0$ | $\alpha(\rho = \rho^*) = 0$ |
| $z(\rho = 0) = -\delta$ | $z(r = a) = -\delta$ | $z(\rho = \rho^*) = -\delta$ |
| $\lambda_\phi(\rho = 0) = \lambda_\xi(\rho = 0)$ | $\lambda_\phi(r = a) = \lambda_\xi(r = a)$ | $r(\rho_{i+1} = \rho_{i+1}^*) = a_{i+1}$ |

¹ After a change of variables described by Eq. (5-26).

² ρ^* is iteratively determined.

the membrane will expand uncontrollably. This limit-pressure is approximately:

$$P_{\text{limit}} = 0.63 \frac{Eh_0}{R}, \quad (5-27)$$

at $\delta/R = 1.26$. Hassager et al. [59] found a deflection of $\delta/R = 0.96$ for the limit-point. Although the source which is used to inflate the membranes is not a constant pressure source (and therefore cannot make the system unstable), it is still desired to avoid this limit-point. The deflections will be limited to below these values.

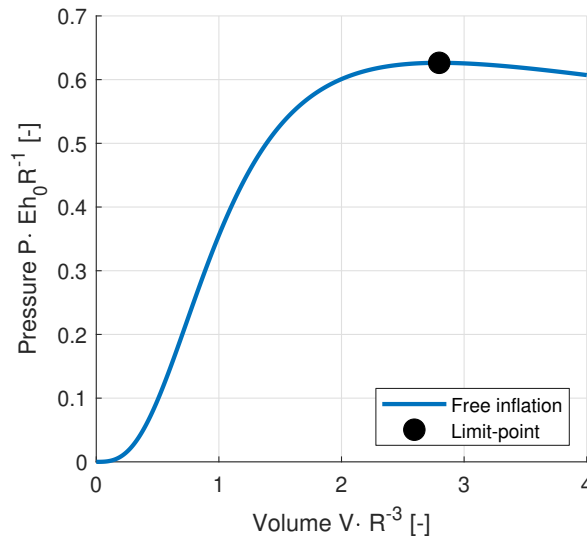


Figure 5-6: Free inflation of the membrane. The limit-point is unstable and a pressure beyond this value will cause the membrane to grow uncontrollably. Therefore the pressures in the system are kept below this value.

5-5-5 Temperature Sensitivity

The membranes will experience a temperature increase from heat conduction by the patient. The device is initially at room temperature $T_0 = 20^\circ\text{C}$, but after contact reaches an equilibrium temperature of $T_1 = 30^\circ\text{C}$ (approximate value for partial contact with the skin).

- **Young's modulus:** The elastic modulus of a polymer, perhaps counter-intuitively, increases with increasing temperature. The Helmholtz free energy is: $H = U - TS$, where U is the internal energy, T is the temperature and S is the entropy of the polymer. The Young's modulus is then given by:

$$E = \frac{\partial^2 H}{\partial \varepsilon^2} = \frac{\partial^2 U}{\partial \varepsilon^2} - T \frac{\partial^2 S}{\partial \varepsilon^2}, \quad (5-28)$$

where ε is the strain. The entropy decreases under elongation ($\partial S/\partial \varepsilon < 0$), but the rate of decrease decreases as well $\partial^2 S/\partial \varepsilon^2 < 0$. The result is that an increase in temperature will cause in an increase in stiffness.

The magnitude of the effect is given by [57], where it is stated that the elastic modulus is proportional to the absolute temperature:

$$\frac{E_1 - E_0}{E_0} = \frac{T_1 - T_0}{T_0} = 3.4\%. \quad (5-29)$$

This seems to agree with experiments [57, 60]. The result is a decreased working range and an increased clamping stiffness. This effect is small and will therefore be neglected.

- **System volume:** The air in the closed system is modeled by the ideal gas law:

$$PV = nRT, \quad (5-30)$$

where n is the number of moles of air and R is the gas constant.

Suppose that on average half of the air is located in the membrane (V_1) and the other half in the tube and piston (V_2). Starting at T_0 , after a while each volume is at a different temperature. V_1' is at T_1 and V_2' is still at T_0 . The change of volume as a result of the increased temperature (under constant pressure) is:

$$\frac{V' - V}{V} = \frac{T_1 - T_0}{2T_0} = 1.7\%, \quad (5-31)$$

where $V = V_1 + V_2$ is the old volume and $V' = V_1' + V_2'$ is the new volume. The result is an increased working range. In reality the effect would be less than that. A volumetric increase leads to a higher pressure due to the stiffness of the membrane. The resulting volume change is slightly less than calculated. This effect will also be neglected.

5-6 Parameter Optimization

In Section 5-4 several constraints on the actuator parameters (θ) were given. These parameters are listed in Table 5-8. The parameters are optimized to get the desired behavior of the membranes. The optimization is composed of two parts:

- **The objective function:** This determines the desired behavior of the actuators. It is desired to make the membrane not too thin to increase its lifetime and resistance to punctures ($h_0 = 0.25$ mm). The radius of the membranes must also not be too small since that would be uncomfortable for the patient.

- **The constraints:** The constraints must hold for both actuator types (side and back) and for any distance in the working range. The working range is discretized in 10 steps (d_1, d_2, \dots, d_{10}) and at each distance the system is evaluated. There is an equality constraint for the preload force ($F = F_{\text{preload}}$), an equality constraint for the distance ($\delta - x = d_j$) and an inequality constraint for the minimum stiffness ($k > k_{\text{min}}$).

The optimization problem is then given by:

$$\theta^* = \arg \min_{\theta, u, x} \left\| \frac{\theta_1}{0.25 \text{ mm}} - 1 \right\|_2^2 + \lambda \left(\left\| \frac{\theta_2}{R_{\text{side}}} \right\|_2^2 + \left\| \frac{\theta_3}{R_{\text{back}}} \right\|_2^2 \right)$$

$$\text{s.t. } \begin{cases} \underline{\theta} \leq \theta \leq \bar{\theta} \\ 0 \leq u \leq 1 \\ 1 - \frac{F(x_{ij}, u_{ij})}{F_{i, \text{preload}}} = 0 \\ 1 - \frac{\delta(u_{ij}) - x_{ij}}{d_j} = 0 \\ 1 - \frac{k(x_{ij}, u_{ij})}{k_{i, \text{min}}} \leq 0 \end{cases} \quad \left. \vphantom{\begin{cases} \underline{\theta} \leq \theta \leq \bar{\theta} \\ 0 \leq u \leq 1 \\ 1 - \frac{F(x_{ij}, u_{ij})}{F_{i, \text{preload}}} = 0 \\ 1 - \frac{\delta(u_{ij}) - x_{ij}}{d_j} = 0 \\ 1 - \frac{k(x_{ij}, u_{ij})}{k_{i, \text{min}}} \leq 0 \end{cases}} \right\} \text{For actuator type } i \text{ evaluated at distance } j \quad (5-32)$$

where $\lambda = 10^{-2}$ is a scaling factor. The input (u) and the compression (x) are optimized as auxiliary variables to make sure that the system is feasible at each state. The lower and upper bounds of a variable are denoted by $\underline{\cdot}$ and $\bar{\cdot}$ respectively. The solution is found with the MATLAB builtin function ‘fmincon’ (a constrained solver). It is set to use the ‘active set’ algorithm [61]. This algorithm is a modified version of sequential quadratic programming (SQP) that can take larger steps and potentially converge faster. The initial conditions are:

$$\theta = [0.25 \text{ mm } 30 \text{ mm } 40 \text{ mm } 100 \text{ mL } 100 \text{ mL}]^T, \quad (5-33)$$

$$u_i = 0.4 + \frac{1 - 0.4}{9} [0 \ 1 \ \dots \ 9] \quad \forall i \in \{1, 2\}, \quad (5-34)$$

$$x_{ij} = 0 \quad \forall i \in \{1, 2\} \text{ and } j \in \{1 \dots 10\}. \quad (5-35)$$

$$(5-36)$$

The optimized values are shown in Table 5-7. Figure 5-7 shows that the minimum stiffness requirements are satisfied.

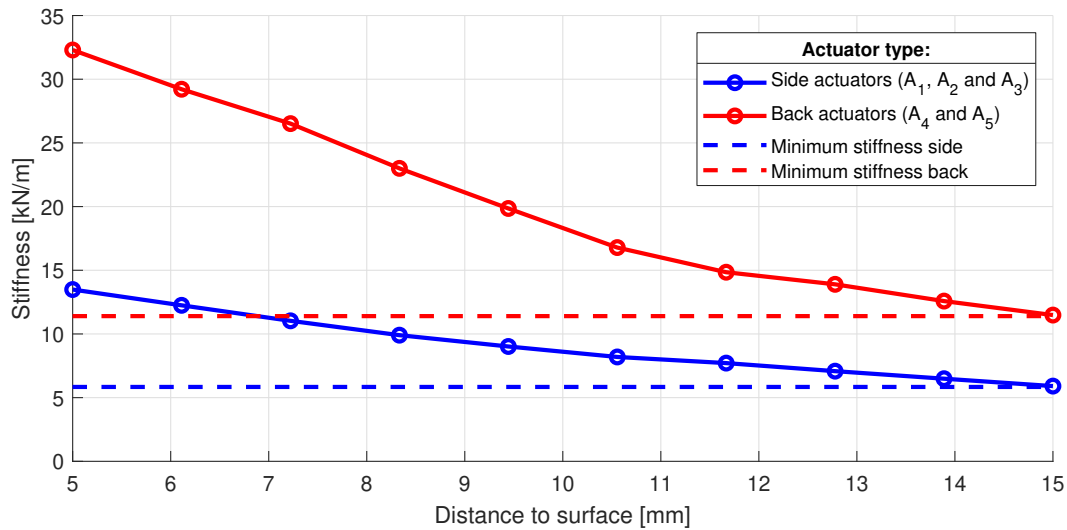


Figure 5-7: The actuator stiffness at the nominal clamping force. The minimum stiffness requirements are satisfied over the full working range.

Table 5-7: The lower and upper bounds of the actuator parameters that are to be optimized. The parameters are collected in $\theta = [h_0 \ R_{\text{side}} \ R_{\text{back}} \ V_{\text{side}} \ V_{\text{back}}]$. The optimal values are displayed in the last column. The Young's modulus of the membrane is assumed $E = 1.4 \text{ MPa}$ and the volume of the tubes is $V_{\text{tube}} = \text{mL}$ ($L_{\text{tube}} = 2 \text{ m}$).

| Parameter | Description | Actuator | Units | Min | Max | Optimal |
|-------------------|--------------------|---------------|-------|-----|-----|---------|
| h_0 | Membrane thickness | Side and back | mm | 0.1 | 5 | 0.23 |
| R_{side} | Membrane radius | Side | mm | 20 | 40 | 39.3 |
| R_{back} | Membrane radius | Back | mm | 20 | 60 | 58.4 |
| V_{side} | Piston volume | Side | mL | 0 | 300 | 73.1 |
| V_{back} | Piston volume | Back | mL | 0 | 300 | 144.5 |

5-7 Simulation and Verification

A side actuator was built and tested. Due to an error in an earlier actuator model the optimization produced slightly different results ($h_0 = 0.26 \text{ mm}$, $R_{\text{side}} = 25.0 \text{ mm}$ and $V_{\text{side}} = 21.8 \text{ mL}$). Therefore the tested actuator may deviate from the optimal one. This will not change the validity of the model nor invalidate the measured results.

5-7-1 Free vs. Constrained Inflation

When the membrane is inflated it deforms as shown in Fig. 5-8. Initially the membrane experiences free inflation ($P \cdot E h_0 R^{-1} < 0.30$) but as soon as the membrane makes contact with the surface there is a rapid increase in pressure. This can also be seen in Fig. 5-9, where the difference between free and constrained inflation is demonstrated. Both constrained inflation types are similar. The difference is that for frictionless boundary conditions the part of the membrane that touches the surface is free to expand, while for no-slip boundary conditions that part is assumed fixed. In both cases the pressure rises more rapidly as soon as the contact surface is reached.

This figure enables us to estimate the distance to the contact surface from the measured input and pressure. A similar plot can be made for the force instead of the pressure. This is demonstrated in Fig. 5-12b. It will be used to estimate and correct the clamping force on the head in Section 7-3-2.

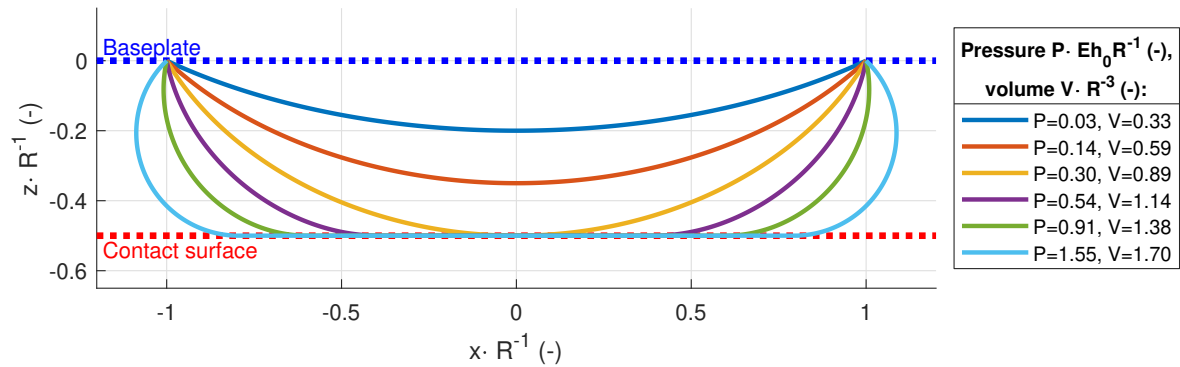


Figure 5-8: The deformation profile for constrained inflation with no-slip boundary conditions. All values are dimensionless which indicates that the deformation profile is similar for all spherical membranes.

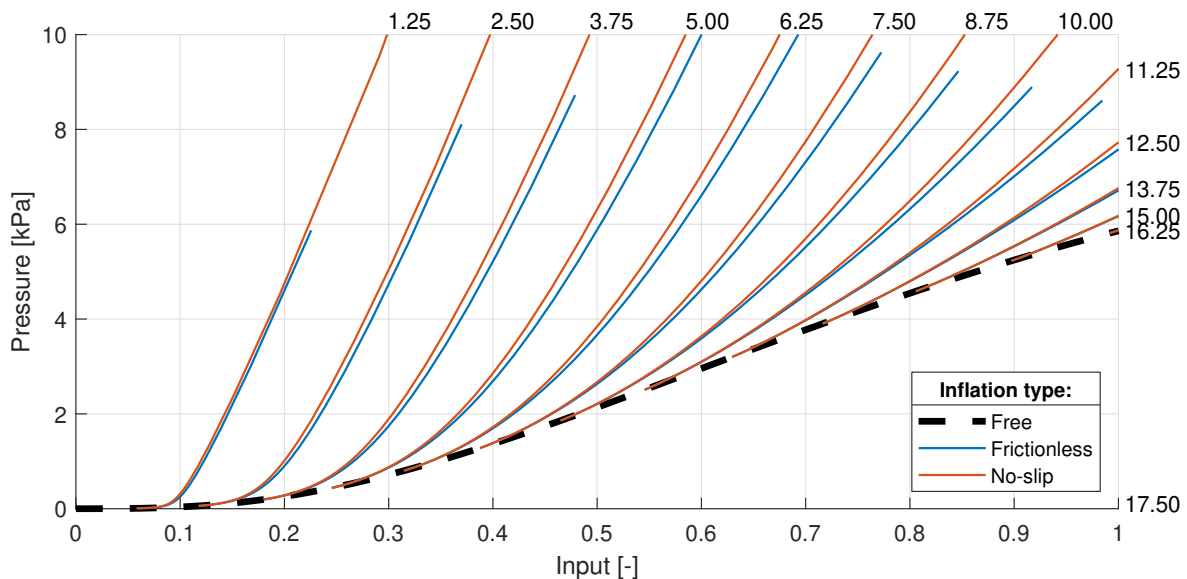


Figure 5-9: A comparison of free inflation and constrained inflation (frictionless and no-slip). The isolines denote a constant distance to the surface (in millimeters). For free inflation the pressure will follow the dotted line. This plot enables us to estimate the distance to the surface as well as (with a similar plot) the force that is generated by the actuator.

5-7-2 Measurement Setup and Model Verification

The test setup for validation of the membrane actuator model is shown in Fig. 5-10. Initially a force sensor was sandwiched between two parallel plates. The membrane would press against one end and with the winged nuts the distance could be changed (1 mm/rev). This was later replaced by a proper compression tester. This machine can measure the position and force

simultaneously. The setup with the compression tester is shown in Fig. 5-11. The tested actuator is identical.

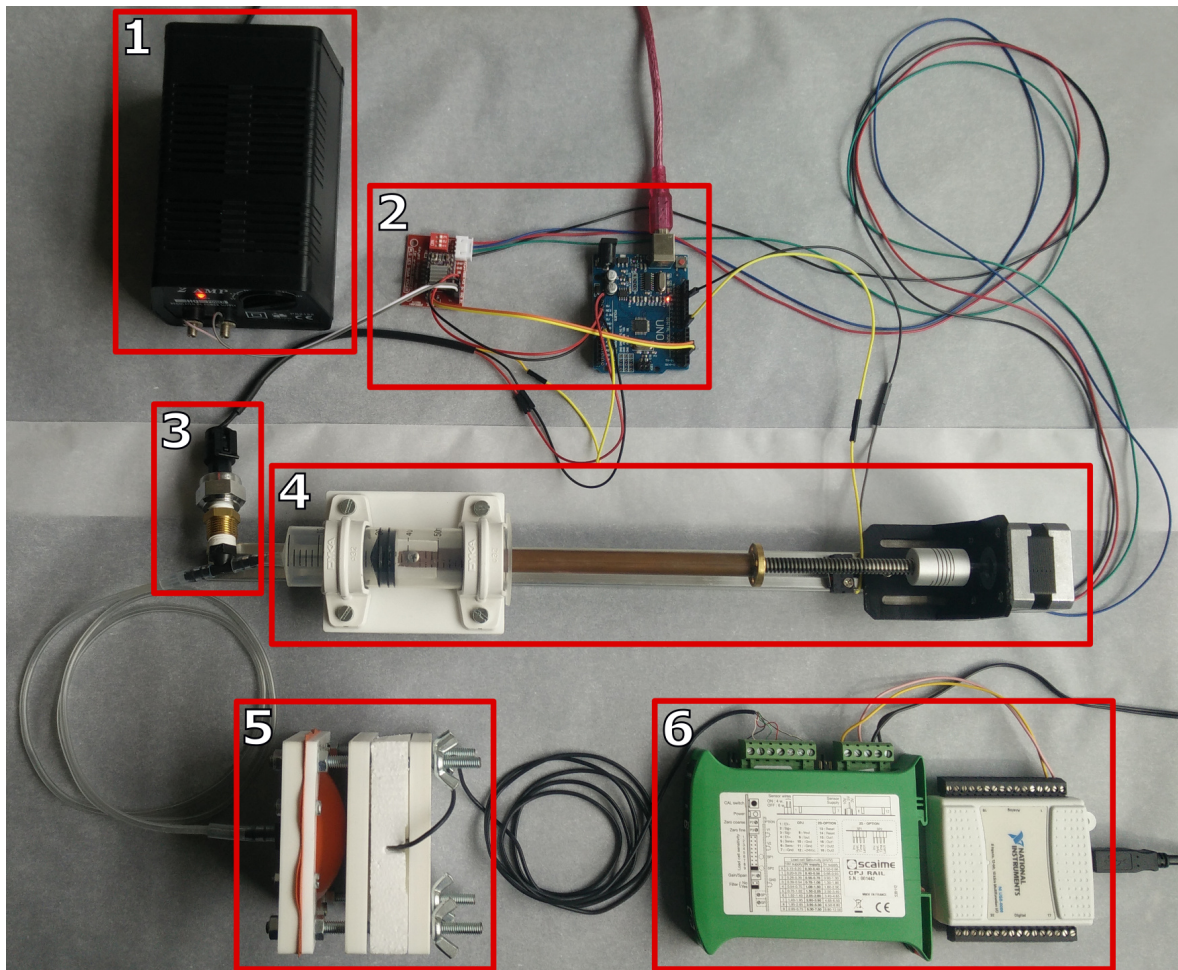
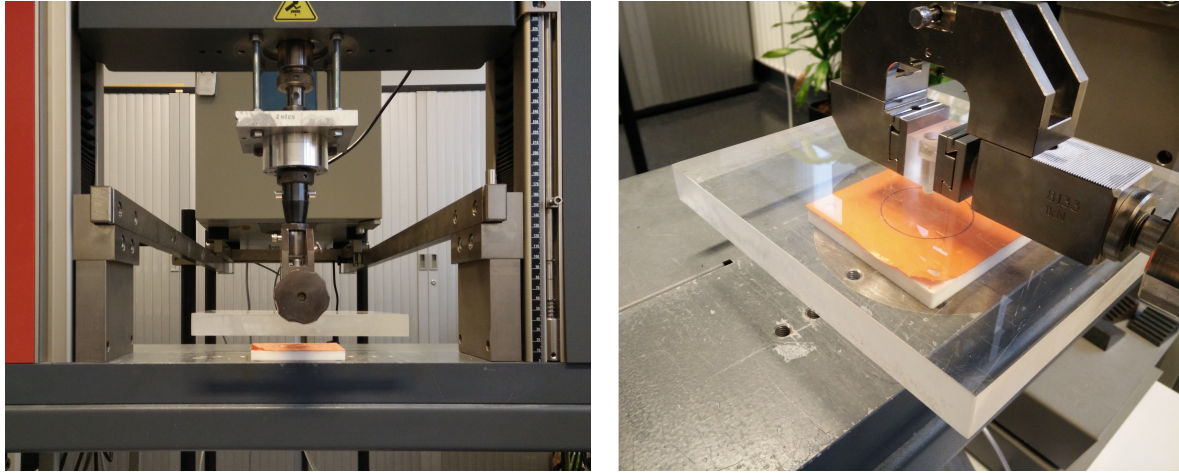


Figure 5-10: The test setup for validation of the membrane actuator model. The parts are: a 9V power supply (1), a micro-controller (ATmega328P) and stepper motor driver (2), a 1.2 MPa pressure sensor (3), the pneumatic source (4), the membrane pressing against a 100 N force sensor (5) and a signal amplifier together with an analog to digital converter (ADC) for the force sensor (6). In the end the force sensor was replaced by a universal testing machine (compression tester). With this machine the position could be controlled and the forces measured simultaneously.

Two tests were performed to verify the physical actuator model. In each of the tests the actuator input, the pressure, the force and the distance to the contact surface were recorded. These tests are:

- **Test 1:** The contact surface was set to a specific distance. Then the membrane was fully inflated and deflated. This was repeated for multiple distances. This data was used to fit the model parameters and to verify the model. This is shown in Fig. 5-12.
- **Test 2:** The compression tester was force limited to 20 N. It then slowly tried to compress the inflated membrane until this force was reached. This was done for different levels of inflation (different input u). This data was used to calculate the actuator stiffness at a load of 15 N. This is shown in Fig. 5-13.



(a) A front view of the machine.

(b) A close-up of the membrane (shown in orange). The size of the actuator is shown by the circle.

Figure 5-11: The test setup of the membrane using a compression tester. This machine can control the position and measure the forces simultaneously. The membrane presses against a plate which is connected to a force sensor. In both pictures the flexible tube going from the piston to the membrane is visible in the bottom.

Table 5-8: The parameters of the actuator module before and after fitting.

| Parameter | Symbol | Units | Initial value | Fitted value |
|---------------------------|-------------------|----------------|-----------------------|-----------------------|
| Young's modulus latex | E | MPa | 1.4 ¹ | 1.57 |
| Input offset | u_{off} | - | 0 | 0.05 |
| Tube volume (dead volume) | V_{tube} | m ³ | 1.26×10^{-5} | 1.25×10^{-5} |

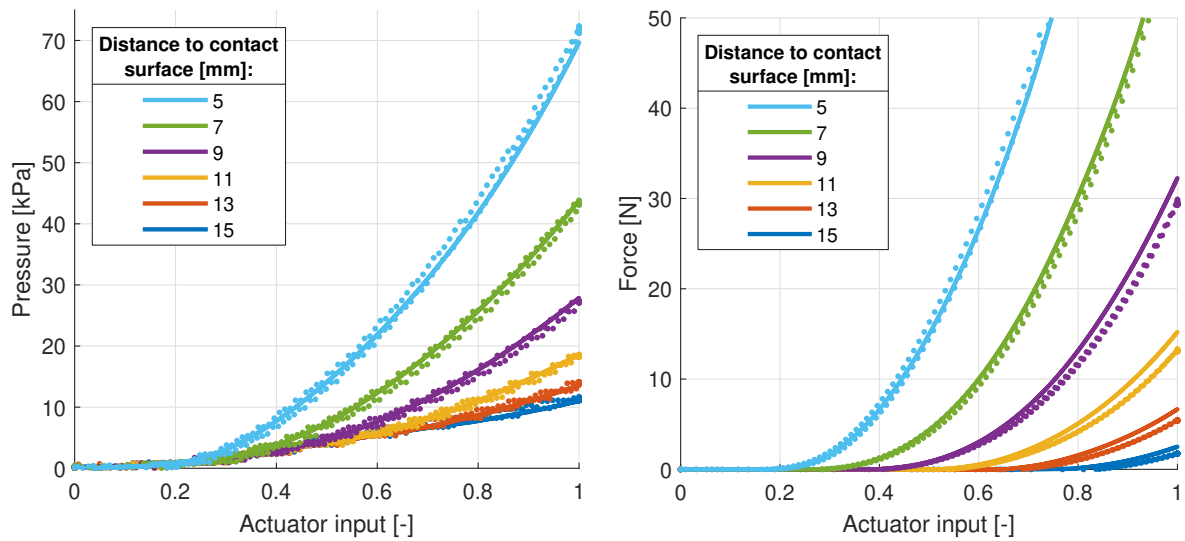
¹ Calculated from a simple tensile test. A strip of latex ($20 \times 50 \times 0.3$ mm) was clamped between two plates and loaded by a weight of 0.1 kg. This corresponds to values found in the literature [62]: 1.5–2.5 MPa.

It was noticed that the membrane did not fully return to the initial state. There was some permanent deformation. The membrane was therefore inflated a few times prior to the measurements to trigger this effect. In the model this was compensated for by adding an offset to the input (u_{off} , see Table 5-8). This way the membrane starts already slightly inflated.

The model with no-slip boundary conditions is fit to the measured data using a nonlinear least squares optimization method. The unknown parameters before and after fitting are shown in Table 5-8. The fitted model is compared to the measurements in Fig. 5-12. It can be seen that after fitting the model accurately predicts the pressure and the force.

5-7-3 Minimum Stiffness Verification

Similar to Fig. 5-7 the actuator stiffness at the nominal preload force is shown in Fig. 5-13. The largest change with respect to the optimal actuator is the reduced working range. The minimum stiffness requirement is still satisfied.



(a) The membrane pressure for a given input and contact surface distance. These measurements are used to fit the parameters listed in Table 5-8.

(b) The actuator force for a given input and contact surface distance. These measurements are used to verify the model. The force estimation becomes less accurate for larger distances.

Figure 5-12: The membrane pressure and force for a given input and contact surface distance. The continuous lines denote the model and the circles denote the measurements. It can be seen that the model is accurate. A slight hysteresis can be noticed in the measurements. During inflation the pressure sensor registers a slightly higher pressure than during deflation. This is because the sensor is mounted at the piston and the narrow tube restricts the air flow a little. Similarly, the force also lags behind.

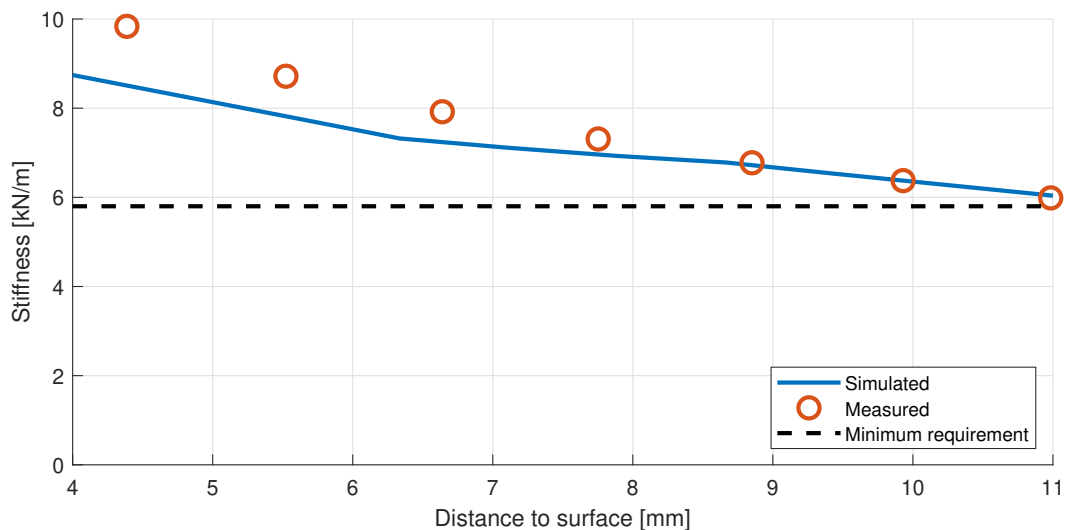


Figure 5-13: The stiffness of the side actuator at the nominal preload force (15 N). The minimum stiffness requirements are satisfied. For short distances the stiffness is underestimated by the model.

5-7-4 Distance Estimation of the Contact Surface

The data from Fig. 5-9 can be used to estimate the distance of the contact surface given the input and the pressure. This was tested on the measured data of test 1 and the results are shown in Fig. 5-14. During free inflation the combination of input and pressure is equal for any distance. The noise at low inputs is therefore reduced by ensuring that the membrane deflection can never be higher than that for free inflation.

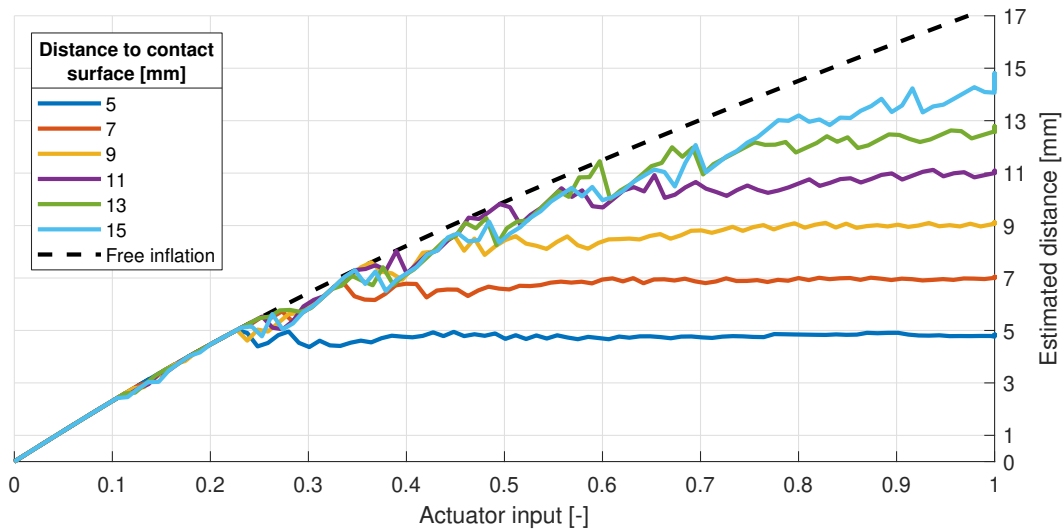


Figure 5-14: The distance to the contact surface can be estimated given the input and the measured pressure. The y-axis is shown on the right to better illustrate the estimation performance. For each specified distance the membrane is inflated fully. If the distance is small it can already be estimated for low input values. If the distance is large the estimation becomes a more unreliable. At the end of the working range the difference between free inflation and constrained inflation becomes small. The estimated distance must always lie below the dotted line (the maximum deflection for free inflation).

Anatomical Model

In this chapter an anatomical model of the head is built and simulated. It is simulated as a kinematic model consisting of five bodies. The generalized coordinates for which all the internal and external forces are in equilibrium will be called the static equilibrium. This position is calculated by the principle of minimum total potential energy.

6-1 Anatomy of the Head and Neck

Since every patient is different, the anatomical model will be based on a median male. In Table 6-1 several parameters are compiled that are used to model the head and neck.

6-1-1 Dominant Range of Motion

The head can rotate in each direction and translate in all but the CC direction. This gives the head five degrees of freedom (DOFs). Motion of the head in CC direction still occurs due to compression of the cervical discs during the day. While this effect is quite large with a mean total height change of 16.1 mm [64], it can simply be avoided by treating the patients during similar times of the day. Also note that this is the total height decrease and not only that of the neck. Since the forces on the neck are lower than those on the body (there is less weight pressing down on the vertebrae) the cervical compression will also likely be less.

In Table 6-2 the rotational range of motion is listed. The upper two joints contribute most to the the rotations in LR, and CC directions. In AP direction the contributions of the joints are approximately equal.

6-1-2 Neck Stiffness

McGill et al. [63] measured the passive stiffness of the neck, i.e. when the muscles are not activated. These measurements considered only rotations (see Table 6-3). The stiffness is linear for rotations $<30^\circ$ [63]. In Section 6-2-1 the neck will be modeled as a series connection of two prismatic joints and three revolute joints. In order to map the measured stiffness of the neck to the stiffness of these joints the equivalence relation of Fig. 6-1 is assumed.

Table 6-1: Model parameters for a median male.

| Parameter | Symbol | Units | Initial value | Source |
|-------------------------|--------|-----------------------|--------------------|--|
| Head mass | m | kg | 4.36 kg | Yoganandan et al. [51] (6.1 % of body weight) |
| Dimensions | | | | |
| Head breadth | b | mm | 152 | Poston [48] |
| T1 to C2 | L_1 | mm | 113.0 | Vasavada et al. [49] |
| C2 to C1 | L_2 | mm | 11.4 | Vasavada et al. [49] |
| C1 to center of gravity | L_3 | mm | 54.1 | Vasavada et al. [49] |
| T1 to measurement point | L_0 | mm | 230.4 | and Yoganandan et al. [51] McGill et al. [63] |
| Stiffnesses | | | | |
| Prismatic; LR direction | k_x | N m^{-1} | 62.44 | Lateral bending: Table 6-3 |
| Prismatic; AP direction | k_z | N m^{-1} | 51.86 | Average of extension and flexion: Table 6-3 |
| Revolute; LR direction | c_x | N m rad^{-1} | 0.69 | Average of extension and flexion: Table 6-3 |
| Revolute; CC direction | c_y | N m rad^{-1} | 1.63 | Axial rotation: Table 6-3 |
| Revolute; AP direction | c_z | N m rad^{-1} | 0.83 | Lateral bending: Table 6-3 |
| CC direction | k_y | N m^{-1} | 1.65×10^5 | Cervical compression: Eq. (6-3) |

Table 6-2: Range of motion of the neck (5th - 95th percentiles). Males and females combined.

| Rotation | Rotation axis | Range of motion [48] | Dominant joints [65] |
|-----------------------|---------------|--------------------------|---|
| Extension and flexion | LR | 65–103° and 40–78° resp. | Atlanto-occipital joint (skull - C1 ‘Atlas’), 15–20° |
| Axial rotation | CC | 74–104° | Atlanto-axial joint (C1 ‘Atlas’ - C2 ‘Axis’), approximately 50° |
| Lateral bending | AP | 34–67° | Equal contributions |

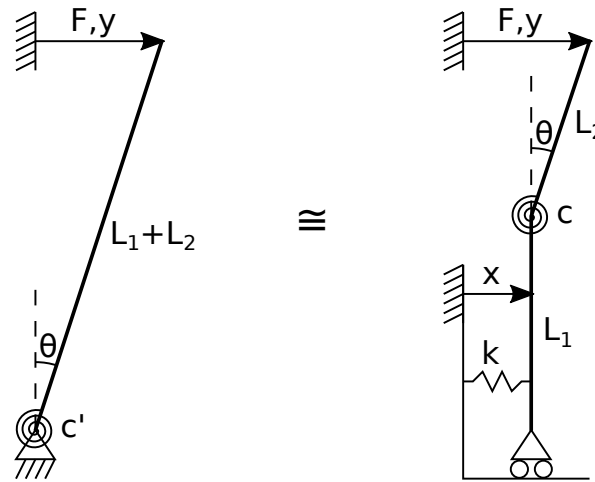


Figure 6-1: Left: the measurement setup with an applied force F resulting in a displacement y . The center of rotation is the cervical joint at T1 - C7 with $L_1 + L_2 = 230.4$ mm. Right: a setup that produces the same displacement for an identical force (assuming a small angle approximation). A prismatic joint has been added to reflect translations of the neck. The center of rotation depends on the location of the corresponding joints and is listed in Table 6-3.

The stiffness of the prismatic joints is then calculated by

$$k = \frac{1}{L_1(L_1 + L_2)} c', \quad (6-1)$$

where c' is the measured bending stiffness, L_1 is the distance from the old rotation center to the new rotation center and L_2 is the distance from the new rotation center to the point where the force is applied.

The stiffness of the revolute joints changes to

$$c = \frac{L_2}{L_1 + L_2} c'. \quad (6-2)$$

The values of the measured stiffness and the equivalent stiffness are listed in Table 6-3. The effect of the joint stiffnesses on the static equilibrium of the system are small compared to the actuator forces. Despite that, they still determine the relative joint positions. They are also used for the weighted regularization of the joint angles in Section 6-2-2.

The stiffness of individual motion segments is researched by Moroney et al. [66]. A motion segment is the joint between two vertebrae, including intermediate soft tissues. The average compression stiffness of an intact motion segment is $k_{\text{segment}} = 1.32 \times 10^6 \text{ N m}^{-1}$. Considering that there are eight motion segments in the neck (T1 - C7, C7 - C6, etc.) and that the motion segments are placed in series, the total compression stiffness of the neck is

$$k_y = \left(\sum_i^8 \frac{1}{k_i} \right)^{-1} = \frac{k_{\text{segment}}}{8} = 1.65 \times 10^5 \text{ N m}^{-1} \quad (6-3)$$

This is much higher than the stiffness in the other directions and therefore it will be assumed that there is no motion of the head in CC direction.

Table 6-3: Passive stiffness values of the neck for an average male. Values for the average female are shown in parenthesis [63]. The equivalent stiffness is calculated by Eqs. (6-1) and (6-2) using dimensions from Table 6-1.

| Mode | Measured stiff. [N m rad ⁻¹] | Equivalent stiffness (dimensions from Fig. 6-1) | | | |
|-----------------|---|---|---------------------------------------|------------|------------|
| | | Bending stiff. [N m rad ⁻¹] | Linear stiff. [N m ⁻¹] | L_1 [mm] | L_2 [mm] |
| Extension | 1.03 (0.37) | 0.48 | 36.06 | 124.4 | 106.0 |
| Flexion | 1.94 (1.48) | 0.89 | 67.67 | 124.4 | 106.0 |
| Lateral bending | 1.63 (0.88) | 1.06 | 87.49 | 80.6 | 149.8 |
| Axial rotation | - ¹ | 1.63 | - | - | - |

¹ Not measured; assumed equivalent to lateral bending.

Patients are often are a bit tense during the first few fractions. This has an effect on the perceived stiffness of the neck. But, as long as this stiffness does not change mid-fraction the alignment error should not be affected.

Table 6-4: A screw description of the joints in the kinematic chain. The dimensions are from [49]. The transform from joint C1-skull to the center of gravity is fixed.

| Joint | Type | Unit twist [m] | Motion |
|----------|-----------|--|----------------------------|
| C3-C2 | Prismatic | $\hat{T}_1 = [0 \ 0 \ 0 \ \ 1 \ 0 \ 0]^T$ | Translation in x-direction |
| C3-C2 | Prismatic | $\hat{T}_2 = [0 \ 0 \ 0 \ \ 0 \ 0 \ 1]^T$ | Translation in z-direction |
| C3-C2 | Revolute | $\hat{T}_3 = [0 \ 0 \ 1 \ \ 0.0796 \ 0 \ 0]^T$ | Lateral bending |
| C2-C1 | Revolute | $\hat{T}_4 = [0 \ 1 \ 0 \ \ -0.0139 \ 0 \ 0]^T$ | Axial rotation |
| C1-skull | Revolute | $\hat{T}_5 = [1 \ 0 \ 0 \ \ 0 \ 0.0148 \ -0.1235]^T$ | Extension and flexion |

6-2 Kinematics

Kinematics is the study of motion. The motion of the neck is provided by its seven vertebrae, C1-C7 (Fig. A-2). They give the neck five DOFs. The dominant joints listed in Table 6-2 serve as a basis for creating the kinematic model.

6-2-1 Forward Kinematics

The head and neck are modeled as a kinematic chain with two prismatic joints and three revolute joints (see Fig. 6-2). The kinematics of this series manipulator are described using screw theory (Appendix C). Each joint is described by a unit twist of the following form:

$$\underbrace{\hat{T} = \begin{bmatrix} 0 \\ \hat{v} \end{bmatrix}}_{\text{prismatic joint}} \quad \text{or} \quad \underbrace{\hat{T} = \begin{bmatrix} \hat{\omega} \\ u \times \hat{\omega} \end{bmatrix}}_{\text{revolute joint}}, \quad (6-4)$$

where $\hat{v} \in \mathbb{R}^3$ is the translation axis, $\hat{\omega} \in \mathbb{R}^3$ the rotation axis and $u \in \mathbb{R}^3$ is rotation point. The unit operator is denoted by $\hat{\cdot}$. The twists of the kinematic chain are listed in Table 6-4. The two prismatic joints and the first revolute joint together represent joint C3-C2. This joint is located approximately halfway through the neck. It reflects the translations and lateral bending as a sum of contributions of all the vertebrae in the neck. The other two revolute joints represent joint C2-C1 (axial rotation) and C1-skull (extension and flexion), respectively.

The homogenous transformation matrix of the end-effector can be calculated with Brockett's product of exponentials [67]:

$$H_n^0(q) = \prod_{i=1}^n H_i^{i-1}(q) = \left(\prod_{i=1}^n e^{\hat{T}_i^{0,(i-1)} q_i} \right) H_n^0(q_0) \quad (6-5)$$

where $q \in \mathbb{R}^5$ contains the generalized coordinates of the prismatic and revolute joints and H_i^j is the homogeneous transformation matrix from frame Ψ_i to frame Ψ_j . It can be partitioned as:

$$H_i^j = \begin{bmatrix} R_i^j & p_i^j \\ 0 & 1 \end{bmatrix}, \quad H_i^j \in \mathbb{R}^{4 \times 4} \quad (6-6)$$

where $R_i^j \in \mathbb{R}^{3 \times 3}$ is a rotation matrix and $p_i^j \in \mathbb{R}^3$ a position. All rotations and positions are with respect to the reference frame Ψ_0 , hence the superscript will be dropped.

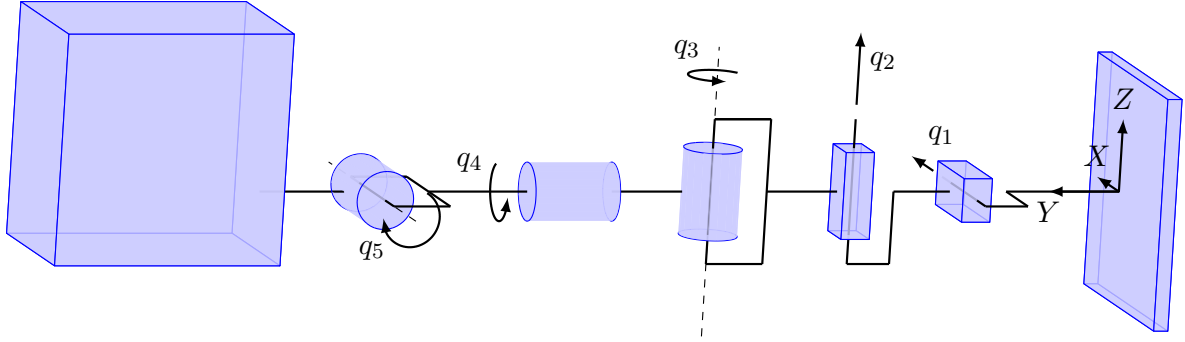


Figure 6-2: The series manipulator of the head and neck with the skull as end-effector. First there are two prismatic joints (q_1 and q_2) attached to the body (more specifically T1, the first of the thoracic vertebrae). Then there are three consecutive revolute joints ($q_3 - q_5$), with at the end the skull.

The twist exponential $e^{\hat{T}\theta}$ of the unit twist is given by

$$e^{\hat{T}\theta} = \begin{cases} \begin{bmatrix} I & \theta\hat{v} \\ 0 & 1 \end{bmatrix} & \text{if } \omega = 0 \text{ (pure translation),} \\ \begin{bmatrix} e^{\tilde{\omega}\theta} & (I - e^{\tilde{\omega}\theta})(\hat{\omega} \times v + \hat{\omega}^T v \hat{\omega}\theta) \\ 0 & 1 \end{bmatrix} & \text{otherwise,} \end{cases} \quad (6-7)$$

where $e^{\tilde{\omega}\theta} = I + \tilde{\omega} \sin \theta + \tilde{\omega}^2 (1 - \cos \theta)$ is Rodrigues' formula [67]. The operator $\tilde{\cdot}$ maps a vector to a skew symmetric matrix such that: $a \times b = \tilde{a}b$ $a, b \in \mathbb{R}^3$.

Pose: Orientation and Location

The combination of orientation and location of a body is called the pose. The pose of region-of-interest (ROI) i is denoted by:

$$y_i = \begin{bmatrix} \alpha \\ \beta \\ \gamma \\ x \\ y \\ z \end{bmatrix}, \quad (6-8)$$

where α , β and γ are the rotation angles and x , y and z are the coordinates.

With only three angles a rotation cannot be uniquely defined. In the literature several conventions are used when working with 3D-2D registration software. Therefore in this study Tait-Bryan angles will be used with rotation order 'XYZ'. These rotations are active (the object is rotated instead of the coordinate system) and extrinsic (the rotations are relative to a fixed reference frame).

Consider the following mapping from a homogeneous transformation matrix to its corresponding pose:

$$h : \mathbb{R}^{4 \times 4} \rightarrow \mathbb{R}^6. \quad (6-9)$$

It is invertible if all three rotation angles are less than 90° (i.e. avoiding gimbal lock).

The homogenous transformation matrix H can be partitioned as shown in Eq. (6-6) to extract the rotation matrix (R) and the location (p). The angles α , β and γ about the x-, y- and z-axis are then given by:

$$\alpha = \cos^{-1} \left(\frac{R_{33}}{\sqrt{1 - R_{13}^2}} \right), \quad \beta = \sin^{-1} (R_{13}) \quad \text{and} \quad \gamma = \cos^{-1} \left(\frac{R_{11}}{\sqrt{1 - R_{13}^2}} \right). \quad (6-10)$$

The coordinates are simply:

$$\begin{bmatrix} x \\ y \\ z \end{bmatrix} = p. \quad (6-11)$$

The pose is then the combination of orientation and location as shown in Eq. (6-8).

If the transformation matrix is calculated by Eq. (6-5), i.e. it depends on the generalized coordinates (q), then the following forward kinematics output function can be defined:

$$c_i(q) = h(H_i(q)) \quad (6-12)$$

where $y_i = c_i(q)$ is the pose of ROI i . It is the kinematic mapping from the joint-space to the end-effector work-space. The pose of each of the selected ROIs can be stacked and represented in a simplified way as:

$$y = \begin{bmatrix} y_1 \\ y_2 \\ \vdots \\ y_n \end{bmatrix} = \begin{bmatrix} c_1(q) \\ c_2(q) \\ \vdots \\ c_n(q) \end{bmatrix} = c(q). \quad (6-13)$$

This function will be used to calculate the output of the nonlinear state space in Eq. (7-4).

Geometric Jacobian and Hessian

In order to find the static equilibrium in Section 6-3 the derivative of the pose to each of the generalized coordinates is needed. This can be calculated numerically, but this is quite slow. Therefore, an analytical expression of the geometric Jacobian and the geometric Hessian are desired.

The geometric Jacobian maps the joint-space velocity to the end-effector velocity and is defined as:

$$J(q) = \begin{bmatrix} \frac{\partial y}{\partial q_1} & \frac{\partial y}{\partial q_2} & \cdots & \frac{\partial y}{\partial q_n} \end{bmatrix}, \quad (6-14)$$

where y is the pose of ROI i (the subscript is dropped for clarity).

The geometric Jacobian of the prismatic and revolute joints is calculated as [68]:

$$J_i(q) = \frac{\partial y}{\partial q_i} = \begin{cases} \begin{bmatrix} 0 \\ R_i \hat{v} \end{bmatrix}, & \text{if } \hat{T}_i \text{ is a prismatic joint} \\ \begin{bmatrix} R_i \hat{\omega} \\ R_i \hat{\omega} \times (p_e - p_i) \end{bmatrix}, & \text{if } \hat{T}_i \text{ is a revolute joint} \end{cases} \quad (6-15)$$

where p_e is the position of the end-effector.

The Hessian $H \in \mathbb{R}^{3 \times n \times n}$ is a third order tensor given by the second partial derivatives [68]:

$$H_{ij}(q) = \frac{\partial^2 y}{\partial q_i \partial q_j} = \begin{bmatrix} \tilde{a}_i & 0 \\ 0 & \tilde{a}_i \end{bmatrix} J_j(q) \quad i \leq j, \quad \text{with} \quad a_i = R_i \hat{\omega}. \quad (6-16)$$

Because of symmetry $H_{ij} = H_{ji}$.

Now suppose that the end-effector point does not lie on the origin of the end-effector frame, such that

$$p'_e = p_e + R_e p_o = p_e + b, \quad (6-17)$$

where p_o is the offset in the end-effector frame. Then the Jacobian changes to:

$$J'_i(q) = \begin{bmatrix} I & 0 \\ -\tilde{b} & I \end{bmatrix} J_i(q), \quad (6-18)$$

and the Hessian changes to:

$$H'_{ij}(q) = \begin{bmatrix} \tilde{a}_i & 0 \\ 0 & \tilde{a}_i \end{bmatrix} J'_j(q) \quad i \leq j. \quad (6-19)$$

This is useful for finding the derivatives of the actuators, forces and springs connected to the joints at an offset from the origin. It is used extensively in Section 6-3.

6-2-2 Inverse Kinematics

Inverse kinematics is the inverse of forward kinematics and is used to find the generalized coordinates that result in the desired reference pose of the end-effector. It is primarily used during the simulations to fit the head inside the immobilization device. It is also used to extend the model of the neck to simulate additional vertebrae.

Head alignment Inside the Immobilization Device

In practice the head will always be put inside the immobilization device. However, at the start of the simulation a body offset is generated (Section 7-5-1) that can potentially place the head outside the device. In that case the actuators are infeasible which leads to undefined behavior. Thus to prevent these problems, upon generation of a new configuration, the head will be placed inside the device using inverse kinematics.

A target location in the center of the device is selected as the reference pose (r). The location is weighted heavier than the orientation. It is more important that the head is in between the actuators than that the head is rotated a bit. The resulting optimization problem is written as:

$$q^* = \arg \min_q \|L^{-1}(r - c(q))\|_2^2 + \lambda \|Kq\|_2^2 \quad (6-20)$$

where L is a weighting matrix for the pose, λ is a scaling parameter and K is the stiffness matrix (Eq. (6-28)) which prevents unnatural solutions.

Neck Trunk

The lower vertebrae of the neck (C7 - C3) are not modeled in the standard kinematic model. However, if one of the ROIs that needs to be aligned is attached to one of these vertebrae they must be added to it. A solution is to first evaluate the standard model and then to attach the lower part of the neck to the upper part. One has to make sure that the orientation and location of both connecting parts is equal. This stitching is done through inverse kinematics similar to Eq. (6-20). The lower part of the neck consists of five spherical joints with a total of 15 generalized coordinates, one for each rotation. The reference is now joint C3 - C2 from the standard model and the weighting matrix is $K = I_{15}$ to reflect the equal importance of each rotation. In Fig. 6-3 a comparison is shown between the standard model and the patched model. Needless to say, the standard model is much faster to evaluate and less prone to errors.

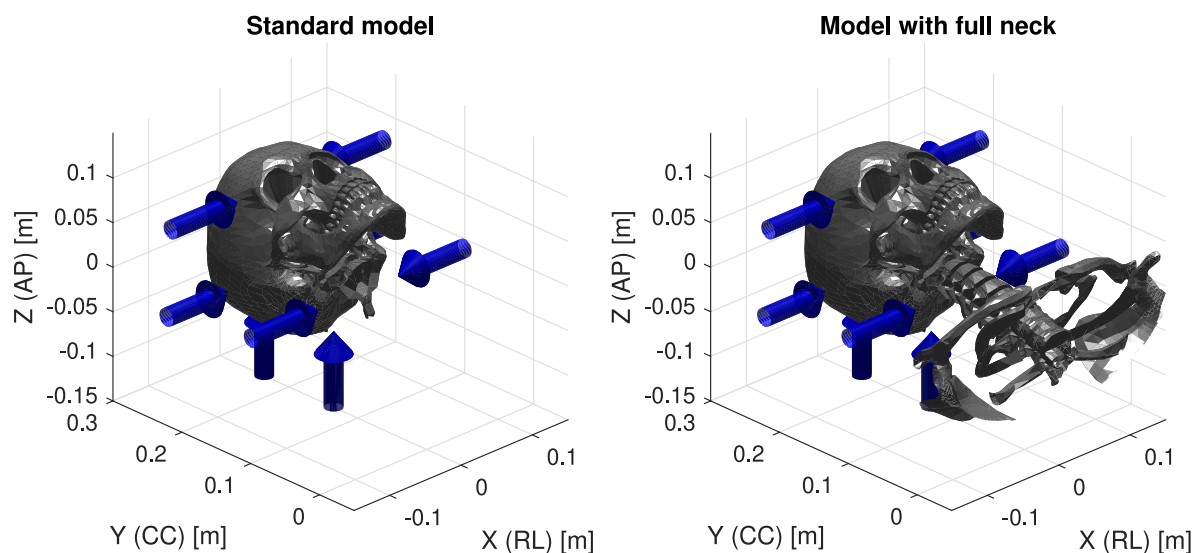


Figure 6-3: Left: the standard model that is used to calculate the pose of the ROIs. Right: the model where the remaining vertebrae of the neck are added through inverse kinematics. Although the body is not shown on the left, it can still be referenced as a ROI.

6-3 Static Equilibrium: Minimum Total Potential Energy Principle

The total potential energy of the system is [69]:

$$\Pi = U + V \quad (6-21)$$

where U is the stored elastic energy and V is the potential energy of the applied loads.

The system is in equilibrium when an infinitesimal variation from the stationary point results in no change in energy. With static is meant that the dynamics are neglected. The variation of energy is:

$$\delta\Pi = \delta(U + V) = \delta U + \delta V, \quad (6-22)$$

under the condition that the applied loads are conservative.

For this system with five joints, eight actuators and a gravitational force, the total variation of energy is:

$$\delta\Pi(q, u) = \sum_i^n \delta U_i^{\text{jnt}}(q) + \sum_i^m \delta U_i^{\text{act}}(q, u) + \delta V^{\text{gra}}(q). \quad (6-23)$$

Since the variation of energy must be zero for there to be an equilibrium, the optimization problem is simply given by:

$$q^* = q_{\text{eq}}(u) \triangleq \arg \min \|\delta\Pi(q, u)\|_2^2, \quad (6-24)$$

where $q_{\text{eq}}(u)$ is defined to be the solution to this optimization problem. The solution is found with the MATLAB builtin function ‘fminunc’ (an unconstrained solver). It is set to use the ‘Levenberg-Marquardt’ algorithm [61]. This algorithm switches intelligently between a gradient descent method and a Gauss-Newton method. Analytical expressions for

$$\frac{\partial^2\Pi(q, u)}{\partial q^2} \quad \text{and} \quad \frac{\partial^2\Pi(q, u)}{\partial q\partial u} \quad (6-25)$$

were calculated to speed up this optimization procedure.

In Eq. (7-4) a slightly modified version of $q_{\text{eq}}(u)$ is used to also account for a rotation of the treatment couch and an offset of the body. A rotation of the treatment couch changes the direction of the gravitational force:

$$f'_g = Rf_g, \quad (6-26)$$

where R is the rotation matrix of the couch. Since the rotational errors are small this effect is also small. An offset of the body changes the locations where the membranes make contact with the head. This effect is small but accounted for in the simulations (Section 7-5-1). It also affects the equilibrium position due to the stiffness of the neck. This effect is also small due to the low stiffness.

These effects are small and are therefore omitted in this section for clarity. However, they are implemented in the final MATLAB model which is used for the simulations. The contributions of the joints, actuators and gravitational force are detailed below.

6-3-1 Prismatic and Revolute Joints

The neck is modeled with two different joint types: prismatic joints and revolute joints. The potential energy of joint i is:

$$U_i^{\text{jnt}}(q) = \frac{1}{2}K_{ii}q_i^2 \quad (6-27)$$

where K is the linear stiffness matrix:

$$K = \begin{bmatrix} 87.49 & 0 & 0 & 0 & 0 \\ 0 & 51.87 & 0 & 0 & 0 \\ 0 & 0 & 1.06 & 0 & 0 \\ 0 & 0 & 0 & 1.63 & 0 \\ 0 & 0 & 0 & 0 & 0.68 \end{bmatrix}. \quad (6-28)$$

These values taken from Table 6-3 where the stiffnesses due to extension and flexion are averaged. The sum of the variation of energy then becomes:

$$\sum_i^n \delta U_i^{\text{jnt}}(q) = \sum_i^n \frac{\partial U_i^{\text{jnt}}}{\partial q} \delta q = q^T K \delta q. \quad (6-29)$$

6-3-2 Membrane Actuators: Nonlinear Springs

The membrane actuators are modeled in Section 5-5 and are implemented as nonlinear springs. The potential energy of a nonlinear spring is:

$$U = - \int_{x_0}^{x_1} F(x, u) dx \quad (6-30)$$

where $x(q, u)$ is the compression of the spring and $F(x, u)$ is the corresponding (scalar) force. The variation of energy of actuator i can thus be expressed as:

$$\delta U_i^{\text{act}}(q, u) = \frac{\partial U_i^{\text{act}}}{\partial x} \frac{\partial x}{\partial q} \delta q = -F_i(x, u) \frac{\partial x}{\partial q} \delta q. \quad (6-31)$$

From now on the subscript i will be dropped for clarity. For the following derivations the symbols from Fig. 6-4 are used.

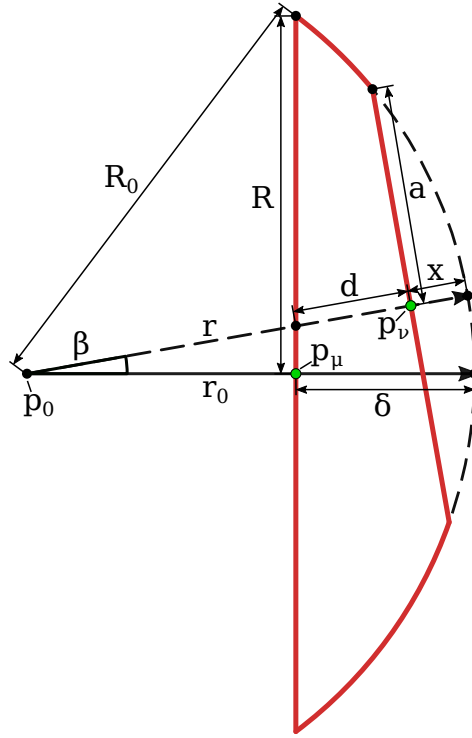


Figure 6-4: An approximation of the membrane profile under compression. The symbols are: R is the radius of the membrane in the undeformed configuration and r_0 is the initial actuation axis. $\delta(u)$ is the deflection of the membrane during free inflation. $R_0(u)$ is the radius of the corresponding sphere with $p_0 = p_\mu(q) + (\delta(u) - R_0(u))\hat{r}_0$ as the origin. $p_\mu(q)$ and $p_\nu(q)$ (shown in green) denote the attachment points of the virtual spring to joints μ and ν . These two points follow directly from the kinematic model. $d(q, u)$ is the distance between both surfaces (also called the stroke of the actuator) and $x(q, u)$ is the compression. $a(q, u)$ is the radius of the circular contact area. The contact area is always perpendicular to the actuation axis $r(q, u)$. This also shows that, as long as the compression is constant, the volume of the membrane is independent of the actuation angle ($\beta(q, u)$). This means that the actuator force is independent of the actuation angle.

The compression is given by:

$$x(q, u) = R_0(u) - \|p_\nu(q) - p_0(q, u)\|_2 = R_0(u) - \|p_\nu(q) - p_\mu(q) - (\delta(u) - R_0(u))\hat{r}_0\|_2, \quad (6-32)$$

where $p_\mu(q)$ and $p_\nu(q)$ are the locations where the spring is attached to joints μ and ν , respectively. $\delta(u)$ is the deflection of the membrane during free inflation and $R_0(u)$ is the corresponding principal curvature. \hat{r}_0 is the original axis of actuation and is only changed by a rotation of the treatment couch.

If the membrane is compressed along \hat{r}_0 (i.e. $p_\nu(q) - p_\mu(q) = \lambda \hat{r}_0$ for $\lambda \neq 0$) and if the actuator is in a feasible configuration (i.e. $\delta(u) \geq \|p_\nu(q) - p_\mu(q)\|_2$) this simplifies to:

$$x(q, u) = \delta(u) - \|p_\nu(q) - p_\mu(q)\|_2. \quad (6-33)$$

The derivative for the general case is:

$$\frac{\partial x}{\partial q} = - \frac{(p_\nu(q) - p_\mu(q) - (\delta(u) - R_0(u))\hat{r}_0)^T}{\|p_\nu(q) - p_\mu(q) - (\delta(u) - R_0(u))\hat{r}_0\|_2} [0_3 \ I_3] (J_\nu(q) - J_\mu(q)), \quad (6-34)$$

where $J_\mu(q)$ and $J_\nu(q)$ are the geometric Jacobians (Section 6-2-1) of joints μ and ν , respectively. The matrix $[0_3 \ I_3]$ is used to select only the derivatives of the location with respect to the generalized coordinates. In the simplified case the derivative is:

$$\frac{\partial x}{\partial q} = - \frac{p_j^T(q) - p_i^T(q)}{\|p_\nu(q) - p_\mu(q)\|_2} [0_3 \ I_3] (J_\nu(q) - J_\mu(q)). \quad (6-35)$$

6-3-3 Gravitational Force

The only constant force acting on the head is the gravitational force. The male head mass is $m = 4.36 \pm 0.59$ kg or approximately 6.1 % of the total body mass [51]. The center of mass of the head is located at a distance of $p_{\text{off}} = [0 \ 59.2 \ 18.0]^T$ [mm] (coordinate frame: Fig. 6-2) from the occipital condyle, which is located at the base of the skull close to C1 [49, 51].

The gravitational force acts on the skull in negative z-direction:

$$f_g = \begin{bmatrix} 0 \\ 0 \\ -mg \end{bmatrix}, \quad (6-36)$$

where $g = 9.81 \text{ ms}^{-2}$ is the gravitational acceleration constant. For the average male this results in a downward force of $F_g = 42.8$ N.

The potential energy of a constant force $f \in \mathbb{R}^3$ acting along a path $r \in \mathbb{R}^3$ is given by [70]:

$$V = - \int_{r_0}^r f \cdot dr = -f^T \int_{r_0}^r dr = -f^T (r - r_0), \quad (6-37)$$

where r_0 is the starting location. Substituting r with p^{skull} and f with the gravitational force f_g the variation of energy becomes:

$$\delta V^{\text{gra}}(q) = \frac{\partial V^{\text{gra}}}{\partial q} \delta q = -f_g^T \frac{\partial p^{\text{skull}}}{\partial q} \delta q = -f_g^T [0_3 \ I_3] J^{\text{skull}}(q) \delta q, \quad (6-38)$$

where $J^{\text{skull}}(q)$ is the geometric Jacobian of the skull.

Controller Design and Performance Evaluation

In order to minimize the alignment error and to adapt to the patient a controller must be implemented. This chapter explains how the controller is constructed and how the control input is generated. It also shows the results of the simulations.

7-1 Overview

The two primary functions of an adaptive immobilization device are alignment and fixation of the head and neck. The fixation will not be actively controlled during the fraction, though sudden motion of the patient can be detected (Section 5-7-4). The focus will lie on the automatic alignment of the patient at the beginning of the fraction.

The alignment correction is performed by a controller. This controller aligns the body by moving the treatment couch and aligns the head and neck with respect to the body using the membrane actuators located inside the immobilization device. An overview of this process is shown in Fig. 7-1. It is desired to keep the number of corrections as low as possible. Not only because of the extra dose given to the patient but also because the 3D-2D registration can take up to several minutes. According to Aitkenhead et al. [7] the number of patients that can be treated per day increases by up to 15 % if the setup time is decreased by 50 %. Given that the average setup takes five minutes, it is reasonable to expect an increase in throughput if the number of corrections is two or less.

Additional system components that are used in the setup, aside from the immobilization device, are:

- An adjustable six degree of freedom (DOF) treatment couch;
- And a stereoscopic X-ray measurement setup with 3D-2D registration software.

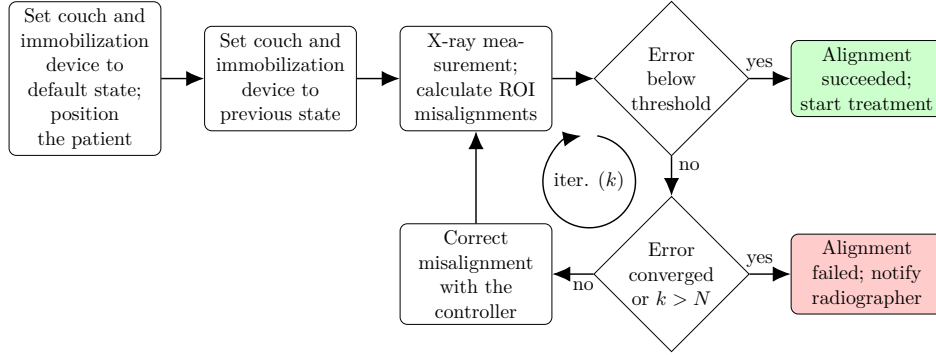


Figure 7-1: The alignment procedure at the start of each fraction. The number of corrections is to be kept as small as possible. Each iteration a single correction is performed. The current iteration is denoted by k and the maximum number of iterations by N .

7-2 Discrete State Space Model

The alignment process of the head and neck is captured in a discrete time state space model. Each step is just a single iteration. Each iteration a single correction is performed. The state is given by:

$$x = \begin{bmatrix} p^c \\ p^b \\ q \end{bmatrix} \in \mathbb{R}^{17}, \quad (7-1)$$

where $p^c \in \mathbb{R}^6$ is the pose of the treatment couch, $p^b \in \mathbb{R}^6$ is the offset pose of the body and $q \in \mathbb{R}^5$ is the generalized coordinate vector of the kinematic model of the head and neck.

The control input is partitioned as:

$$u = \begin{bmatrix} u^c \\ u^m \end{bmatrix} \in \mathbb{R}^{14}, \quad (7-2)$$

where $u^c \in \mathbb{R}^6$ is the input to the six DOF treatment couch and $u^m \in \mathbb{R}^8$ is the input to the membrane actuators inside the immobilization device.

Let the sum of two poses be defined as:

$$p = p_1 + p_2 \triangleq h \left(h^{-1}(p_1) \cdot h^{-1}(p_2) \right), \quad (7-3)$$

where $p = h(H)$ is the mapping from a homogeneous transformation matrix to the corresponding pose (Eq. (6-9)) and $H = h^{-1}(p)$ is its inverse. It is additive but not commutative.

The pose of each region-of-interest (ROI) is then described by the following nonlinear state

space model:

$$\begin{aligned}
 x_{k+1} = f(x_k, u_k) &= \begin{bmatrix} u_k^c \\ p_k^b \\ q_{\text{eq}}(u_k^c, p_k^b, u_k^m) \end{bmatrix}, \\
 y_k = g(x_k, u_k) &= \begin{bmatrix} p_k^c + p_k^b + c_1(q_k) \\ p_k^c + p_k^b + c_2(q_k) \\ \vdots \\ p_k^c + p_k^b + c_n(q_k) \end{bmatrix},
 \end{aligned} \tag{7-4}$$

where $q_{\text{eq}}(u^c, p^b, u^m)$ is a slightly modified version of $q_{\text{eq}}(u^m)$ (Eq. (6-24)). $c_i(q)$ is the kinematic output function as defined in Eq. (6-12) and n is the number of ROIs that is measured.

7-2-1 Linearization

The nonlinear state space system of Eq. (7-4) is linearized to:

$$\begin{aligned}
 \Delta x_{k+1} = \frac{\partial f}{\partial x} \Big|_{x_k, u_k} \Delta x_k + \frac{\partial f}{\partial u} \Big|_{x_k, u_k} \Delta u_k &= \underbrace{\begin{bmatrix} 0 & 0 & 0 \\ 0 & I_6 & 0 \\ 0 & \frac{\partial q_{\text{eq}}}{\partial p^b} & 0 \end{bmatrix}}_A \Delta x_k + \underbrace{\begin{bmatrix} I_6 & 0 \\ 0 & 0 \\ \frac{\partial q_{\text{eq}}}{\partial u^c} & \frac{\partial q_{\text{eq}}}{\partial u^m} \end{bmatrix}}_B \Delta u_k, \\
 \Delta y_k = \frac{\partial g}{\partial x} \Big|_{x_k, u_k} \Delta x_k + \frac{\partial g}{\partial u} \Big|_{x_k, u_k} \Delta u_k &\approx \underbrace{\begin{bmatrix} I_6 & I_6 & J_1 \\ I_6 & I_6 & J_2 \\ \vdots & \vdots & \vdots \\ I_6 & I_6 & J_n \end{bmatrix}}_C \Delta x_k, \\
 &\text{(for small rotations and translations)}
 \end{aligned} \tag{7-5}$$

where $J_i = \frac{\partial g_i}{\partial q}$ is the geometric Jacobian (Eq. (6-14)).

7-2-2 Observability

Two important concepts within control theory are the observability and controllability of a system. To determine the local observability of the nonlinear system, the observability of the linearized system is checked. The influence of the treatment couch rotation and the body offset is small (Section 6-3). So for the sake of analyzing the observability and controllability,

the linearized system is simplified to:

$$\Delta x_{k+1} = \underbrace{\begin{bmatrix} 0 & 0 & 0 \\ 0 & I_6 & 0 \\ 0 & 0 & 0 \end{bmatrix}}_A \Delta x_k + \underbrace{\begin{bmatrix} I_6 & 0 \\ 0 & 0 \\ 0 & \frac{\partial q_{\text{eq}}}{\partial u^m} \end{bmatrix}}_B \Delta u_k, \quad (7-6)$$

$$\Delta y_k = \underbrace{\begin{bmatrix} I_6 & I_6 & J_1 \\ I_6 & I_6 & J_2 \\ \vdots & \vdots & \vdots \\ I_6 & I_6 & J_n \end{bmatrix}}_C \Delta x_k. \quad (7-7)$$

The observability matrix is given by:

$$\mathcal{O} = \begin{bmatrix} C \\ CA \\ \vdots \\ CA^{16} \end{bmatrix}. \quad (7-8)$$

The linearized system is observable iff \mathcal{O} has full row rank. Since $A^m = A$ for $m > 0$ this is reduced to:

$$\text{rank}(\mathcal{O}) = \text{rank}\left(\begin{bmatrix} C \\ CA \end{bmatrix}\right) = \text{rank}\left(\begin{bmatrix} I_6 & I_6 & J_1 \\ \vdots & \vdots & \vdots \\ I_6 & I_6 & J_n \\ 0 & I_6 & 0 \\ \vdots & \vdots & \vdots \\ 0 & I_6 & 0 \end{bmatrix}\right). \quad (7-9)$$

The system is observable iff the number of ROIs is larger than 1 and:

$$\text{rank}\left(\begin{bmatrix} J_1 \\ \vdots \\ J_n \end{bmatrix}\right) = 5. \quad (7-10)$$

The neck is modeled as a kinematic chain, i.e. a series of joints. This means that the end-effector must be measured for the system to be observable, because that is the only body that is a function of the last generalized coordinate. In this case the end-effector is the skull and it can be shown that

$$\text{rank}(J^{\text{skull}}) = 5. \quad (7-11)$$

It is assumed that each ROI is measured correctly (i.e. all rotations and translations are known).

Incomplete Registration

If the system becomes unobservable because of bad or missing measurements, they must be repeated until the system becomes observable again. The discarded measurements are still useful as they can improve the current measurement.

The measured output is given by:

$$z_k = O_k y_k + w_k, \quad w_k \sim \mathcal{N}(0, R) \quad (7-12)$$

where y_k is the true output of the system and R is the covariance matrix of the measurement noise (Eq. (7-34)). The matrix O_k determines whether the ROI was registered successfully. For example:

$$O_k^1 = \underbrace{\begin{bmatrix} I_6 & 0 \\ 0 & I_6 \end{bmatrix}}_{\text{Full measurement}} \quad \text{and} \quad O_k^2 = \underbrace{\begin{bmatrix} I_6 & 0 \\ 0 & 0 \end{bmatrix}}_{\text{Missing ROI 2}}. \quad (7-13)$$

There can be two reasons for a bad or missing measurement:

- The 3D-2D registration algorithm failed to converge; it works with misalignments up to 15 mm [35].
- One or more of the registered ROIs is missing or badly visible on the X-ray image.

Multiple pose measurements can be combined into the following weighted linear least squares problem:

$$\underbrace{\begin{bmatrix} z_k^1 \\ z_k^2 \\ \vdots \\ z_k^n \end{bmatrix}}_{z'} = \underbrace{\begin{bmatrix} O_k^1 \\ O_k^2 \\ \vdots \\ O_k^n \end{bmatrix}}_{O'} y_k + \underbrace{\begin{bmatrix} w_k^1 \\ w_k^2 \\ \vdots \\ w_k^n \end{bmatrix}}_{\epsilon} \quad (7-14)$$

Due to missing measurements O' may not be full rank, meaning that y_k cannot be estimated correctly. The pose is therefore estimated in a robust way by [71]:

$$\hat{y}_k = V_1 \Sigma^{-1} U_1^T z', \quad \text{where} \quad O' = [U_1 \ U_2] \begin{bmatrix} \Sigma & 0 \\ 0 & 0 \end{bmatrix} \begin{bmatrix} V_1^T \\ V_2^T \end{bmatrix} \quad (\text{SVD}). \quad (7-15)$$

This is the minimum 2-norm solution to the linear least squares problem. When O' becomes full rank (i.e. each ROI is measured at least once) the solution becomes equal to that of the ordinary linear least squares. Since the measurements of the rotations are independent to those of the translations (i.e. they are separable) there is no need for a weighting matrix.

As a result, the observability matrix is full rank if the right ROIs are selected and if the measurements are successful. This means that Δx can be fully estimated and thus the system is locally observable.

7-2-3 Controllability

The controllability is a dual problem to the observability. Similarly to the observability matrix, the controllability matrix is given by:

$$K = [B \ AB \ \dots \ A^{16}B]. \quad (7-16)$$

The system is controllable iff K has full column rank:

$$\text{rank}(K) = \text{rank}([B \mid AB]) = \text{rank} \left(\begin{bmatrix} I_6 & 0 & \vdots & 0 & 0 \\ 0 & 0 & \vdots & 0 & 0 \\ 0 & \frac{\partial q_{\text{eq}}}{\partial u^{\text{m}}} & \vdots & 0 & 0 \end{bmatrix} \right). \quad (7-17)$$

Given that the actuators in the immobilization device are capable of five DOF actuation it makes sense that

$$\text{rank} \left(\frac{\partial q_{\text{eq}}}{\partial u^{\text{m}}} \right) = 5. \quad (7-18)$$

Furthermore, the body offset is not controllable since the body is assumed to be fixed to the treatment couch. This is one of the reasons why the six DOF treatment couch is used. The resulting rank is: $\text{rank}(K) = 6 + 5 = 11 < 17$ and thus the system is not controllable.

Controllability Normal Form

Since the system is not controllable, a coordinate transformation ($\Delta z = T\Delta x$) can be applied that separates the controllable from the uncontrollable modes. There exists an invertible transformation matrix T [72] that transforms Eq. (7-4) into:

$$\Delta z_{k+1} = \begin{bmatrix} A_{11} & A_{12} \\ 0 & A_{22} \end{bmatrix} \Delta z_k + \begin{bmatrix} B_1 \\ 0 \end{bmatrix} \Delta u_k \quad (7-19)$$

$$\Delta y_k = [C_1 \ C_2] \Delta z_k. \quad (7-20)$$

Now the pair (A_{11}, B_1) is controllable and the eigenvalues of A_{22} are the uncontrollable modes of (A, B) . This is called the controllability normal form. It is used to calculate the control inputs for the intrafraction controller.

7-3 Intrafraction Controller

At the beginning of the fraction the patient must be aligned with respect to the reference pose. This reference is determined during the treatment planning process. During each iteration (Fig. 7-1) the system is in equilibrium. The equilibrium only changes after a correction by the controller. This change is modeled as instantaneous (there are no dynamic effects). It is desired to align the patient in as few iterations as possible.

If the effects of the couch rotation and the body offset are neglected, then the optimal control input (u^*) is given by the following constrained optimization problem:

$$\begin{aligned} u^* = \arg \min_u & \quad \left\| L^{-1}(r - c(q_{\text{eq}}(u))) \right\|_2 \\ \text{s.t.} & \quad p^{\text{b}} + u^{\text{c}} = 0 \end{aligned} \quad (7-21)$$

where r is the reference pose, $c(q)$ is the output of the forward kinematics and $q_{\text{eq}}(u)$ is the equilibrium function. The treatment couch should cancel the offset of the body. The

weighting matrix L is primarily used to give a different weight to rotations and translations, but different weights can also be given to individual ROIs:

$$L = \begin{bmatrix} w_1 L_0 & 0 & \cdots & 0 \\ 0 & w_2 L_0 & \cdots & 0 \\ \vdots & \vdots & \ddots & \vdots \\ 0 & 0 & \cdots & w_n L_0 \end{bmatrix} \quad \text{with} \quad L_0 = \underbrace{\begin{bmatrix} (0.4^\circ)^2 I_3 & 0 \\ 0 & (0.7 \text{ mm})^2 I_3 \end{bmatrix}}_{\text{See requirements: Table 3-1}} \quad (7-22)$$

The weights w_i determine the relative importance of the individual ROIs. Larger ROIs or ones close to the tumor should get higher weights than others. In this study all ROIs are given equal weights.

This control input is only optimal if the model is exactly known. Unfortunately, every patient is different. In order to cope with model uncertainties, a gradient based output controller is designed. This means that it uses the linearized model to perform corrections based on the alignment error. First an unconstrained controller is designed and then a more practical constrained controller. The second controller will be used to simulate the system.

7-3-1 Unconstrained Controller

Equation (7-5) is written compactly as:

$$\begin{aligned} \Delta x_{k+1} &= A_k \Delta x_k + B_k \Delta u_k \\ \Delta y_k &= C_k \Delta x_k + D_k \Delta u_k \end{aligned} \quad (7-23)$$

where the system is linearized at each iteration (k).

Suppose that there is a control input u_{k+1} such that the tracking error goes to zero ($r - y(x_k, u_{k+1}) \rightarrow 0$) and the system is stationary ($\Delta x_{k+1} = \Delta x_k$). Then the control input is given by $u_{k+1} = u_k + \Delta u_{k+1}$ with:

$$\Delta u_{k+1} = \arg \min_{\Delta u} \left\| L^{-1} \left(\underbrace{r - y_k}_{\text{Tracking error}} - \underbrace{M_k \Delta u}_{\text{Correction}} \right) \right\|_2^2 \quad (7-24)$$

where $M_k = C_k(I - A_k)^{-1}B_k + D_k$ (with $\Delta y_k = M_k \Delta u_k$). This only holds when $(I - A_k)$ is invertible. This is not the case as can be seen from Eq. (7-6). The controllable modes correspond to the treatment couch and the actuators in the immobilization device. In Eq. (7-19) the controllable subsystem is therefore calculated resulting in:

$$M_k = \left(C_1(I - A_{11})^{-1}B_1 + D \right), \quad (7-25)$$

where $I - A_{11}$ is invertible this time.

M_k has three singular values that are zero. This corresponds to the two sets of opposing actuators in the immobilization device, three on each side. With this setup it is therefore possible to change the clamping force on the head without changing its position.

The solution to the optimization problem is then given by:

$$\Delta u_{k+1} = V_1 \Sigma^{-1} U_1^T L^{-1} (r - y_k), \quad \text{where} \quad L^{-1} M_k = [U_1 \ U_2] \begin{bmatrix} \Sigma & 0 \\ 0 & 0 \end{bmatrix} \begin{bmatrix} V_1^T \\ V_2^T \end{bmatrix} \quad (\text{SVD}), \quad (7-26)$$

This is the minimum 2-norm solution to the weighted linear least squares problem because M_k is singular. The solution is the minimum change in input that is needed to align the patient.

7-3-2 Constrained Controller: Force Correction

Previously the controller was not constrained. However, there are some physical constraints on the actuators, as well as some safety constraints. These are the minimum and maximum stroke of the pneumatic pistons ($0 \leq u^m \leq 1$) and the minimum clamping force on the head to maintain the appropriate stiffness ($F_k \geq F_{\min} = 15 \text{ N}$, Section 5-4-2). Only the clamping force of the side actuators is corrected. The objective is extended to also minimize the clamping force while simultaneously trying to maintain a set minimum force. These objectives and constraints are summarized in Table 7-1.

The force of the actuators (Eq. (5-13)) depends on the input to the actuators and the pose of the head. The change in clamping force due to a change in input is due to the following effects:

- An increase of the control input means an increase in pressure. Provided that the contact surface (in this case the head) remains stationary, the force increases.
- An increase in force means that the equilibrium position will change. The result is a lower force.

These two effects combined show how the control input changes the clamping force. This is represented by $\Delta F_k = N_k \Delta u_k$ where:

$$N_k = \frac{\partial F(q, u)}{\partial q} \frac{\partial q_{\text{eq}}(u)}{\partial u} + \frac{\partial F(q, u)}{\partial u}. \quad (7-27)$$

It can be shown that $\text{rank}(N_k) = 5$. This corresponds to the two back actuators and three independent side actuators.

Only the actuators that are linearly dependent can be changed freely. The six actuators located on the sides of the head are selected by $S_N = [I_6 \ 0_{6 \times 2}]$. Active constraints limit the solution space of the optimization which usually results in a decreased performance. This can be seen in Fig. 7-8.

The optimization problem is then written as:

$$\begin{aligned} \Delta u_{k+1} = \arg \min_{\Delta u} & \underbrace{\frac{1}{2} \Delta u^T H \Delta u + c^T \Delta u}_{\text{Quadratic objective}} + \underbrace{\sigma p(\Delta u)^T p(\Delta u)}_{\text{Penalty constraint}} \\ \text{s.t.} & \underbrace{K \Delta u - b \leq 0}_{\text{Linear constraints}} \end{aligned} \quad (7-28)$$

Table 7-1: Objective function and constraints for the optimization.

| | Equation | Description |
|-------------------------|---|--|
| Objectives | | |
| Zero tracking error | $\ L^{-1}(r - y_k - M_k \Delta u)\ _2^2$ | Main objective; eliminate misalignments |
| Decrease clamping force | $\lambda \left\ 1 - \frac{S_N(F_k + N_k \Delta u)}{F_{\min}} \right\ _2^2$ | Regularization; ¹ patient comfort |
| Minimum clamping force | $\sigma \left\ \max \left(0, 1 - \frac{S_N(F_k + N_k \Delta u)}{F_{\min}} \right) \right\ _2^2$ | Penalty function; ² soft constraint for adequate fixation |
| Constraints | | |
| Actuator inputs | $0 \leq (u^m + \Delta u^m) \leq 1$ | Physical constraint; actuator saturation |
| Maximum clamping force | $F_k + N_k \Delta u \leq F_{\max}$ | Safety constraint |

¹ Without regularization the problem becomes singular and the solution becomes unreliable. The value of the regularization parameter λ is chosen such that this norm is lower than the norm of the tracking error. It should have a minimum influence on the alignment process.

² The minimum clamping force is added as a soft constraint as opposed to a hard constraint like the maximum force. If both are hard constraints it is possible that no solution exists. It is better to have a too low clamping force with decreased fixation performance, than a too high clamping force that can result in injury to the patient. A penalty function is used instead of a barrier function since it is defined for all values, not only feasible ones. The penalty coefficient σ is kept constant and its value is chosen such that when the constraint is violated this norm becomes higher than that of the tracking error.

where

$$\begin{aligned}
W &= (L^T L)^{-1}, \\
H &= 2M_k^T W M_k + \frac{2\lambda}{F_{\min}^2} N_k^T S_N^T S_N N_k, \\
c &= -2M_k^T W (r - y_k) - \frac{2\lambda}{F_{\min}^2} N_k^T S_N^T (F_{\min} - S_N F_k), \\
p(\Delta u) &= \max \left(0, 1 - \frac{S_N(F_k + N_k \Delta u)}{F_{\min}} \right), \\
S_m &= \begin{bmatrix} 0_{8 \times 6} & I_8 \end{bmatrix}, \quad (\text{selects only the membrane actuators}) \\
K &= \begin{bmatrix} \frac{N_k}{F_{\max}} \\ S_m \\ -S_m \end{bmatrix}, \quad b = \begin{bmatrix} 1 - \frac{F_k}{F_{\max}} \\ 1 - S_m u_k \\ S_m u_k \end{bmatrix}.
\end{aligned} \tag{7-29}$$

Without the penalty term, the optimization problem is quadratic with linear constraints. The Hessian of the objective function is positive definite, which makes it a convex optimization problem. For any convex optimization problem a local minimum is also the global minimum and thus the solution is optimal [73]. The penalty term is convex and the sum of a strictly convex function and a convex function is again strictly convex [73]. Therefore the optimization problem including the penalty function is also convex. The solution is found with the MATLAB builtin function ‘fmincon’ (a constrained solver). It is set to use the ‘sequential quadratic programming (SQP)’ algorithm [61]. This algorithm performs a series of quadratic optimizations with linear constraints which coincides with the original optimization problem when the penalty constraint is inactive. If the initial conditions are feasible, then the actual values are irrelevant since the global minimum is always reached. That said, the initial conditions are set to $\Delta u = 0$.

7-3-3 Nonlinear Observer: an Extended Kalman Filter

An extended Kalman filter is implemented to estimate the state (x) of the system. It is desired to know the state so that the linearization in Section 7-2-1 yields more accurate results. It is also used to give a better estimate of the output of the system.

It was already shown in Section 7-2-2 that the system is locally observable. The extended Kalman filter is a nonlinear extension to the linear Kalman filter (see Appendix F for the algorithm). It estimates the state based on the linearized system matrices:

$$M_k = \left. \frac{\partial f}{\partial x} \right|_{\hat{x}_{k-1|k-1}, u_k} \quad \text{and} \quad H_k = \left. \frac{\partial h}{\partial x} \right|_{\hat{x}_k|k-1, u_k}. \quad (7-30)$$

for a linear time-invariant (LTI) system with additive white noise and known covariances the linear Kalman filter gives the unbiased minimum-error variance estimate of the state [71]. Considering that this system is slightly nonlinear for small misalignments, it can be assumed that the extended Kalman filter similarly gives a close to optimal estimate.

Process and Measurement Noise

Equation (7-4) is only valid for the ideal case when there is no process or measurement noise present. If noise is added, the resulting system looks like:

$$x_{k+1} = f(x_k, u_k) + v_k, \quad v_k \sim \mathcal{N}(0, Q) \quad (7-31)$$

$$y_k = g(x_k, u_k) + w_k, \quad w_k \sim \mathcal{N}(0, R) \quad (7-32)$$

where v_k is the process error caused by uncertainties in the corrections and w_k is the measurement error. Both are assumed to be normally distributed with the following constant covariance matrices:

$$Q = \begin{bmatrix} Q_{\text{couch}} & 0 & 0 \\ 0 & Q_{\text{body}} & 0 \\ 0 & 0 & Q_{\text{device}} \end{bmatrix} \quad \text{with} \quad \begin{cases} Q_{\text{couch}} = \underbrace{\begin{bmatrix} (0.05^\circ)^2 I_3 & 0 \\ 0 & (0.1 \text{ mm})^2 I_3 \end{bmatrix}}_{\text{See requirements: Table 3-1}}, \\ Q_{\text{body}} = Q_{\text{couch}}, \\ Q_{\text{device}} = \begin{bmatrix} (1 \text{ mm})^2 I_2 & 0 \\ 0 & (0.5^\circ)^2 I_3 \end{bmatrix} \end{cases} \quad (7-33)$$

and

$$R = \begin{bmatrix} R_{X\text{-ray}} & 0 & \cdots & 0 \\ 0 & R_{X\text{-ray}} & \cdots & 0 \\ \vdots & \vdots & \ddots & \vdots \\ 0 & 0 & \cdots & R_{X\text{-ray}} \end{bmatrix} \quad \text{with} \quad R_{X\text{-ray}} = \underbrace{\begin{bmatrix} (0.3^\circ)^2 I_3 & 0 \\ 0 & (0.4 \text{ mm})^2 I_3 \end{bmatrix}}_{\text{See requirements: Table 3-1}}. \quad (7-34)$$

7-4 Model Personalization: Parameter Estimation

M_k and N_k are derived from a standard anatomical model of the head and neck. The idea of a parameter estimation method is to calibrate the parameters of this model (dimensions, mass, stiffnesses, etc.) such that it better matches the individual patient. In theory the adapted model will improve the controller and therefore reduce the number of iterations that is needed to align the patient. The parameter estimation is done in between fractions and therefore only has an indirect effect on the alignment process.

A distinction is made between constant parameters and parameters that can vary between fractions. The parameter vector θ is partitioned as:

$$\theta = \begin{bmatrix} \theta_{\text{static}} \\ \theta_{\text{dynamic}} \end{bmatrix} \quad (7-35)$$

where θ_{static} contains the anatomical dimensions of the patient. These are assumed to be constant for the entire duration of the treatment. θ_{dynamic} contains the dynamic parameters related to weight loss, swelling, tumor shrinkage and the stiffnesses of the neck.

The parameter update equation for fraction l is:

$$\theta_{l+1} = \theta_l + v_l, \quad (\text{random walk}) \quad v_l \sim \mathcal{N}(0, Q_\theta) \quad (7-36)$$

$$y_l = y(\hat{x}_l, u_l, \theta_l) + w_l, \quad w_l \sim \mathcal{N}(0, R) \quad (7-37)$$

where \hat{x}_l is the final estimated state and u_l is the input that was used to align the patient. The system output function is parameterized as $y(x, u, \theta)$. An extended Kalman filter is then used to estimate the parameters (θ). Q_θ is the covariance matrix that specifies how fast the parameters must react. R is the measurement covariance matrix. The measurement passed to the Kalman filter is the direct X-ray measurement from the last iteration of the fraction.

7-5 Simulation and Verification

The performance of the immobilization device and the controller are checked with several different simulations. The main points of interest are the alignment error after a correction and the fixation during the fraction.

7-5-1 Simulation Procedure

The simulation tries to replicate the real world scenario as accurately as possible. In general, the procedure as shown in Fig. 7-1 is followed. The simulations are implemented in MATLAB. Pseudo-code of the process is shown in Algorithm 1. The steps are as follows:

1. The simulation starts by generating a reference configuration with a corresponding reference pose. In practice previous actuator inputs will be used as a starting point for the next fraction, but these are unknown to the simulation.

The control input (u_0) for which the system is in equilibrium at a reference state x_0 is found by the following constrained optimization problem:

$$\begin{aligned}
 u_0 = \arg \min_u \quad & \|u\|_2^2 \\
 \text{s.t.} \quad & \|\delta\Pi(x_0, u)\|_2^2 = 0 \\
 & 1 - \frac{F_i(x_0, u)}{F_{\min}} \leq 0 \\
 & \frac{-d_i(x_0, u)}{d_{\max}} \leq 0 \\
 & 0 \leq u_i^m \leq 1
 \end{aligned} \quad \left. \vphantom{\begin{aligned} u_0 = \arg \min_u \quad & \|u\|_2^2 \\ \text{s.t.} \quad & \|\delta\Pi(x_0, u)\|_2^2 = 0 \\ & 1 - \frac{F_i(x_0, u)}{F_{\min}} \leq 0 \\ & \frac{-d_i(x_0, u)}{d_{\max}} \leq 0 \\ & 0 \leq u_i^m \leq 1 \end{aligned}} \right\} \text{For each actuator } i \quad (7-38)$$

where $\delta\Pi(x_0, u)$ is the variation of energy that determines whether all the forces are in equilibrium. $F_i(x_0, u)$ is the force applied by actuator i , F_{\min} is the minimum clamping force, $d_i(x_0, u)$ is the stroke of actuator i and d_{\max} is the maximum stroke used to scale the constraint. This input will be used as a starting point for subsequent simulations.

2. For each simulation a new configuration is generated with an offset for the body. This offset is a random pose, normally distributed with zero mean and covariance matrix:

$$P^b = \text{diag}(0, 0, 1^{\circ 2}, 5 \text{ mm}^2, 5 \text{ mm}^2, 0). \quad (7-39)$$

It simulates the procedure of the patient lying down on the treatment couch and putting its head inside the immobilization device. Because, even when using the laser guidance system, the body (and similarly the head and neck) will not lie in exactly the same spot as the previous fraction. Offsetting the body generates three problems that need to be accounted for during the simulations:

- (a) The first problem is that of finding a feasible starting position of the head and neck. This problem was already explained in Section 6-2-2. If the head is placed randomly inside the immobilization device, it is possible that the system becomes unfeasible. Therefore, when generating a new configuration with a random body offset the head will be placed inside the device using inverse kinematics.
 - (b) The second problem is that of finding the new locations on the head and neck where the actuators make contact. It is important to know these locations since they not only determine M_k and N_k but also the current stroke of the actuators and the resulting equilibrium. To find these locations, a basic 3D model of the head and neck [74] is imported. A ray-triangle intersection algorithm [75] is implemented to find the intersection point of the actuators with the 3D mesh (Fig. 7-2).
 - (c) The third problem is that if the offset is too large, the desired reference cannot be reached. Most of the times the actuators saturate and the next-best solution is found. However, sometimes this large offset causes the optimization of the equilibrium to fail, resulting in unpredictable behavior. These simulation results are discarded.
3. For each iteration the new state and output are computed according to the nonlinear state space model (Eq. (7-4)). Each iteration corresponds to a single correction of the misalignments. A fixed number of iterations is simulated. In practice a heuristic is implemented to stop when the alignment is sufficient.

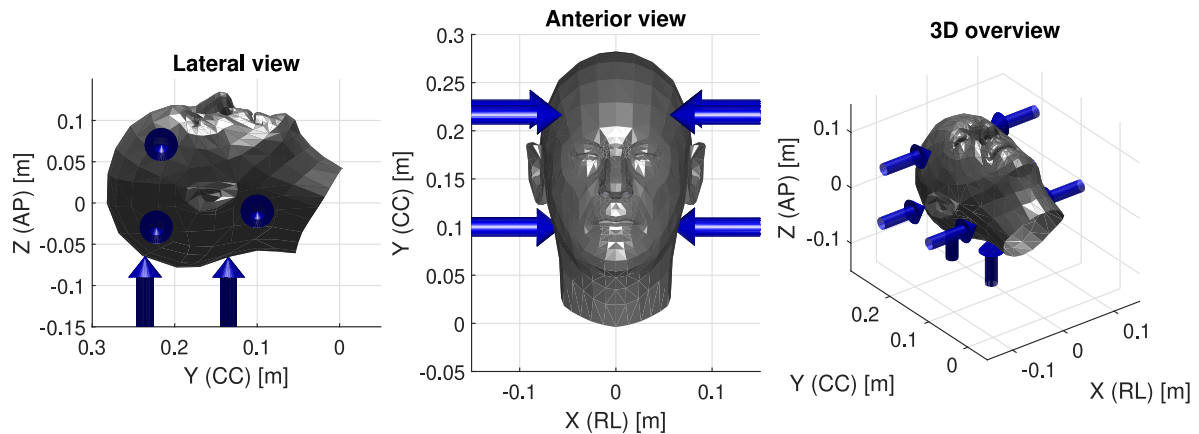


Figure 7-2: The 3D mesh of the head and neck [74] used to find the contact points of the actuators. A ray-triangle intersection algorithm [75] is implemented to find the intersection point of the actuators (rays) with the 3D mesh (triangles). The head is scaled to match the dimensions used in the rest of the model. From left to right: A lateral view showing the five independent actuators. An anterior view showing the two sets of three actuators on opposing sides of the head. Only three of these actuators are linearly independent. And lastly, another overview of the head.

4. The new actuator forces are calculated according to Eq. (5-13). In practice the forces would be estimated from Fig. 5-12b. The noise on the force measurements is assumed to be $v_F \sim \mathcal{N}(0, I)$.
5. The state is estimated by an extended Kalman filter as described in Section 7-3-3.
6. The system is linearized around the estimated state and the new M_k and N_k are calculated as shown in Eqs. (7-25) and (7-27). The controller can be used with or without an observer. If it is used without an observer, M_k and N_k are calculated once for the initial state and kept constant for the duration of the simulation.
7. Using the calculated alignment errors and the estimated clamping forces the new control input is found by the constrained optimization of Eq. (7-28). If the force correction is disabled, it uses a simpler algorithm that is similar to Eq. (7-26) but with bounded actuator inputs.

Algorithm 1: Simulation of the alignment procedure with a random body offset.

Initialize reference configuration

Find control input corresponding to initial state

for All simulations ($1, \dots, 100$) **do**

Initialize new configuration with a random body offset

for All iterations ($k = 0, \dots, 4$) **do**

Update state space system

Measure output and actuator forces

Estimate new state using Kalman filter

Calculate and apply new control input

end

end

Table 7-2: 1D alignment errors in the three directions: left-right (LR), cranial-caudal (CC) and anterior-posterior (AP). These correspond to the X-, Y-, and Z-axis in Fig. 6-2, respectively. Only the rotational error in AP-direction (highlighted) is significantly impacted by the force correction. The errors are compared to values found in literature.

| | Rotations | | | Translations | | |
|----------------------------------|-----------|------|------|--------------|------|------|
| | LR | CC | AP | LR | CC | AP |
| Simulated: | | | | | | |
| Without force correction | 0.31 | 0.33 | 0.34 | 0.64 | 0.27 | 0.38 |
| With force correction | 0.27 | 0.36 | 0.74 | 0.72 | 0.29 | 0.40 |
| Examples from literature: | | | | | | |
| Polat et al. [33] | 0.7 | 0.6 | 0.7 | 1.1 | 0.6 | 1.0 |
| Giske et al. [21] | 0.7 | 0.7 | 0.7 | 1.6 | 1.3 | 1.5 |

7-5-2 Alignment Performance

This study mainly focuses on the alignment of the head with respect to the body. Therefore the simulated system contains two ROIs: the body and the skull. Unless otherwise specified, the errors in this section are the root mean square (RMS) 3D alignment errors. This means that when multiple ROIs are measured, for each ROI the 3D rotational error and 3D translational error is calculated. Then the RMS values of each of these 3D errors is calculated. In Appendix B-3 the relation between 1D and 3D errors is explained. Also, unless otherwise specified, the controller uses an observer and includes force correction.

In Table 3-1 the requirements on the alignment errors are listed. They are a maximum rotational error of 1.1° and a maximum translational error of 1.9 mm (with 95 % certainty).

In Fig. 7-3 the median alignment errors of the system are shown for consecutive corrections. The red dotted line denotes the maximum error in 95 % of the simulations and the black dotted line denotes the requirement. The requirements are satisfied if the red line drops below the black line. The whiskers of the boxes contain approximately 99.3 % of the errors. The percentage of simulations that succeeded in satisfying the error requirements after a single correction is shown in the title.

From Fig. 7-3 it is clear that the system with force correction performs worse than without. Most notably the rotational error is affected. This is further investigated in Table 7-2. While most of the errors are similar, the rotational error in AP-direction has doubled. This is most likely because the back actuators (responsible for the AP-direction) are not part of the force correction procedure. Even though the system performs worse without force correction it is still recommended to enable it to reduce intrafraction motion. In both cases the translational error requirements are fulfilled after a single iteration. Only in the case without force correction the rotational error requirements are also satisfied.

In Fig. 7-4 the probability of exceeding a given error is shown. It shows the system with and without force correction and with and without observer. The effect of the observer is not visible after a single iteration. Significant performance gains are only visible after several iterations. This can also be seen in Fig. 7-5 where the error between the real pose and the estimated pose is shown. After one iteration there is no significant difference between the systems with and without observer. The observer needs more iterations to be able to gain an

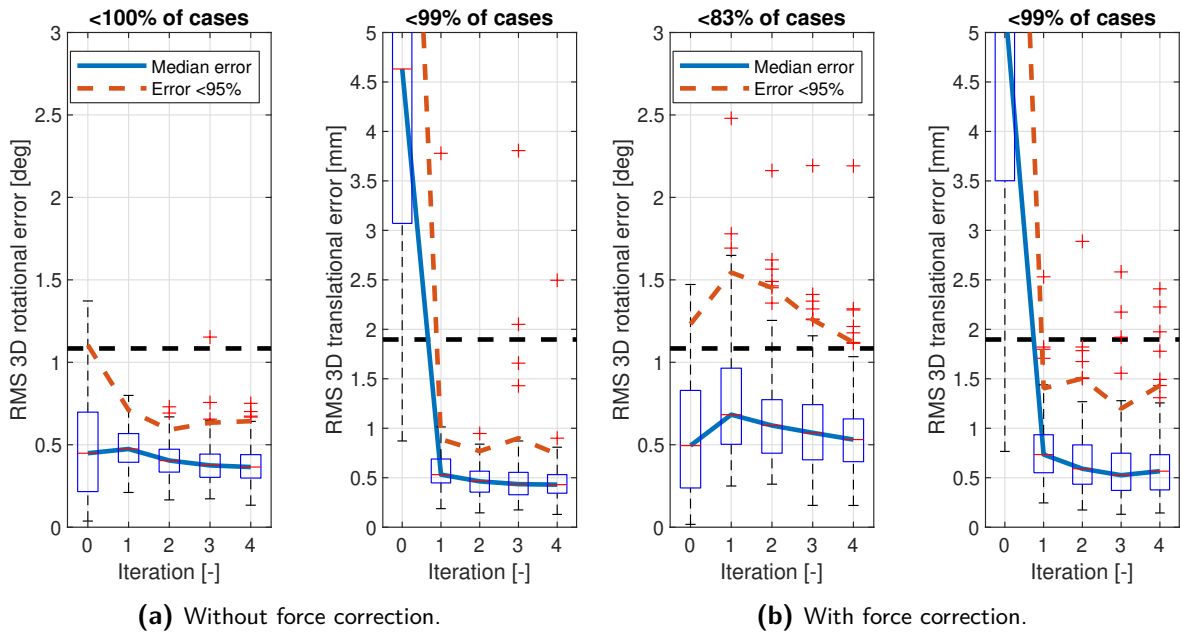


Figure 7-3: The median of the rotational and translational errors of the head and neck for consecutive corrections (iterations). In both cases the translational error requirements are fulfilled after one iteration. Only in the case without force correction the rotational error requirements are also satisfied.

advantage.

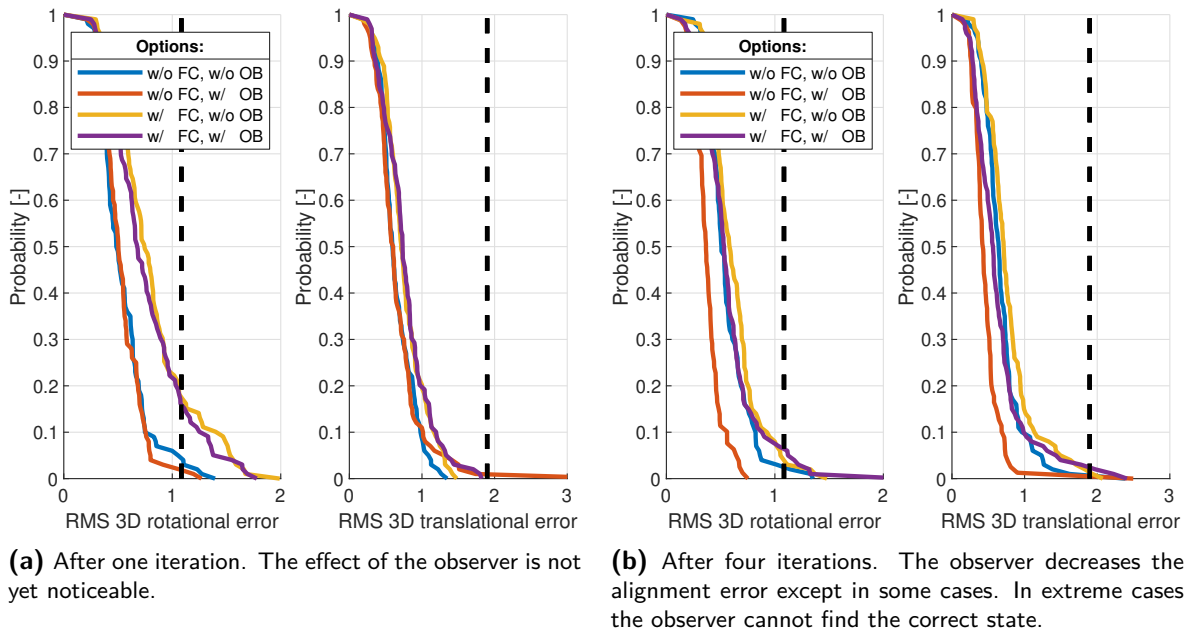


Figure 7-4: The probability of exceeding a given error, either rotational or translational. A comparison of different controller options is given. The abbreviations are: with (w/), without (w/o), force correction (FC), and observer (OB). The observer increases the performance of the controller slightly, both with and without force correction. The force correction decreases the performance significantly.

Table 7-3: A comparison of the alignment errors between the state-of-the-art, the desired errors given by the requirements and the errors resulting from the simulations.

| | Rotations | Translations |
|---------------------------------|-----------|--------------|
| State-of-the-art | 2.1 | 3.5 |
| Requirements | 1.2 | 2.1 |
| Simulation results ¹ | 1.7 | 1.5 |

¹ After a single iteration.

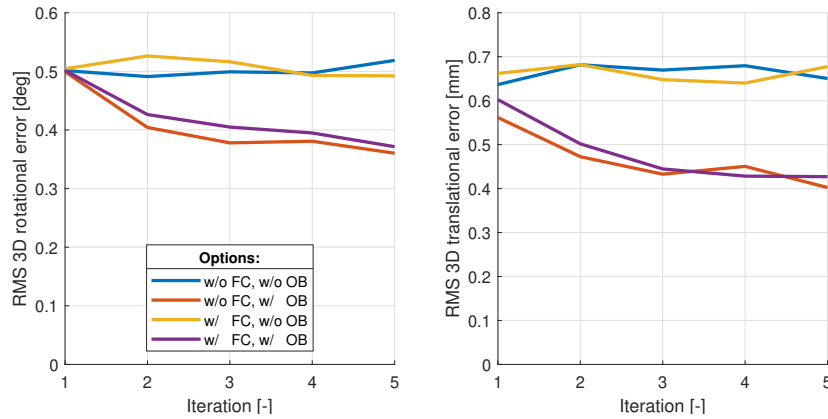
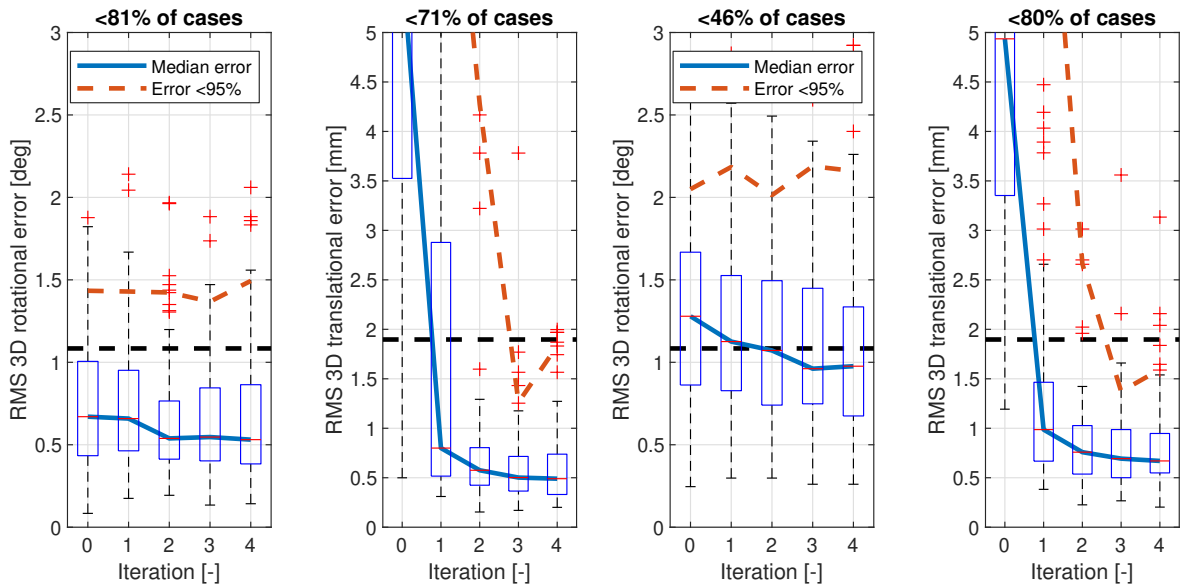


Figure 7-5: An evaluation of the observer performance. Shown are the rotational and translational errors between the real pose and estimated pose. The abbreviations are: with (w/), without (w/o), force correction (FC), and observer (OB). The results are averaged over 100 simulations. The observer improves the localization performance. The errors of the pure measurements are constant and agree with the chi distribution (Appendix B-3). Namely: $\mu_{\text{rot}} = 1.60 \cdot 0.3 = 0.48^\circ$ and $\mu_{\text{rot}} = 1.60 \cdot 0.4 = 0.64 \text{ mm}$.

In Fig. 7-6 the alignment errors of a system with more than two ROIs are shown. The errors of Fig. 7-6a are comparable to those of Fig. 7-3b (the system with two ROIs). In Fig. 7-6b the body offset was approximately doubled. The translational error seems unaffected but the rotational error has also doubled.

For a system with a single ROI, one would expect that corrections using purely the treatment couch are sufficient. In Fig. 7-7a the control input of a single ROI system is compared to that of the system with two ROIs. For a single ROI, one can see that the treatment couch performs the corrections and the actuators in the immobilization device only try to correct the clamping force. For systems with multiple ROIs, both are actively correcting the errors. The alignment performance of single ROI system is excellent, as shown by Fig. 7-7b.

In Table 7-3 the alignment errors of current alternative methods are compared to the results (for two ROIs). The rotational error has decreased by 19% and the translational error by 57% compared to existing methods. Although the rotational error does not satisfy the requirements, it is still better than alternative methods.



(a) Measured ROIs: the body, C5, C2 and the skull. The translational error after one iteration has a lot of variation. Although the median is well below the dotted line, the upper whisker extends to 6.5 mm.

(b) Measured ROIs: C5, C2 and the skull. This time the initial body offset is approximately doubled. As a result the rotational error also doubles.

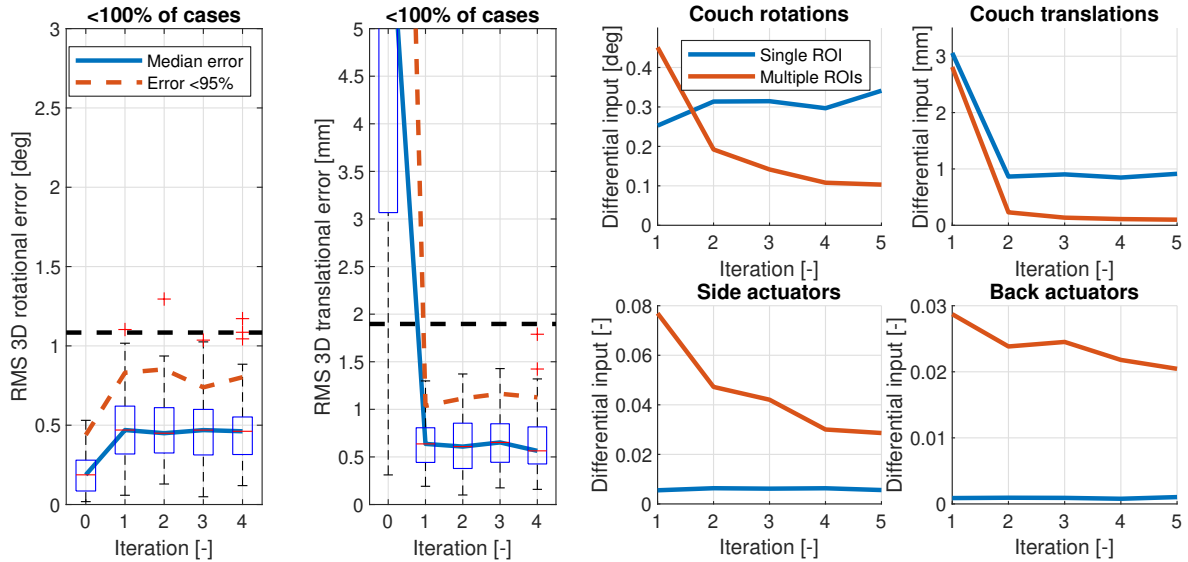
Figure 7-6: The alignment errors for systems with more than two ROIs. Vertebra C5 was added to the model using inverse kinematics as described by Section 6-2-2. It is mostly responsible for the large rotational errors. In both cases the rotational error exceeds the given requirements. The translational alignment is sufficient after two iterations.

7-5-3 Fixation Performance

A good fixation is important in reducing intrafraction motion and keeping the patient aligned. In Table 5-4 the minimum stiffness of the actuators was determined. If the moments that were calculated in Table 5-3 are applied one at a time, then the 1D alignment errors are shown in Table 7-4.

The fixation performance is ensured by maintaining a constant clamping force. The controller automatically corrects the clamping force to the desired value (15 N). In Fig. 7-8 it is shown that the force correction is successful in maintaining a desired clamping force. The reference case is without force correction, which understandably results in the best alignment. In the second case the minimum clamping force is increased to 25 N (from the default 15 N). The clamping force is reached but the rotational alignment performance has decreased (see also Table 7-2). The third case is added to illustrate what happens when the minimum clamping force and maximum clamping force constraints are in conflict. The soft constraint placed on the minimum force has to yield to the hard constraint on the maximum force. The result is that the clamping force correctly reaches the maximum force, but because of the higher cost in the objective function a less ideal alignment is found.

The force correction negatively affects the rotational alignment errors. This effect was already shown in Table 7-2.



(a) The errors are comparable to that of Fig. 7-3a. In all cases the error requirements are fulfilled.

(b) The control input (averaged per category) to the treatment couch and actuators, averaged over 100 simulations. What is shown is the difference in control input from one iteration to the next. It is interesting to see that in both cases, while the error stabilizes after a single iteration, the control input is never constant.

Figure 7-7: A case with only a single ROIs, namely the skull. A system with a single ROI is not observable (Section 7-2-2). The control input is compared to that of Fig. 7-3b.

Table 7-4: Fixation errors due to an applied moment. The magnitude of this moment is determined by the subconsciously generated moments listed in Table 5-3. The errors are below those specified by the requirements, indicating that the fixation is satisfactory.

| Type | Applied moment [N m] | 1D alignment error | |
|--------------------------|----------------------|--------------------|-------------------|
| | | Rotations [deg] | Translations [mm] |
| Extension | 1.30 | 0.14 | 0.10 |
| Lateral bending | 0.64 | 0.06 | 0.09 |
| Axial rotation | 0.43 | 0.14 | 0.48 |
| Requirements (Table 3-1) | - | 0.30 | 0.60 |

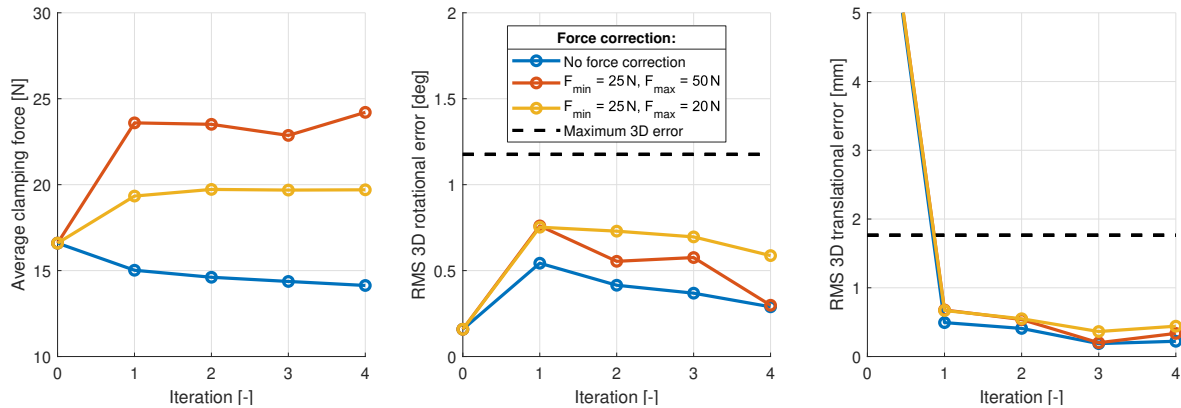


Figure 7-8: The effect of force correction on the alignment. The reference case is without force correction, which understandably results in the best alignment. Note that the translational alignment remains largely unchanged.

7-5-4 Parameter Estimation Results

The parameter estimation method is tested for two different parameters. These are the length of the neck (the distance between C7 and the center of gravity of the head) and the mass of the head. The length is a static parameter and the mass is a dynamic parameter.

The update equation of the real parameters during the simulation is:

$$\theta_{k+1} = \begin{bmatrix} 1 & 0 \\ 0 & 0.95^{0.1} \end{bmatrix} \theta_k, \quad \theta_0 = \begin{bmatrix} 0.194 \text{ m} \\ 4.36 \text{ kg} \end{bmatrix} \quad (7-40)$$

The length of the neck is increased by 10% and kept constant. The mass of the head decreases 5% every ten fractions (simulating weight loss).

In Fig. 7-9 the new length is correctly estimated after approximately five fractions. Despite the observability matrix being full rank, the mass could not be estimated reliably. This is because the singular value of the observability matrix for the mass is approximately 2000 times lower than that of the neck length. Even the change in neck length has a minimal effect on the alignment. The performance gain is negligible which can mean two things: that the controller is robust to uncertainties in the model. And that, unless you need to know the actual parameters, the parameter estimation is unnecessary.

7-5-5 Verification with a Clamped Cantilever Beam

A proof of principle is built using a cantilever beam. It is visualized in Fig. 7-10. The beam is fixed on one end and clamped between two actuators on the other. This setup approximates the lateral bending of the neck. The length of the beam is $L_{\text{beam}} = 0.30 \text{ m}$ and there are two opposing actuators placed at $L_{\text{act}} = 0.2164 \text{ m}$. The thickness and width of the beam are chosen such that the bending stiffness is $1.06 \text{ N m rad}^{-1}$, equal to that of the neck (Table 6-3).

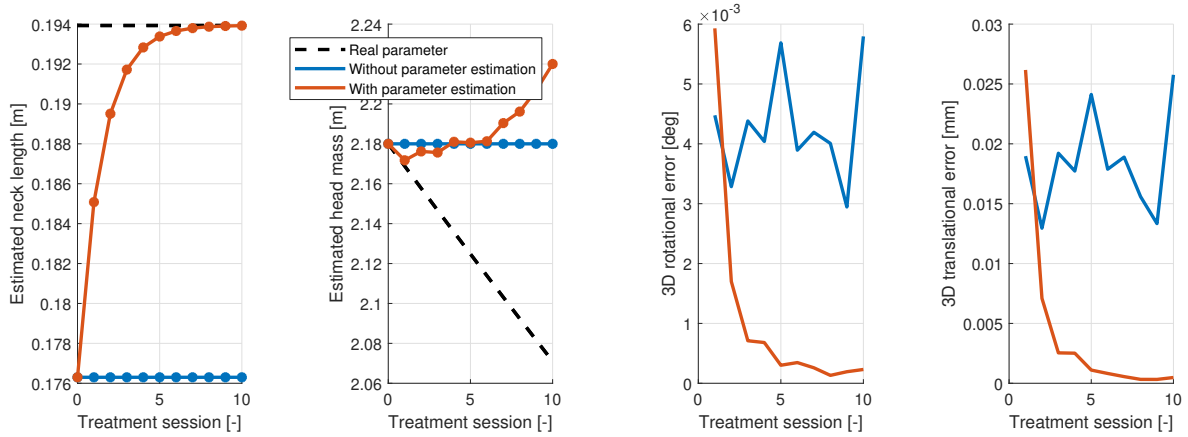


Figure 7-9: Estimation of model parameters and the effect on the alignment over a duration of ten fractions (a typical treatment consists of 30 fractions). The estimated parameters are the neck length and the mass of the head. The length is estimated correctly after approximately five fractions while the mass cannot be observed. The real values are given by Eq. (7-40) or by the dotted lines in the figure. This simulation was performed without any measurement noise. The variation of the alignment error is due to the random body offset at the beginning of each fraction. It can be seen that even without noise in the system the performance gain is very small (approximately 4×10^{-3} for rotations and 0.015 mm for translations).

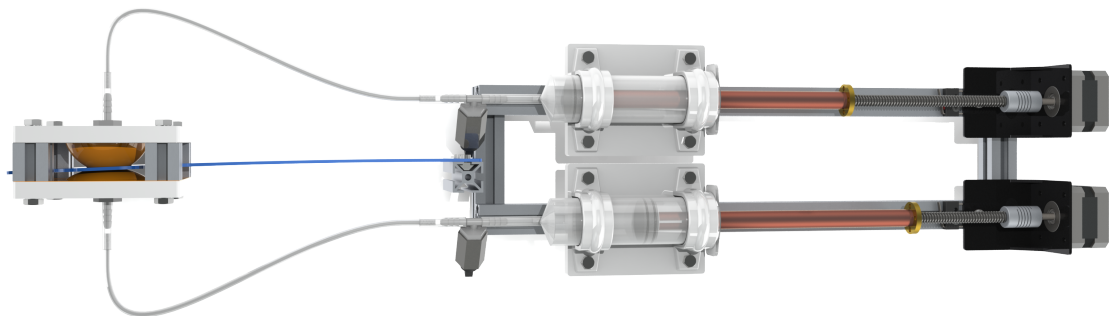


Figure 7-10: A dual actuator setup clamping a simple cantilever beam. This setup serves as a proof of principle.

Chapter 8

Conclusion

An immobilization device was designed to automatically align the head and neck of a patient. This device uses two orthogonal X-ray projections in combination with a 3D-2D registration method to calculate the alignment error. The global alignment is done by the six degree of freedom (DOF) treatment couch whereas local alignments, of the head with respect to the body, are done by the immobilization device.

The alignment errors after a single correction are similar to or lower than those of existing immobilization methods. For a simple case of two regions-of-interest (ROIs), namely the body and the head, the 3D rotational error was reduced by 20% and the translational error by almost 60%. For more complex cases with four or more ROIs the translational errors did not change, but the rotational errors increased to those similar to the thermoplastic mask.

The immobilization device boasts an open design that is as comfortable as possible for the patient. It is also suitable for use in CT and MRI machines because it contains no metals and is made out of a thin shell with low density gradients. It contains eight actuators to immobilize and align the patient. The six actuators at opposing sides of the head and neck were optimized separately from the two at the back. With this configuration any five DOF motion of the head is possible (excluding translations in cranial-caudal (CC) direction).

The actuators consist of a inflatable rubber membranes that have a negligible effect on the proton beam. The membranes also follow the contours of the head and have a relatively large contact area for optimal comfort. The usage of a closed-volume pneumatic system offers the ability to not only detect intrafraction motion but also to estimate and correct the clamping force on the head and neck. The force correction increases the fixation performance but doubles the rotational alignment error in the anterior-posterior (AP) direction. This causes relatively high rotational errors compared to the translational errors.

The adaptation to the patient is two-fold. First it can adapt to different head sizes by adjusting the actuators. With five different device sizes most of the patients can be immobilized. Then there is also the possibility to adapt the model parameters to the patient. This is deemed unnecessary due to the inherent robustness of the controller.

Because local corrections are possible with this device, the initial alignment of the patient becomes less important. It can therefore be done faster. For the general use case, a single

correction is sufficient. The duration of a single correction is primarily determined by the time that is needed for the 3D-2D registration. This can take up to several minutes. In conclusion, it can be expected that the average setup time for the patient decreases by 50%. Such a reduction increases the throughput of patients by 15%.

Future Research

This study demonstrates that an adaptive immobilization device is feasible and merits a more thorough investigation. A few things are listed that should to be researched before testing in clinical trials. They are ordered, with the most important first:

- The force correction introduces a large rotational error in anterior-posterior (AP) direction (Table 7-2). Investigate whether this is a problem in the controller (and thus can be solved) or whether it is a limitation of the system.
- Investigate whether the body can be assumed fixed to the treatment couch. A solution must also be found in immobilizing the mandible and hyoid bone.
- Investigate different membrane geometries and their properties (see Appendix E).
- Regions-of-interest (ROIs) that are not explicitly part of the model nor attached to one of the other ROIs are now added using inverse kinematics. These ROIs should be properly integrated into the model, preferably with their own generalized coordinates.
- Investigate whether the distance estimation of the membranes can improve (or possibly replace) the X-ray measurements. Also investigate the effect of a curved contact surface on the distance estimation.
- A possible improvement to the system can be to add more actuators in the neck. These will help to better align the individual vertebrae.
- Investigate what clamping forces the patient can tolerate. A higher clamping force results in a better fixation.

Appendix A

Medical Terminology

In this chapter some medical terms are explained. Also some relevant anatomy regarding the head and neck area is shown.

A-1 Directional Terms

The position of organs, bones, etc. are given in a reference frame relative to the patient. The directional terms are shown in Fig. A-1.

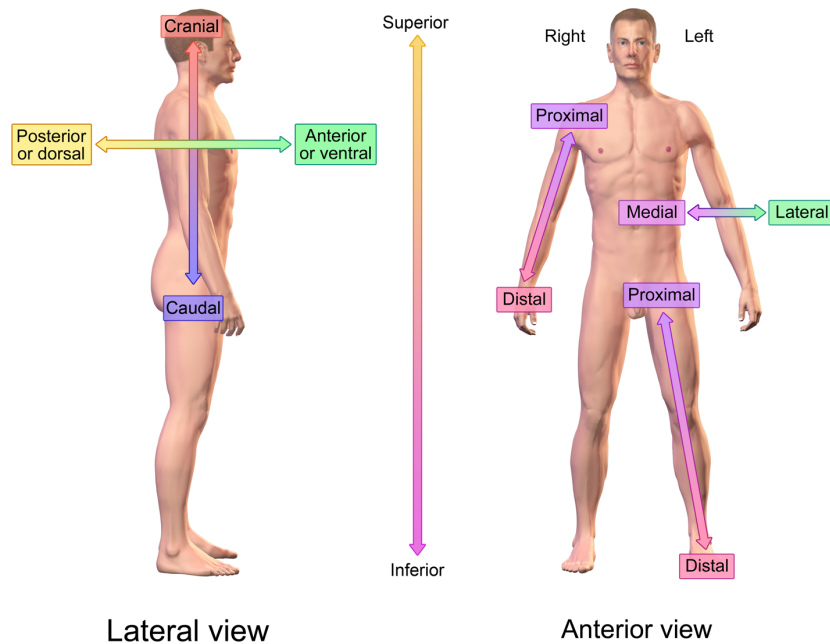


Figure A-1: Directional terms applied to the human body. From [76].

A-2 Relevant Head and Neck Anatomy

This study focuses on the head and neck area. In Fig. A-2 the bones in this area are labeled. Bones of note are: vertebrae T1 and C7-C1, the skull, the mandible and the hyoid bone.

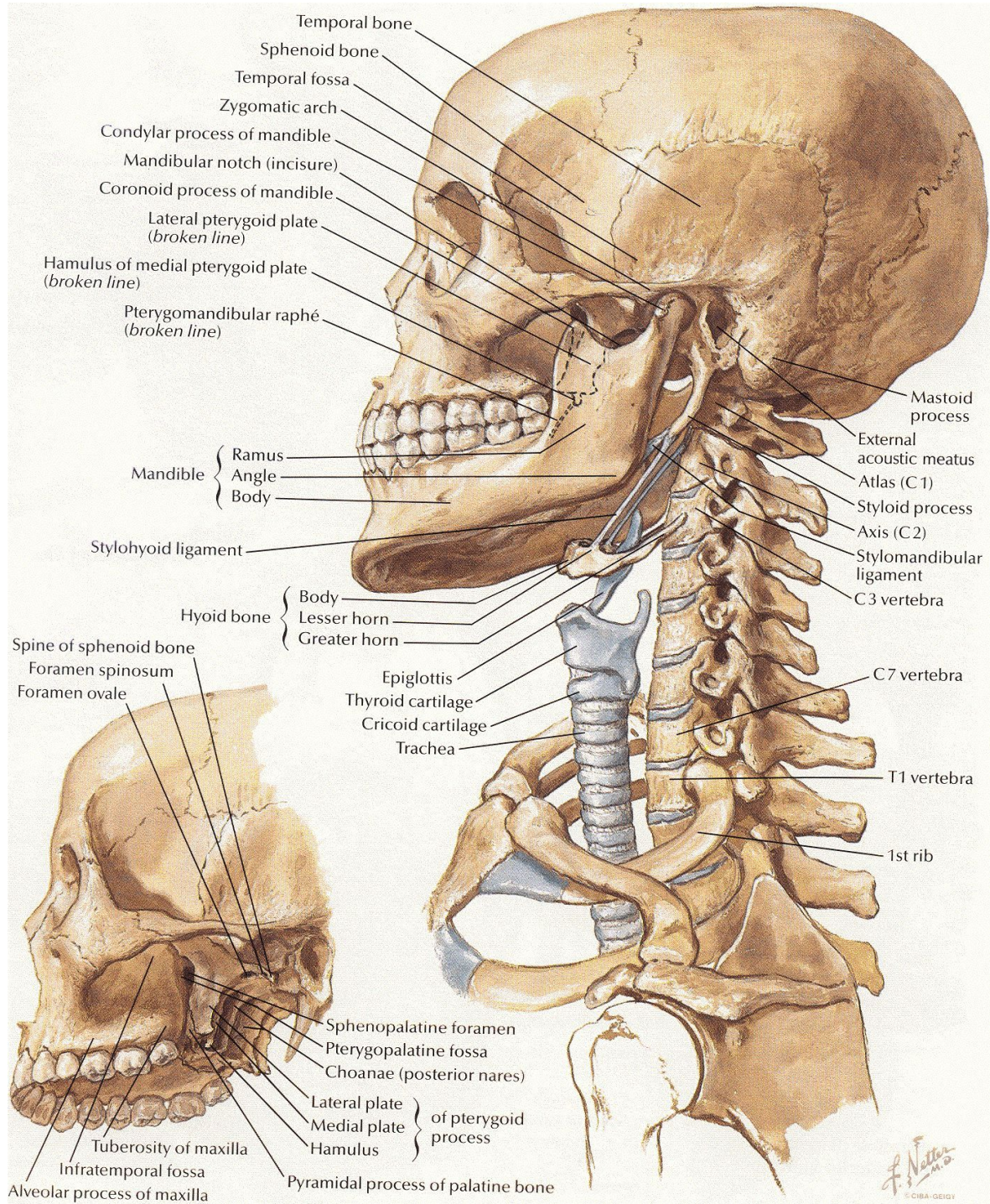


Figure A-2: The skeletal system of the head and neck. From [77].

Appendix B

Errors and Uncertainties

This chapter contains some extra information about state-of-the-art errors and how to calculate them.

B-1 Calculation of the Alignment Errors

A common method with which alignment errors are calculated is illustrated by van Herk [38] in Fig. B-1. A margin recipe that is widely used is: $2.5\Sigma + 0.7\sigma$ [38].

| | Patient 1 | Patient 2 | Patient 3 | Patient 4 |
|-------|-----------|-----------|-----------|-----------|
| Day 1 | 2 | 4 | 1 | 3 |
| Day 2 | 1 | -2 | -1 | -3 |
| Day 3 | 1 | 2 | 2 | -2 |
| Day 4 | 1 | 0 | 2 | 1 |
| Mean | 1.25 | 1 | 1 | -0.25 |
| SD | 0.50 | 2.58 | 1.41 | 2.75 |

↓

Mean = $M = 0.75$
SD = $\Sigma = 0.68$
RMS = $\sigma = 2.03$

Figure B-1: An example of how the alignment errors are calculated. For example: the values indicate the translational error in millimeters in LR-direction. From [38].

B-2 Rigid Body Errors

Most current alignment strategies treat the head and neck as a rigid body. In practice the head and neck will show local alignment errors. Some of these errors are listed in Table B-1.

Table B-1: The local alignment errors of the regions-of-interest (ROIs) after a rigid body correction. Several correction methods are compared. It can be seen that the random error increases with the number of ROIs. This is because local errors are not averaged out. Compare it with a single ROI where the error after correction is approximately to zero.

| Correction method | Number of ROIs | Translations (mm) | | Rotations (deg) | | Ref. |
|----------------------|----------------|-------------------|---------------|-----------------|---------------|------|
| | | RMS- Σ | RMS- σ | RMS- Σ | RMS- σ | |
| Mid-PTV ¹ | 4 | 1.7 | 1.1 | | | [19] |
| Min-max ² | 4 | 1.3 | 0.7 | | | |
| Rigid body | 5 | 1.4 | 0.9 | 1.0 | 0.7 | [33] |
| Rigid body | 8 | 1.5 | 1.3 | | | [18] |
| Mean ³ | 8 | 1.3 | 1.1 | | | |
| Min-max | 8 | 1.4 | 1.3 | | | |
| Rigid body | 8 | 1.4 | 1.4 | 0.7 | 0.7 | [21] |
| Rigid body | 13 | 1.8 | 1.6 | | | [20] |

¹ Minimize the vertebrae error in the middle of the planning target volume (PTV).

² Minimize the maximum error of the ROIs.

³ Minimize the mean error of the ROIs.

B-3 3D Errors: Chi Distribution

Thus far only 1D errors were listed. Sometimes it is desired to know the mean absolute displacement and the corresponding standard deviation (SD). This is called the 3D error. The errors in LR, CC, and AP directions are considered independent and identically distributed (IID). The 3D error is a new random variable, that follows the chi distribution. It is denoted by:

$$V = \sqrt{X^2 + Y^2 + Z^2}. \quad (\text{B-1})$$

For $X, Y, Z \sim \mathcal{N}(0, \sigma^2)$ the mean and SD of V are

$$\mu' = \sigma \sqrt{2} \frac{\Gamma\left(\frac{k+1}{2}\right)}{\Gamma\left(\frac{k}{2}\right)} \approx 1.60\sigma, \quad (\text{B-2})$$

and

$$\sigma' = \sigma \sqrt{k - 2 \left(\frac{\Gamma\left(\frac{k+1}{2}\right)}{\Gamma\left(\frac{k}{2}\right)} \right)^2} \approx 0.67\sigma, \quad (\text{B-3})$$

respectively. The number of degrees of freedom is denoted by $k = 3$.

Suppose that $E_{95\%}$ is larger than 95% of the 3D errors. Given a 1D error, this value can be calculated as:

$$E_{95\%} \triangleq \mu' + 1.65\sigma' \approx 2.71\sigma. \quad (\text{B-4})$$

This is used to calculate the 3D error requirements from the 1D errors.

Appendix C

Screw Theory

Chasles' theorem states that any motion of a rigid body can be described by a pure rotation along a line l together with a pure translation along l [67]. This line l is called the screw axis. The ratio between the translation and rotation is called the pitch λ .

C-1 Twists

Twists are a type of screw that describe the instantaneous velocity of the rigid body. A twist is denoted by:

$$T = \begin{bmatrix} \omega \\ v \end{bmatrix}, \quad T \in \mathbb{R}^6 \quad (\text{C-1})$$

where $\omega \in \mathbb{R}^3$ are the angular velocities and $v \in \mathbb{R}^3$ are the linear velocities. An alternative representation is the matrix form:

$$\tilde{T} = \begin{bmatrix} \tilde{\omega} & v \\ 0 & 0 \end{bmatrix}, \quad \tilde{T} \in \mathbb{R}^{4 \times 4} \quad (\text{C-2})$$

where $\tilde{\omega} \in \mathbb{R}^{3 \times 3}$ is a skew symmetric matrix such that $\tilde{\omega}a = \omega \times a$.

C-2 Wrenches

Wrenches are a type of screw that describe the forces applied to the rigid body. Similar to a twist, a wrench is denoted by:

$$W = \begin{bmatrix} m & f \end{bmatrix}, \quad W \in \mathbb{R}^6 \quad (\text{C-3})$$

where $m \in \mathbb{R}^3$ represents the torque and $f \in \mathbb{R}^3$ the linear forces. An alternative representation is the matrix form:

$$\tilde{W} = \begin{bmatrix} \tilde{f} & m^T \\ 0 & 0 \end{bmatrix}, \quad \tilde{W} \in \mathbb{R}^{4 \times 4} \quad (\text{C-4})$$

where $\tilde{f} \in \mathbb{R}^{3 \times 3}$ is a skew symmetric matrix such that $\tilde{f}a = \omega \times a$. Wrenches are duals to twists.

Appendix D

Concept Generation

In this chapter it is shown how the concepts are generated and which one is eventually chosen to function as a base design.

D-1 Morphological Chart

The adaptive immobilization must perform several functions. In Table D-1 options for each function are listed. A concept is generated by selecting a combination of options. This process is shown in Table D-1 by the colored lines (not every combination is possible). Three concepts are selected. The red, green and blue lines denote concepts 1, 2 and 3 respectively.

Each of these concepts uses the same indexing method. The indexing method provides a repeatable connection of the immobilization device to the treatment couch. It will be designed to be compatible to the couch top. A sketch of the general indexing concept is shown in Fig. D-1.

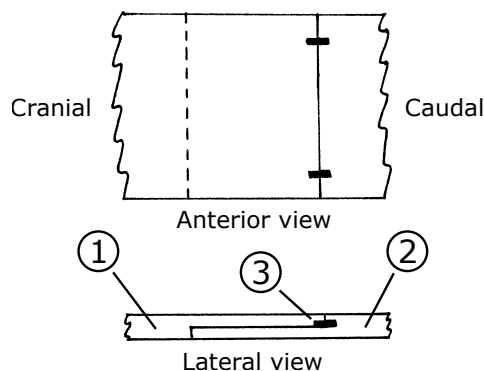
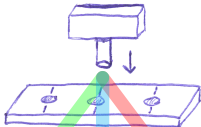
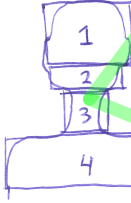
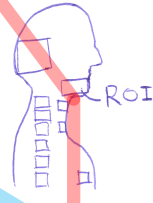
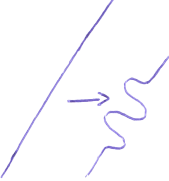
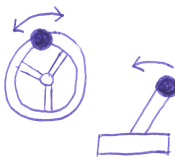
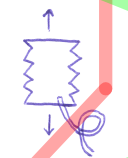
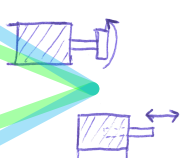
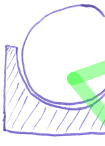
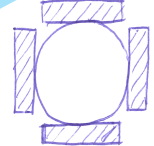
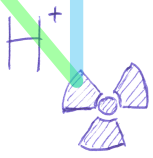


Figure D-1: The indexable couch top is identical for each concept. The cranial part of the couch top (1) supports the head and neck and is rigidly attached to the immobilization device. The caudal part of the couch top (2) supports the body. The indexation pins (3) ensure a repeatable and secure connection to the treatment couch.

Table D-1: The morphological chart used to design three concepts. The red, green and blue lines denote concepts 1, 2 and 3 respectively.

| [Weight] Function | [Score] Option 1 | [Score] Option 2 | [Score] Option 3 | [Score] Option 4 |
|--|--|---|---|---|
| [1] Alignment of the device on the treatment couch | [2] Lasers  | [5] Indexable  | | |
| [5] Localization of the ROIs ¹ | [2] Surface scanning  | [3] IR tracking  | [5] CBCT or stereoscopic X-ray  | |
| [3] Actuation | [1] SMAs or SMPs ²  | [2] Manual  | [3] Pneumatic or hydraulic  | [5] Electric  |
| [4] Fixation of the head and neck | [1] Open support  | [3] Force-closed  | [5] Shape-closed  | |
| [3] Compatibility with medical equipment | [1] Proton equipment only H^+ | [3] Proton and CT H^+  | [5] Proton, CT and MRI H^+  | |

¹ IR-tracking and surface scanning can be used as a deformable registration method if enough ROIs are tracked.

² Shape-memory alloys (SMAs) or shape-memory polymers (SMPs).

D-1-1 Concept 1: Stereoscopic X-ray, Pneumatic Actuation

This concept uses stereoscopic X-ray imaging to locate the regions-of-interest (ROIs). Because of the directional nature of the actuators, they are placed on both sides of the head and neck. This is shown in Fig. D-2. By simultaneous actuation of two opposing actuators, the head and neck can be clamped.

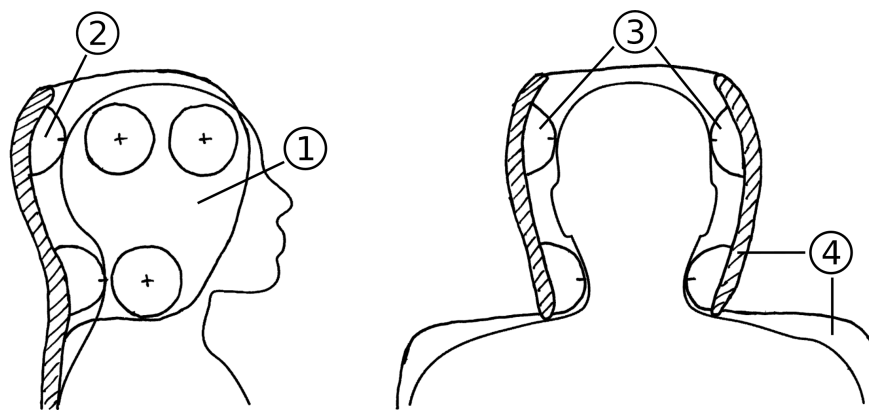


Figure D-2: Concept 1, as denoted by the red line in Table D-1. Left: lateral view, right: anterior view. Inflatable membranes (2). The head and neck are clamped into place by the actuators (3). The head and neck are enclosed for maximum fixation (1). The immobilization device is rigidly connected to the treatment couch (4).

Advantages of this concept:

- It can be extended with redundant actuators for finer and more robust motion control.
- There are no metal parts, therefore it is suited for use in CT and MRI devices.
- The bony anatomy is registered directly. This gives a good estimation of the location of the clinical target volume (CTV).
- The eyes, nose, ears and mouth are unobstructed. This improves the patient comfort and makes it easy to communicate with the radiographer.

Disadvantages of this concept:

- The stiffness of the actuators is relatively low due to the compressibility of air.
- Because of the nature of the measurement method, an extra radiation dose is given to the patient.
- The misalignment will only be corrected at the beginning of the fraction because continuous imaging is not desirable.

D-1-2 Concept 2: Surface Scanning, Electric Actuation

This concept uses surface scanning to locate the ROIs. The actuation is done with electric linear actuators that can translate and rotate the platform. This is shown in Fig. D-3. The head and neck will gently be held in place by gravity, since any other form of fixation will either obstruct the cameras or deform the surface.

Advantages of this concept:

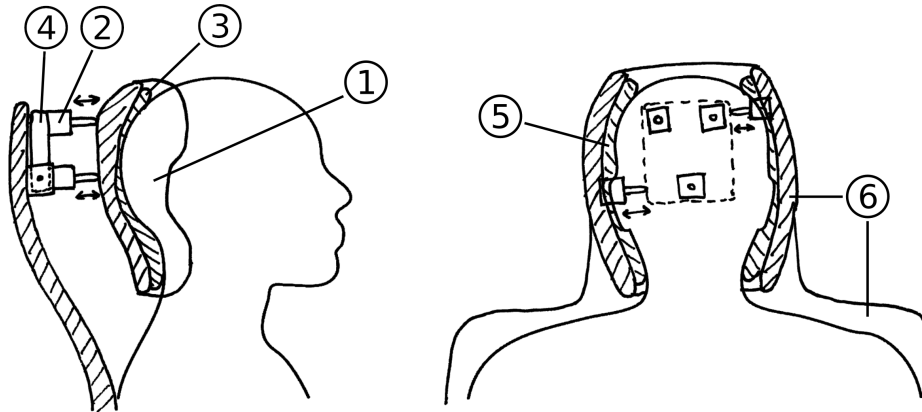


Figure D-3: Concept 2, as denoted by the green line in Table D-1. Left: lateral view, right: anterior view. To reduce artifacts in the CT scan, the actuators are moved away from the neck and towards the head as much as possible. The entire upper part of the skull can be seen as rigid and is therefore easier to register. Lead screw stepper motors (2). The intermediate platform for the translation in left-right (LR) direction and rotation in anterior-posterior (AP) direction (4). The head is lightly supported and the ears are not obstructed (1). A cushion provides comfort and a better fixation (3). Elastic foam presses firmly on the sides of the back of the head to keep it in place and not distort the imaged surface (5). The immobilization device is not directly fixed to the treatment couch (6).

- The patient setup time is low. The head and neck are simply supported and the surface scanning method can be used directly.
- The error can be corrected continuously, thus intra-fraction drift is eliminated.
- The eyes, nose, ears and mouth are unobstructed. This improves the patient comfort and makes it easy to communicate with the radiographer.

Disadvantages of this concept:

- If a high accuracy is desired or if the patient's surface has changed, the surface must be re-registered to the bony anatomy. For this a full CT scan is needed to register the CT surface to the imaged surface. Because of the full CT scan, a significant radiation dose is given to the patient.
- The surface scanning methods needs a suitable surface with enough features. This may pose a problem for localizing the neck and shoulders.
- The electric actuation introduces metal objects which makes it unsuitable for MRI. It also makes imaging by the CT device more difficult due to artifacts (e.g. streaking).
- The cameras used for surface scanning may be obstructed by the gantry during treatment.

D-1-3 Concept 3: IR-Tracking, Electric Actuation

This concept uses IR-tracking to locate the ROIs. The locations of the IR-markers are shown in Fig. D-4. The actuation is done with a Stewart platform driven by electric servos. This concept uses flexible inner padding for the head and neck to establish a good fixation. The working principle is similar to the device by Wiersma et al. [25]. Both use IR-tracking and are electrically actuated. However, this concept has more sets of IR-markers for a better local alignment and uses six degree of freedom (DOF) correction instead of four DOF.

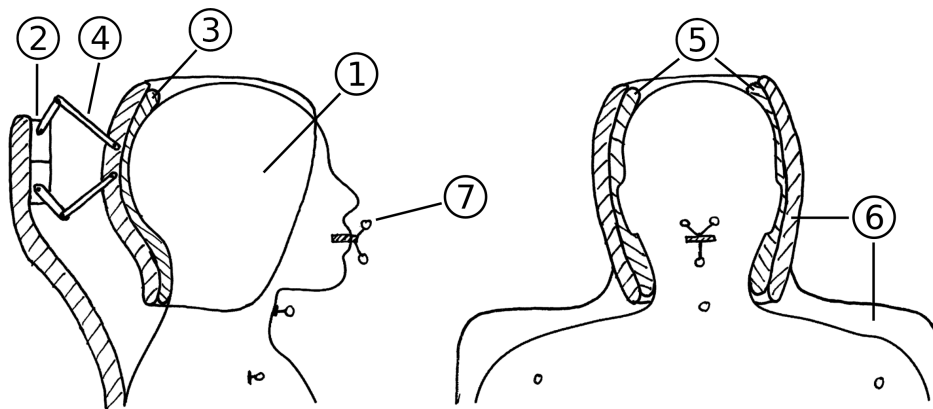


Figure D-4: Concept 3, as denoted by the blue line in Table D-1. Left: lateral view, right: anterior view. Electric servo motors (2). A Stewart platform for six DOF motion (4). The head and neck are enclosed for maximum fixation (1). A cushion provides comfort and a better fixation (3). Elastic foam presses firmly on the sides of the head to keep it in place (5). The immobilization device is not fixed to the treatment couch (6). IR-markers on a bite-block and on the neck and shoulders for the localization of the ROIs (7).

Advantages of this concept:

- IR-markers are easy and reliable to track.
- The error can be corrected continuously, thus intra-fraction drift is eliminated.

Disadvantages of this concept:

- The radiographer must manually place the IR-markers on the neck and shoulders each fraction. An individualized bite-block must be made once for each patient.
- Each fraction the IR-markers must be replaced and re-registered with respect to the CTV. For this at least two X-ray projections are needed. This results in an extra radiation dose given to the patient.
- The electric actuation introduces metal objects which makes it unsuitable for MRI. It also makes imaging by the CT device more difficult due to artifacts (e.g. streaking).
- The IR-tracking cameras may be obstructed by the gantry during treatment.
- The mouth is obstructed by a bite-block. This is slightly uncomfortable for the patient but mostly makes it harder to communicate with the radiographer.

D-2 Concept Selection

The concepts are ranked according to the scores given in Table D-1. The concept with the highest weighted score is concept 1. Concept 3 scored the second highest.

The concept that is selected is therefore concept 1, a pneumatic actuated adaptive immobilization device (Section D-1-1). This concept is:

- **Simple:** it has no moving parts. No lubrication is needed and there is less wear and tear.
- **Rigid:** it is rigidly connected to the treatment couch.
- **Safe:** the inherent compliance makes it safer for the patient.

- **Compatible:** it can be used in proton therapy (PT), CT and MRI environments.

For this concept to work as intended it is assumed that the shoulders are rigid and do not move relative to the treatment couch. It is also assumed that the head will not move in cranial-caudal (CC) direction.

Geometric Membrane Model: Stiffness Mechanisms

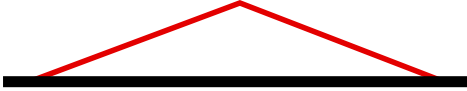
This chapter explores some of the underlying mechanisms for the membrane behavior.

Equation (5-14) shows that the stiffness of the membrane is due to two different mechanisms. They are visualized in Fig. E-1. For $x \ll \delta$ it can be seen that the stiffness is mostly due to the change of contact area since the change of pressure is small. Most notably, $dA/dx|_{x=0} = 2\pi R_0$ is nonzero for a circular membrane. But, due to the reciprocal relation between the volume and pressure from $x > 0.3\delta$ the stiffness due to the change in pressure becomes the dominant effect.

The change of area effect is explored for different geometries in Fig. E-2. In Table E-1 the different cross-sections are compared. The configuration with a single spherical membrane is chosen, because it:

- Is axisymmetric as opposed to the 2×2 grid.
- Uses lower pressures for the same deflection compared to the toroidal and 2×2 grid configurations.
- Is simple to manufacture compared to the cylindrical and conical configurations.
- Is relatively simple to model according to existing literature.

Table E-1: A comparison of the contribution to the change of area effect due to different membrane geometries

| Cross-sectional geometry (axially symmetric, unless otherwise stated) | Contact area $A(x)$ & change of area $\frac{dA}{dx}$ | Description |
|--|--|---|
|  Cylindrical (piston) | $A(x) = \pi R^2,$ $\frac{dA}{dx} = 0.$ | |
|  Conical | $A(x) = \pi \left(\frac{R}{\delta}\right)^2 x^2,$ $\frac{dA}{dx} = 2\pi \left(\frac{R}{\delta}\right)^2 x.$ | $\frac{dA}{dx}$ is smaller than single spherical membrane for: $x < \frac{1}{2}\delta.$ |
|  Spherical | $A(x) = \pi x (2R_0 - x),$ $\frac{dA}{dx} = 2\pi (R_0 - x),$ where $R_0 = \frac{1}{2}R \left(\frac{\delta}{R} + \frac{R}{\delta}\right).$ | |
|  Spherical, 2×2 grid (not axially symmetric) | $A(x) = 4\pi x (2R_0^* - x),$ $\frac{dA}{dx} = 8\pi (R_0^* - x),$ where $R_0^* = \frac{1}{4}R \left(\frac{2\delta}{R} + \frac{R}{2\delta}\right).$ | $\frac{dA}{dx}$ is larger than single spherical membrane for: $x < \frac{1}{2}\delta.$ |
|  Toroidal | $A(x) = 2\pi(R + R_i)\sqrt{x(u-x)},$ $\frac{dA(x)}{dx} = \pi(R + R_i)\frac{u-2x}{\sqrt{x(u-x)}},$ where $u = \delta + \frac{(R_i - R)^2}{4\delta}$ | |

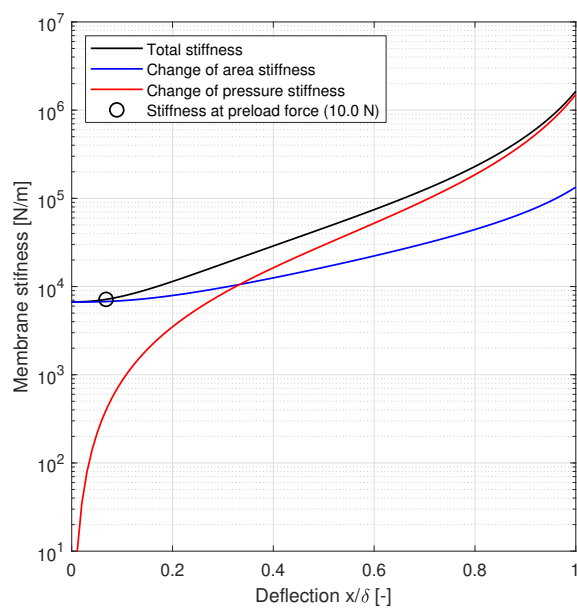


Figure E-1: Stiffness mechanisms. For $x/\delta \ll 1$ the stiffness is primarily due to the change of contact area of the membrane.

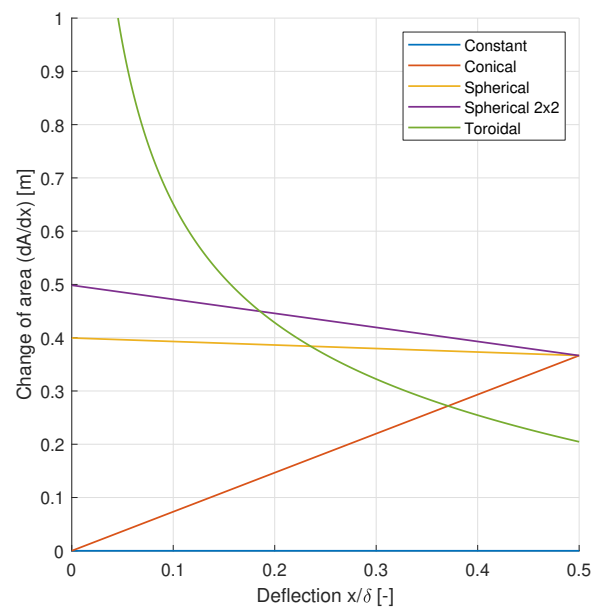


Figure E-2: Change of area for different geometries.

Appendix F

Extended Kalman Filter: Algorithm

The extended Kalman filter is very similar to the normal Kalman filter and works in two stages. There is first the prediction of the new state and then the update of the state based on the measurements. The process is described in more detail by [78]:

- **Predict:**

- Predicted state estimate: $\hat{x}_{k|k-1} = f(\hat{x}_{k|k-1}, u_{k-1})$
- predicted covariance estimate: $P_{k|k-1} = F_k P_{k-1|k-1} F_k^T + Q_k$

- **Update:**

- Innovation or measurement residual: $\tilde{y}_k = z_k - h(\hat{x}_{k|k-1})$
- Innovation (or residual) covariance: $S_k = H_k P_{k|k-1} H_k^T + R_k$
- Kalman gain: $K_k = P_{k|k-1} H_k^T S_k^{-1}$
- Updated state estimate: $\hat{x}_{k|k} = \hat{x}_{k|k-1} + K_k \tilde{y}_k$
- Updated covariance estimate: $P_{k|k} = (I - K_k H_k) P_{k|k-1}$

It uses the following linearization:

$$F_k = \left. \frac{\partial f}{\partial x} \right|_{\hat{x}_{k-1|k-1}, u_k} \quad \text{and} \quad H_k = \left. \frac{\partial h}{\partial x} \right|_{\hat{x}_{k|k-1}, u_k}. \quad (\text{F-1})$$

Bibliography

- [1] IKNL. (2017). Nederlandse kankerregistratie, [Online]. Available: <http://www.cijfersoverkanker.nl> (visited on 10/05/2017).
- [2] J. A. Knottnerus, “De radiotherapie belicht - een vooruitblik tot 2015”, Gezondheidsraad, 2008.
- [3] VARIAN. (2017). ProBeam proton therapy image gallery, [Online]. Available: <http://newsroom.varian.com/ProBeam> (visited on 10/09/2017).
- [4] H. Paganetti, B. S. Athar, M. Moteabbed, J. A. Adams, U. Schneider, and T. I. Yock, “Assessment of radiation-induced second cancer risks in proton therapy and IMRT for organs inside the primary radiation field”, *Physics in Medicine and Biology*, vol. 57, no. 19, pp. 6047–6061, Oct. 7, 2012.
- [5] M. Baumann, M. Krause, J. Overgaard, J. Debus, S. M. Bentzen, J. Daartz, C. Richter, D. Zips, and T. Bortfeld, “Radiation oncology in the era of precision medicine”, *Nature Reviews Cancer*, vol. 16, no. 4, pp. 234–249, Mar. 18, 2016.
- [6] Seattle Cancer Care Alliance. (2017). The advantages of proton therapy over standard x-ray radiation, [Online]. Available: <https://www.sccaprotontherapy.com/cancers-treated/childhood-cancer-treatment> (visited on 12/05/2017).
- [7] A. H. Aitkenhead, D. Bugg, C. G. Rowbottom, E. Smith, and R. I. Mackay, “Modelling the throughput capacity of a single-accelerator multitreatment room proton therapy centre”, *The British Journal of Radiology*, vol. 85, no. 1020, e1263–e1272, Dec. 2012.
- [8] G. Bednarz, M. Machtay, M. Werner-Wasik, B. Downes, J. Bogner, T. Hyslop, J. Galvin, J. Evans, W. Curran, and D. Andrews, “Report on a randomized trial comparing two forms of immobilization of the head for fractionated stereotactic radiotherapy: Randomized trial comparing two head immobilization systems”, *Medical Physics*, vol. 36, no. 1, pp. 12–17, Dec. 4, 2008.
- [9] L. V. Laitinen, B. Liliequist, M. Fagerlund, and A. Eriksson, “An adapter for computed tomography-guided stereotaxis”, *Surgical Neurology*, vol. 23, no. 6, pp. 559–566, Jun. 1985.

- [10] C. B. Saw, R. Yakoob, C. A. Enke, T. P. Lau, and K. M. Ayyangar, “Immobilization devices for intensity-modulated radiation therapy (IMRT)”, *Medical Dosimetry*, vol. 26, no. 1, pp. 71–77, 2001.
- [11] G. C. Bentel, L. B. Marks, G. W. Sherouse, and D. P. Spencer, “A customized head and neck support system”, *International Journal of Radiation Oncology* Biology* Physics*, vol. 32, no. 1, pp. 245–248, 1995.
- [12] D. Schmidhalter, M. K. Fix, M. Wyss, N. Schaer, P. Munro, S. Scheib, P. Kunz, and P. Manser, “Evaluation of a new six degrees of freedom couch for radiation therapy: Evaluation of a new 6dof couch”, *Medical Physics*, vol. 40, no. 11, p. 111710, Oct. 8, 2013.
- [13] T. Gevaert, D. Verellen, B. Engels, T. Depuydt, K. Heuninckx, K. Tournel, M. Duchateau, T. Reynders, and M. De Ridder, “Clinical evaluation of a robotic 6-degree of freedom treatment couch for frameless radiosurgery”, *International Journal of Radiation Oncology* Biology* Physics*, vol. 83, no. 1, pp. 467–474, May 2012.
- [14] Q. Zhang, J. Driewer, S. Wang, S. Li, X. Zhu, D. Zheng, Y. Cao, J. Zhang, A. Jamshidi, and B. W. Cox, “Accuracy evaluation of a six-degree-of-freedom couch using ConeBeam CT and IsoCal phantom with an in-house algorithm”, *Medical Physics*, 2017.
- [15] J. Meyer, J. Wilbert, K. Baier, M. Guckenberger, A. Richter, O. Sauer, and M. Flentje, “Positioning accuracy of cone-beam computed tomography in combination with a HexaPOD robot treatment table”, *International Journal of Radiation Oncology* Biology* Physics*, vol. 67, no. 4, pp. 1220–1228, Mar. 2007.
- [16] M. Guckenberger, J. Meyer, J. Wilbert, K. Baier, O. Sauer, and M. Flentje, “Precision of image-guided radiotherapy (IGRT) in six degrees of freedom and limitations in clinical practice”, *Strahlentherapie und Onkologie*, vol. 183, no. 6, pp. 307–313, Jun. 2007.
- [17] S. D. Sharma, P. Dongre, V. Mhatre, and M. Heigrujam, “Evaluation of automated image registration algorithm for image-guided radiotherapy (IGRT)”, *Australasian Physical & Engineering Sciences in Medicine*, vol. 35, no. 3, pp. 311–319, Sep. 2012.
- [18] S. van Kranen, S. van Beek, A. Mencarelli, C. Rasch, M. van Herk, and J.-J. Sonke, “Correction strategies to manage deformations in head-and-neck radiotherapy”, *Radiotherapy and Oncology*, vol. 94, no. 2, pp. 199–205, Feb. 2010.
- [19] M. Kapanen, M. Laaksomaa, T. Tulijoki, S. Peltola, T. Wigren, S. Hyödynmaa, and P.-L. Kellokumpu-Lehtinen, “Estimation of adequate setup margins and threshold for position errors requiring immediate attention in head and neck cancer radiotherapy based on 2d image guidance”, *Radiation Oncology*, vol. 8, no. 1, p. 212, 2013.
- [20] S. van Kranen, A. Mencarelli, S. van Beek, C. Rasch, M. van Herk, and J.-J. Sonke, “Adaptive radiotherapy with an average anatomy model: Evaluation and quantification of residual deformations in head and neck cancer patients”, *Radiotherapy and Oncology*, vol. 109, no. 3, pp. 463–468, Dec. 2013.

- [21] K. Giske, E. M. Stoiber, M. Schwarz, A. Stoll, M. W. Muentner, C. Timke, F. Roeder, J. Debus, P. E. Huber, C. Thieke, and R. Bendl, “Local setup errors in image-guided radiotherapy for head and neck cancer patients immobilized with a custom-made device”, *International Journal of Radiation Oncology*Biological*Physics*, vol. 80, no. 2, pp. 582–589, Jun. 2011.
- [22] M. Engelsman, S. J. Rosenthal, S. L. Michaud, J. A. Adams, R. J. Schneider, S. G. Bradley, J. B. Flanz, and H. M. Kooy, “Intra- and interfractional patient motion for a variety of immobilization devices: Magnitude of inter- and interfractional patient motion”, *Medical Physics*, vol. 32, no. 11, pp. 3468–3474, Oct. 26, 2005.
- [23] P. Castadot, J. A. Lee, X. Geets, and V. Grégoire, “Adaptive radiotherapy of head and neck cancer”, *Seminars in Radiation Oncology*, vol. 20, no. 2, pp. 84–93, Apr. 2010.
- [24] E. E. Ahunbay, C. Peng, A. Godley, C. Schultz, and X. A. Li, “An on-line replanning method for head and neck adaptive radiotherapy: On-line adaptive radiotherapy”, *Medical Physics*, vol. 36, no. 10, pp. 4776–4790, Sep. 23, 2009.
- [25] R. D. Wiersma, Z. Wen, M. Sadinski, K. Farrey, and K. M. Yenice, “Development of a frameless stereotactic radiosurgery system based on real-time 6d position monitoring and adaptive head motion compensation”, *Physics in Medicine and Biology*, vol. 55, no. 2, pp. 389–401, Jan. 21, 2010.
- [26] X. Liu, A. H. Belcher, Z. Grelewicz, and R. D. Wiersma, “Robotic real-time translational and rotational head motion correction during frameless stereotactic radiosurgery”, *Medical physics*, vol. 42, no. 6, pp. 2757–2763, 2015.
- [27] C. W. Hurkmans, P. Remeijer, J. V. Lebesque, and B. J. Mijnheer, “Set-up verification using portal imaging; review of current clinical practice”, *Radiotherapy and oncology*, vol. 58, no. 2, pp. 105–120, 2001.
- [28] Qfix. (2017). Integrity series qfix, [Online]. Available: <http://www.peo-radiation-technology.com/en/product/integrity-series-qfix/> (visited on 10/13/2017).
- [29] A. C. Houweling, S. van der Meer, E. van der Wal, C. H. Terhaard, and C. P. Raaijmakers, “Improved immobilization using an individual head support in head and neck cancer patients”, *Radiotherapy and Oncology*, vol. 96, no. 1, pp. 100–103, Jul. 2010.
- [30] M. Guckenberger, J. Meyer, D. Vordermark, K. Baier, J. Wilbert, and M. Flentje, “Magnitude and clinical relevance of translational and rotational patient setup errors: A cone-beam CT study”, *International Journal of Radiation Oncology*Biological*Physics*, vol. 65, no. 3, pp. 934–942, Jul. 2006.
- [31] H. Kang, D. M. Lovelock, E. D. Yorke, S. Kriminiski, N. Lee, and H. I. Amols, “Accurate positioning for head and neck cancer patients using 2d and 3d image guidance”, *Journal of applied clinical medical physics*, vol. 12, no. 1, pp. 86–96, 2011.
- [32] O. Gopan and Q. Wu, “Evaluation of the accuracy of a 3d surface imaging system for patient setup in head and neck cancer radiotherapy”, *International Journal of Radiation Oncology*Biological*Physics*, vol. 84, no. 2, pp. 547–552, Oct. 2012.

- [33] B. Polat, J. Wilbert, K. Baier, M. Flentje, and M. Guckenberger, “Nonrigid patient setup errors in the head-and-neck region”, *Strahlentherapie und Onkologie*, vol. 183, no. 9, pp. 506–511, Sep. 2007.
- [34] M. Djordjevic, E. Sjöholm, O. Tullgren, and B. Sorcini, “Assessment of residual setup errors for anatomical sub-structures in image-guided head-and-neck cancer radiotherapy”, *Acta Oncologica*, vol. 53, no. 5, pp. 646–653, May 2014.
- [35] X. Chen, M. R. Varley, L.-K. Shark, G. S. Shentall, and M. C. Kirby, “A computationally efficient method for automatic registration of orthogonal x-ray images with volumetric CT data”, *Physics in Medicine and Biology*, vol. 53, no. 4, pp. 967–983, Feb. 21, 2008.
- [36] A. D. Jensen, M. Winter, S. P. Kuhn, J. Debus, O. Nairz, and M. W. Münter, “Robotic-based carbon ion therapy and patient positioning in 6 degrees of freedom: Setup accuracy of two standard immobilization devices used in carbon ion therapy and IMRT”, *Radiation Oncology*, vol. 7, no. 1, p. 51, 2012.
- [37] J. Boda-Heggemann, C. Walter, A. Rahn, H. Wertz, I. Loeb, F. Lohr, and F. Wenz, “Repositioning accuracy of two different mask systems3d revisited: Comparison using true 3d/3d matching with cone-beam CT”, *International Journal of Radiation Oncology*Biology*Physics*, vol. 66, no. 5, pp. 1568–1575, Dec. 2006.
- [38] M. van Herk, “Errors and margins in radiotherapy”, *Seminars in Radiation Oncology*, vol. 14, no. 1, pp. 52–64, Jan. 2004.
- [39] J. Yang, A. S. Garden, Y. Zhang, L. Zhang, and L. Dong, “Variable planning margin approach to account for locoregional variations in setup uncertainties”, *Medical physics*, vol. 39, no. 8, pp. 5136–5144, 2012.
- [40] S. van Kranen, S. van Beek, C. Rasch, M. van Herk, and J.-J. Sonke, “Setup uncertainties of anatomical sub-regions in head-and-neck cancer patients after offline CBCT guidance”, *International Journal of Radiation Oncology*Biology*Physics*, vol. 73, no. 5, pp. 1566–1573, Apr. 2009.
- [41] L. Zhang, A. S. Garden, J. Lo, K. K. Ang, A. Ahamad, W. H. Morrison, D. I. Rosenthal, M. S. Chambers, X. R. Zhu, R. Mohan, and L. Dong, “Multiple regions-of-interest analysis of setup uncertainties for head-and-neck cancer radiotherapy”, *International Journal of Radiation Oncology*Biology*Physics*, vol. 64, no. 5, pp. 1559–1569, Apr. 2006.
- [42] J. L. Barker, A. S. Garden, K. Ang, J. C. O’Daniel, H. Wang, L. E. Court, W. H. Morrison, D. I. Rosenthal, K. Chao, S. L. Tucker, R. Mohan, and L. Dong, “Quantification of volumetric and geometric changes occurring during fractionated radiotherapy for head-and-neck cancer using an integrated CT/linear accelerator system”, *International Journal of Radiation Oncology*Biology*Physics*, vol. 59, no. 4, pp. 960–970, Jul. 2004.
- [43] B. Zhao, G. Maquilan, S. Jiang, and D. L. Schwartz, “Minimal mask immobilization with optical surface guidance for head and neck radiotherapy”, *Journal of Applied Clinical Medical Physics*, vol. 19, no. 1, pp. 17–24, Jan. 2018.

- [44] G. Li, D. M. Lovelock, J. Mechalakos, S. Rao, C. Della-Biancia, H. Amols, and N. Lee, “Migration from full-head mask to open-face mask for immobilization of patients with head and neck cancer”, *Journal of Applied Clinical Medical Physics*, vol. 14, no. 5, pp. 243–254, Sep. 2013.
- [45] A. J. Olch, L. Gerig, H. Li, I. Mihaylov, and A. Morgan, “Dosimetric effects caused by couch tops and immobilization devices: Report of AAPM task group 176”, *Medical physics*, vol. 41, no. 6, 2014.
- [46] S. Hamlet, G. Ezzell, and A. Aref, “Larynx motion associated with swallowing during radiation therapy”, *International Journal of Radiation Oncology*Biophysics*Physics*, vol. 28, no. 2, pp. 467–470, Jan. 1994.
- [47] L. Gilbeau, M. Octave-Prignot, T. Loncol, L. Renard, P. Scalliet, and V. Grégoire, “Comparison of setup accuracy of three different thermoplastic masks for the treatment of brain and head and neck tumors”, *Radiotherapy and Oncology*, vol. 58, no. 2, pp. 155–162, 2001.
- [48] A. Poston, “Human engineering design data digest: Human factors standardization systems”, *Human Factors Standardization SubTAG*, 2000.
- [49] A. N. Vasavada, S. Li, and S. L. Delp, “Influence of muscle morphometry and moment arms on the moment-generating capacity of human neck muscles”, *Spine*, vol. 23, no. 4, pp. 412–422, 1998.
- [50] H.-J. Su, D. V. Dorozhkin, and J. M. Vance, “A screw theory approach for the conceptual design of flexible joints for compliant mechanisms”, *Journal of Mechanisms and Robotics*, vol. 1, no. 4, p. 041 009, 2009.
- [51] N. Yoganandan, F. A. Pintar, J. Zhang, and J. L. Baisden, “Physical properties of the human head: Mass, center of gravity and moment of inertia”, *Journal of Biomechanics*, vol. 42, no. 9, pp. 1177–1192, Jun. 2009.
- [52] P. M. Hopkins, “Skeletal muscle physiology”, *Continuing Education in Anaesthesia Critical Care & Pain*, vol. 6, no. 1, pp. 1–6, Feb. 2006.
- [53] S. P. Moroney, A. B. Schultz, and J. A. Miller, “Analysis and measurement of neck loads”, *Journal of Orthopaedic Research*, vol. 6, no. 5, pp. 713–720, 1988.
- [54] A. A. Vasserman, Y. Z. Kazavchinskii, and V. A. Rabinovich, “Thermophysical properties of air and air components (teplofizicheskie svoistva vozdukha i ego komponentov)”, NATIONAL STANDARD REFERENCE DATA SYSTEM, 1971.
- [55] R. Long, K. R. Shull, and C.-Y. Hui, “Large deformation adhesive contact mechanics of circular membranes with a flat rigid substrate”, *Journal of the Mechanics and Physics of Solids*, vol. 58, no. 9, pp. 1225–1242, Sep. 2010.
- [56] A. Libai and J. G. Simmonds, *The Nonlinear Theory of Elastic Shells*, 2nd ed. Cambridge University Press, 1998.
- [57] L. R. G. Treloar, *The physics of rubber elasticity*. Oxford University Press, USA, 1975.
- [58] A. Srivastava and C.-Y. Hui, “Large deformation contact mechanics of long rectangular membranes. i. adhesionless contact”, *Proceedings of the Royal Society A: Mathematical, Physical and Engineering Sciences*, vol. 469, no. 2160, pp. 20 130 424–20 130 424, Sep. 25, 2013.

- [59] O. Hassager, S. B. Kristensen, J. R. Larsen, and J. Neergaard, "Inflation and instability of a polymeric membrane", *Journal of Non-Newtonian Fluid Mechanics*, vol. 88, no. 1, pp. 185–204, Dec. 1999.
- [60] L. Kari, "The non-linear temperature dependent stiffness of precompressed rubber cylinders", *KGK Kautschuk Gummi Kunststoffe*, p. 6, 2002.
- [61] MATLAB. (2018). Find minimum of constrained nonlinear multivariable function - MATLAB fmincon, [Online]. Available: <https://www.mathworks.com/help/optim/ug/fmincon.html> (visited on 09/19/2018).
- [62] Cambridge University Engineering Department, *Materials Data Book*. 2003.
- [63] S. M. McGill, K. Jones, G. Bennett, and P. J. Bishop, "Passive stiffness of the human neck in flexion, extension, and lateral bending", *Clinical Biomechanics*, vol. 9, no. 3, pp. 193–198, 1994.
- [64] F. Vuvor and O. Harrison, "A study of the diurnal height changes among sample of adults aged 30 years and above in ghana", *Biomedical and Biotechnology Research Journal (BBRJ)*, vol. 1, no. 2, p. 113, 2017.
- [65] D. J. Magee, *Orthopedic physical assessment*, 6th edition. St. Louis, Missouri: Elsevier, 2014, 1173 pp.
- [66] S. P. Moroney, A. B. Schultz, J. A. Miller, and G. B. Andersson, "Load-displacement properties of lower cervical spine motion segments", *Journal of Biomechanics*, vol. 21, no. 9, pp. 769–779, Jan. 1988.
- [67] S. Stramigioli and H. Bruyninckx, "Geometry and screw theory for robotics", p. 75, May 15, 2001.
- [68] A. Hourtash, "The kinematic hessian and higher derivatives", IEEE, 2005, pp. 169–174.
- [69] J. Reddy, *Theory and Analysis of Elastic Plates and Shells, Second Edition*. CRC Press, Nov. 20, 2006.
- [70] R. Hibbeler, *Engineering Mechanics: Dynamics*. Pearson education, 2012.
- [71] M. Verhaegen and V. Verdult, *Filtering and system identification: a least squares approach*. Cambridge university press, 2007.
- [72] B. Friedland, *Control system design: an introduction to state-space methods*. Courier Corporation, 2012.
- [73] S. P. Boyd and L. Vandenberghe, *Convex optimization*. Cambridge, UK ; New York: Cambridge University Press, 2004, 716 pp.
- [74] Leppee. (Feb. 2, 2013). Head low poly base, [Online]. Available: <https://www.turbosquid.com/3d-models/free-base-heads-3d-model/721696> (visited on 09/13/2018).
- [75] R. Muller-Cajar and R. Mukundan, "Triangulation-a new algorithm for inverse kinematics", 2007.
- [76] Blausen.com staff, "Medical gallery of blausen medical 2014", *WikiJournal of Medicine*, vol. 1, no. 2, p. 10, 2014.

- [77] (Jan. 13, 2018). Bone structures head and neck bones, Anatomy Sciences, [Online]. Available: <http://anatomysciences.com/bone-structures-head-and-neck-bones/> (visited on 09/26/2018).
- [78] Wikipedia. (2018). Extended kalman filter. Page Version ID: 857194375, [Online]. Available: https://en.wikipedia.org/w/index.php?title=Extended_Kalman_filter&oldid=857194375 (visited on 09/20/2018).

List of Acronyms

| | |
|------------|---|
| AP | Anterior-posterior |
| CC | Cranial-caudal |
| CT | Computed tomography |
| CTV | Clinical target volume |
| DOF | Degree of freedom |
| ENT | Ear, nose and throat |
| GTV | Gross tumor volume |
| IID | Independent and identically distributed |
| IR | Infrared |
| LR | Left-right |
| LTI | Linear time-invariant |
| MRI | Magnetic resonance imaging |
| pCT | Planning-CT |
| PT | Proton therapy |
| PTV | Planning target volume |
| QA | Quality assurance |
| RMS | Root mean square |
| ROI | Region-of-interest |

| | |
|-------------|----------------------------------|
| RT | Radiotherapy |
| SD | Standard deviation |
| SMA | Shape-memory alloy |
| SMP | Shape-memory polymer |
| SOBP | Spread-out Bragg peak |
| SQP | Sequential quadratic programming |
| SRS | Stereotactic radiosurgery |